MID-AMERICA TRANSPORTATION CENTER

Report # MATC-KU: 151-4

Final Report

WBS: 25-1121-0005-151-4

Automated Bridge Inspection using Digital Image Correlation and Other Vision-based Methods - Phase IV

William Collins, PhD, PE
Assistant Professor
Department of Civil, Environmental & Architectural Engineering
The University of Kansas

Caroline Bennett, PhD, PE
Professor

Rushil Mojidra
Research Assistant

Jian Li, PhD, PE
Associate Professor

Jaswant Cobos
Research Assistant

Afeez Badmus
Research Assistant

2023

A Cooperative Research Project sponsored by U.S. Department of Transportation- Office of the Assistant Secretary for Research and Technology

The contents of this report reflect the views of the authors, who are responsible for the facts and the accuracy of the information presented herein. This document is disseminated in the interest of information exchange. The report is funded, partially or entirely, by a grant from the U.S. Department of Transportation's University Transportation Centers Program. However, the U.S. Government assumes no liability for the contents or use thereof.

Automated Bridge Inspection using Digital Image Correlation and other Vision-based Methods

William Collins, Ph.D., P.E.
Associate Professor
CEAE Department
University of Kansas

Caroline Bennett, Ph.D., P.E.
Professor, Chair
CEAE Department
University of Kansas

Jian Li, Ph.D., P.E.
Professor
CEAE Department
University of Kansas

Afeez Badmus
Research Assistant
CEAE Department
University of Kansas

Rushil Mojidra
Research Assistant
CEAE Department
University of Kansas

Jaswant Cobos
Research Assistant
CEAE Department
University of Kansas

A Report on Research Sponsored by

Mid-America Transportation Center

University of Nebraska–Lincoln

September 2024

TECHNICAL REPORT DOCUMENTATION PAGE

1. Report No. 25-1121-0005-151-4	2. Government Accession No.	3. Recipient's Catalog No.
4. Title and Subtitle Automated Bridge Inspection using Digital Image Correlation and other Vision-based Methods – Phase IV		5. Report Date September 2023 6. Performing Organization Code
7. Author(s) William Collins, Ph.D., Caroline Bennett, Ph.D., Jian Li, Ph.D., Mary Juno, and Hayder Al-Salih		8. Performing Organization Report No. 25-1121-0005-151-4
9. Performing Organization Name and Address University of Kansas 2150 Learned Hall, 1530 W. 15th St. Lawrence, KS 66049		10. Work Unit No. 11. Contract or Grant No. 69A3551747107
12. Sponsoring Agency Name and Address Mid-America Transportation Center		13. Type of Report and Period Covered Final Report June 2020 – June 2023 14. Sponsoring Agency Code MATC TRB RiP No. 91994-114
15. Supplementary Notes Conducted in cooperation with the U.S. Department of Transportation, Federal Highway Administration.		

16. Abstract

One of the main concerns for aging steel bridges in the United States is the initiation and propagation of distortion-induced fatigue cracks. Distortion-induced fatigue cracks account for most of the fatigue cracks in bridges. Despite recent studies proving that visual inspections consistently fail to identify realistically sized fatigue cracks, Departments of Transportation are forced to rely primarily on the use of visual inspections to locate and characterize fatigue cracking. Many detection methodologies have been examined for fatigue crack detection, but the methods are dependent on detection equipment that is physically attached to the bridge, such as sensor networks, which limits the flexibility of the methods for analyzing the multiple fatigue susceptible regions present on highway bridges. The development of an inspection technique that is not dependent on human visual inspection or physical attachments would have the potential to decrease the time and cost of performing inspections, as well as decrease the risk of injury to inspectors and increase reliability.

The ability of vision-based technologies to serve as an alternative to manual inspections of highway bridges is an area of active research. While many vision-based technologies have been proven to detect macro-indicators of damage, digital image correlation (DIC) has shown potential for detecting and characterizing fatigue cracks. Since DIC measurements have the ability to capture full-field displacements and surface strains, it is proven that developed DIC methodologies have the ability to identify and characterize both in-plane and out-of-plane fatigue cracks, allowing application to steel bridges exposed to differential girder displacement. This report summarizes the development of a crack-detection methodology using DIC and focuses on the impact of crack complexity on the developed methodology. Research indicates that DIC is successful at detecting complex branched distortion-induced fatigue cracks, but automation presents challenges.

17. Key Words Fatigue, cracking, bridge, steel, inspection, digital image correlation		18. Distribution Statement No restrictions. This document is available through the National Technical Information Service, Springfield, VA 22161.	
19. Security Classif. (of this report)	20. Security Classif. (of this page)	21. No. of Pages 105	22. Price

Form DOT F 1700.7 (8-72) Reproduction of completed page authorized

Table of Contents

Disclaimer viii
Abstract ix
Chapter 1 Digital Image Correlation Background 1
1.1 Introduction 1
1.2 Digital Image Correlation Methodology 3
1.2.1 Computer Vision 3
1.2.2 Digital Image Correlation Background 4
1.2.3 Digital Image Correlation Setup 6
Chapter 2 Previous Work Overview 7
2.1 Initial In-Plane Testing 7
2.1.1 Initial Testing and Methodology Development 7
2.1.2 Crack Characterization Methodology 7
2.2 Distortion-Induced Fatigue Testing 8
2.2.1 Initial Distortion-Induced Fatigue Testing 9
2.2.1.1 Initial Distortion-Induced Fatigue Test Setup and Loading 9
2.2.1.2 Initial Distortion-Induced Fatigue DIC Configuration 10
2.2.1.3 Initial Distortion-Induced Fatigue Crack Characterization Methodology 11
2.2.2 Complex Branched Distortion-Induced Fatigue Crack Methodology 12
2.2.2.1 Complex Branched Crack Pattern 12
2.2.2.2 Complex Branched Crack Data Collection Loading 13
2.2.2.3 Crack Characterization Methodology 14
2.2.3 Complex Branched Distortion-Induced Fatigue Crack Results 15
2.2.3.1 Vertical Crack Characterization Results 18
2.2.3.2 Branched Crack I Characterization Results 20
2.2.3.3 Branched Crack II Characterization Results 21
2.2.3.4 Horizontal Web-to-Flange Crack Characterization Results 23
2.2.3.5 Complex Branched Distortion-Induced Fatigue Crack Summary 24
2.3 Advancements Towards Automation 26
2.3.1 Lighting and Focus Testing 26
2.3.1.1 Lighting and Focus Test Setup, Loading, and Conditions 27
2.3.1.2 Lighting and Focus Testing Results 28
2.3.2 Study on the Impact of Aperture 33
2.3.2.1 Aperture Test Setup and Loading 34
2.3.2.2 Aperture Study Results 34
2.3.3 Investigation into Open-Source DIC Alternatives 36
2.3.3.1 Open-Source Software Alternatives 36
2.3.4 Distortion-Induced Fatigue Crack Single Camera Testing 37
2.3.4.1 Single Camera Test Setup and Loading 38
2.3.4.2 Single Camera Results 40
Chapter 3 Cantilever Overhead Sign Structure Fatigue Crack Testing 43
3.1 Cantilever Overhead Sign Structure Fatigue Crack Test Setup and Loading 43
3.1.1 Cantilever Overhead Sign Structure Background 43
3.1.2 Cantilever Overhead Sign Structure Fatigue Crack Test Setup 44
3.1.3 Cantilever Overhead Sign Structure Fatigue Crack Loading 46

3.2 Cantilever Overhead Sign Structure Fatigue Crack Detection 48
3.2.1 DIC System Configuration and Specifications 48
3.2.2 DIC Post-Processing 51
3.3 Cantilever Overhead Sign Structure Fatigue Crack Results 51
3.3.1 Crack Detection Results 51
Chapter 4 Application of DIC to Fracture-prone Component Evaluation 55
4.1 Recognition of Potential for Application to Fracture-prone Component Evaluation . 55
4.1.1 Potential Applications 55
4.1.2 Brief Background on Constraint-induced Fracture 55
4.2 Constraint-induced Fracture Testing and Results 56
4.2.1 Constraint-induced Fracture Specimen Design 56
4.2.2 Results of DIC during Constraint-induced Fracture Testing 58
Chapter 5 Continued Advancements Towards Automation 64
5.1 Digital Image Correlation Using Deep Learning Algorithms 64
5.1.1 Deep Learning Background 64
5.1.2 Synthetic Data Generation Method 67
5.1.3 Deep Learning DIC Architecture 69
5.1.4 Deep Learning DIC Training and Results 70
Chapter 6 Conclusions and Future Work 74
6.1 Conclusions 74
6.2 Future Work 75
References 77
Appendix A ..... Previous Work 83

List of Figures

Figure 2.1 (a) Hardware locations for out-of-plane testing, (b) hardware orientation as seen from above, and (c) fatigue susceptible region with speckle pattern applied 10
Figure 2.2 (a) Fatigue cracks in web-gap region and (b) schematic of crack path with orthogonal data extraction lines 13
Figure 2.3 Representative DIC results for (a) U-displacement along the *x*-axis, (b) V-displacement along the *y*-axis, and (c) W-displacement along the *z*-axis 15
Figure 2.4 Typical visualized DIC strains: (a) strain in *x*-axis; (b) strain in *y*-axis; (c) strain in *xy*-plane; (d) max principal strain; (e) min principal strain; (f) von Mises strain 16
Figure 2.5 Vertical Crack: (a) relative W-displacement; (b) convergence of relative W-displacement; (c) relative V-displacement; (d) convergence of relative V-displacement 19
Figure 2.6 Branched Crack I: (a) relative W-displacement; (b) convergence of relative W-displacement; (c) relative V-displacement; (d) convergence of relative V-displacement 20
Figure 2.7 Branched Crack II: (a) relative W-displacement; (b) convergence of relative W-displacement; (c) relative V-displacement; (d) convergence of relative V-displacement 22
Figure 2.8 Horizontal web-to-flange crack: (a) relative V-displacement; (b) convergence of relative V-displacement 23
Figure 2.9 (a) Absolute average percent error between predicted and actual crack lengths for 95% and 98% convergence for relative V- and W-displacement; (b) predicted crack lengths based on 95% and 98% convergence for relative V- and W-displacement 25
Figure 2.10 DIC results for a 25.4 mm (1.0 in.) crack with 648 mm (25.5 in.) camera distance under LC5 and Condition 1 in terms of (a) displacement and (b) strain 29
Figure 2.11 DIC results for a 25.4 mm (1.0 in.) crack with 648 mm (25.5 in.) camera distance under LC5 and Condition 1 in terms of (a) displacement and (b) strain 29
Figure 2.12 Relative displacement of a 25.4 mm (1.0 in.) crack under LC5 30
Figure 2.13 Convergence of relative displacement of a 25.4 mm (1.0 in.) crack under LC5 31
Figure 2.14 Average convergence at crack tip for each load case and condition for a crack of 25.4 mm (1.0 in.) with a camera to specimen spacing of 648 mm (25.5 in.) 32
Figure 2.15 C(T) specimen photographed with apertures of (a) f/2.8; (b) f/4; and (c) f/11 33
Figure 2.16 Convergence of relative displacement of a 50.8 mm (2.0 in.) crack with a camera distance of 203 mm (8.0 in.) and an aperture of f/1.4 under LC5 35
Figure 2.17 Crack location and geometry 38
Figure 2.18 Cracked web gap region as seen from (a) camera 1 and (b) camera 2 39
Figure 2.19 Convergence of relative displacement of a 44.5 mm (1.75 in.) complex crack under LC7 40
Figure 3.1 Schematic of a COSS box connection 43
Figure 3.2 Schematic of the COSS test setup 45
Figure 3.3 COSS test specimen 46
Figure 3.4 3D DIC setup for the (a) box connection, (b) mast-arm, and (c) baseplate 49
Figure 3.5 Strain fields before and after fatigue crack initiation 53
Figure 4.1. Schematic representation of discontinuous transverse stiffener CIF specimen 57
Figure 4.2 CIF specimen in place with partial self-reacting load frame 57
Figure 4.3 Stiffener details 58
Figure 4.4 High-contrast pattern on CIF specimen prior to testing 59
Figure 4.5 DIC cameras and lighting suspended above the CIF specimen 60

Figure 4.6 DIC calibration image of CIFC cameras and lighting suspended above the CIF specimen 61
Figure 4.7 DIC principal strain fields at a) 657 kN (148 kips), b) 897 kN (202 kips), and c) 1926 kN (433 kips) of tensile force 63
Figure 5.1 Artificial neural network structure 65
Figure 5.2 Uncracked dataset generation 68
Figure 5.3 Unet architecture 70
Figure 5.4 Training loss for the proposed model 71
Figure 5.5 Two sample predictions from the test dataset 73
Figure 6.1 Overall methodology of experimental validation 75
Figure 6.2 Laboratory images of speckle pattern patches from C(T) specimen 76
Figure A.1 DIC results for a 25.4 mm (1.0 in.) crack with 648 mm (25.5 in.) camera distance under LC5 and Condition 1 in terms of (a) displacement and (b) strain 84
Figure A.2 DIC results for a 25.4 mm (1.0 in.) crack with 648 mm (25.5 in.) camera distance under LC5 and Condition 5 in terms of (a) displacement and (b) strain 84
Figure A.3 DIC results for a 25.4 mm (1.0 in.) crack with 432 mm (17.0 in.) camera distance under LC5 and Condition 1 in terms of (a) displacement and (b) strain 85
Figure A.4 DIC results for a 25.4 mm (1.0 in.) crack with 432 mm (17.0 in.) camera distance under LC5 and Condition 5 in terms of (a) displacement and (b) strain 85
Figure A.5 DIC results for a 25.4 mm (1.0 in.) crack with 216 mm (8.5 in.) camera distance under LC5 and Condition 1 in terms of (a) displacement and (b) strain 86
Figure A.6 DIC results for a 25.4 mm (1.0 in.) crack with 216 mm (8.5 in.) camera distance under LC5 and Condition 5 in terms of (a) displacement and (b) strain 86
Figure A.7 Relative displacement of a 25.4 mm (1.0 in.) crack with a camera distance of 648 mm (25.5 in.) under LC5 87
Figure A.8 Convergence of relative displacement of a 25.4 mm (1.0 in.) crack with a camera distance of 648 mm (25.5 in.) under LC5 88
Figure A.9 Relative displacement of a 25.4 mm (1.0 in.) crack with a camera distance of 432 mm (17.0 in.) under LC5 88
Figure A.10 Convergence of relative displacement of a 25.4 mm (1.0 in.) crack with a camera distance of 432 mm (17.0 in.) under LC5 89
Figure A.11 Relative displacement of a 25.4 mm (1.0 in.) crack with a camera distance of 216 mm (8.5 in.) under LC5 89
Figure A.12 Convergence of relative displacement of a 25.4 mm (1.0 in.) crack with a camera distance of 216 mm (8.5 in.) under LC5 90
Figure A.13 Average convergence at crack tip for each load case and condition for a 25.4 mm (1.0 in.) crack with a camera distance of 648 mm (25.5 in.) 91
Figure A.14 Average convergence at crack tip for each load case and condition for a 25.4 mm (1.0 in.) crack with a camera distance of 432 mm (17.0 in.) 92
Figure A.15 Average convergence at crack tip for each load case and condition for a 25.4 mm (1.0 in.) crack with a camera distance of 216 mm (8.5 in.) 93
Figure A.16 Convergence of relative displacement of a 50.8 mm (2.0 in.) crack with a camera distance of 203.2 mm (8.0 in.) and an aperture of f/1.4 under LC5 94
Figure A.17 Convergence of relative displacement of a 50.8 mm (2.0 in.) crack with a camera distance of 203.2 mm (8.0 in.) and an aperture of f/2.8 under LC5 95

Figure A.18 Convergence of relative displacement of a 50.8 mm (2.0 in.) crack with a camera distance of 304.8 mm (12.0 in.) and an aperture of f/1.4 under LC5 95
Figure A.19 Convergence of relative displacement of a 50.8 mm (2.0 in.) crack with a camera distance of 304.8 mm (12.0 in.) and an aperture of f/2.8 under LC5 96
Figure A.20 Convergence of relative displacement of a 50.8 mm (2.0 in.) crack with a camera distance of 457.2 mm (18.0 in.) and an aperture of f/1.4 under LC5 96
Figure A.21 Convergence of relative displacement of a 50.8 mm (2.0 in.) crack with a camera distance of 457.2 mm (18.0 in.) and an aperture of f/2.8 under LC5 97
Figure A.22 Convergence of relative displacement of a 50.8 mm (2.0 in.) crack with a camera distance of 609.6 mm (24.0 in.) and an aperture of f/1.4 under LC5 97
Figure A.23 Convergence of relative displacement of a 50.8 mm (2.0 in.) crack with a camera distance of 609.6 mm (24.0 in.) and an aperture of f/2.8 under LC5 98
Figure A.24 *Ncorr* in-plane crack displacement gradient 99
Figure A.25 *Ncorr* out-of-plane crack displacement gradient 99
Figure A.26 *ALDIC* in-plane crack displacement gradient 100
Figure A.27 *ALDIC* out-of-plane crack displacement gradient 100
Figure A.28 DICe in-plane crack displacement gradient 101
Figure A.29 *DICe* out-of-plane crack displacement gradient 101
Figure A.30 Convergence of relative displacement of a 44.5 mm (1.75 in.) complex crack under LC1 102
Figure A.31 Convergence of relative displacement of a 44.5 mm (1.75 in.) complex crack under LC2 103
Figure A.32 Convergence of relative displacement of a 44.5 mm (1.75 in.) complex crack under LC3 103
Figure A.33 Convergence of relative displacement of a 44.5 mm (1.75 in.) complex crack under LC4 104
Figure A.34 Convergence of relative displacement of a 44.5 mm (1.75 in.) complex crack under LC5 104
Figure A.35 Convergence of relative displacement of a 44.5 mm (1.75 in.) complex crack under LC6 105
Figure A.36 Convergence of relative displacement of a 44.5 mm (1.75 in.) complex crack under LC7 105

List of Tables

Table 2.1 Crack designations and lengths 13
Table 2.2 Out-of-plane load cases 14
Table 2.3 Average convergence at 25.4 mm (1.0 in.) crack tip for 648 mm (25.5 in.) camera distance 32
Table 2.4 Convergence of 50.8 mm (2.0 in.) crack under varying camera distances and aperture conditions 35
Table 2.5 Single camera out-of-plane loading cases 39
Table 2.6 Convergence at 44.5 mm (1.75 in.) crack tip from U-displacement 41
Table 3.1 COSS dimensions 44
Table 3.2 COSS load and box connection stress ranges 48
Table 5.1 Minimum and maximum values of different deformation elements 68
Table 5.2 Model Performance Metrics 72
Table A.1 Light and focus conditions for 648 mm (25.5 in.) distance 83
Table A.2 Light and focus conditions for 432 mm (17.0 in.) distance 83
Table A.3 Light and focus conditions for 216 mm (8.5 in.) distance 83
Table A.4 Average convergence at 25.4 mm (1.0 in.) crack tip for 648 mm (25.5 in.) camera distance 91
Table A.5 Average convergence at 25.4 mm (1.0 in.) crack tip for 432 mm (17.0 in.) camera distance 92
Table A.6 Average convergence at 25.4 mm (1.0 in.) crack tip for 216 mm (8.5 in.) camera distance 93

Disclaimer

The contents of this report reflect the views of the authors, who are responsible for the facts and the accuracy of the information presented herein. This document is disseminated in the interest of information exchange. The report is funded, partially or entirely, by a grant from the U.S. Department of Transportation's University Transportation Centers Program. However, the U.S. Government assumes no liability for the contents or use thereof.

Abstract

One of the main concerns for aging steel bridges in the United States is the initiation and propagation of distortion-induced fatigue cracks. Distortion-induced fatigue cracks account for most of the fatigue cracks in bridges. Despite recent studies proving that visual inspections consistently fail to identify realistically sized fatigue cracks, Departments of Transportation are forced to rely primarily on the use of visual inspections to locate and characterize fatigue cracking. Many detection methodologies have been examined for fatigue crack detection, but the methods are dependent on detection equipment that is physically attached to the bridge, such as sensor networks, which limits the flexibility of the methods for analyzing the multiple fatigue susceptible regions present on highway bridges. The development of an inspection technique that is not dependent on human visual inspection or physical attachments would have the potential to decrease the time and cost of performing inspections, as well as decrease the risk of injury to inspectors and increase reliability.

The ability of vision-based technologies to serve as an alternative to manual inspections of highway bridges is an area of active research. While many vision-based technologies have been proven to detect macro-indicators of damage, digital image correlation (DIC) has shown potential for detecting and characterizing fatigue cracks. Since DIC measurements have the ability to capture full-field displacements and surface strains, it is proven that developed DIC methodologies have the ability to identify and characterize both in-plane and out-of-plane fatigue cracks, allowing application to steel bridges exposed to differential girder displacement. This report summarizes the development of a methodology for crack detection using DIC and focuses on the impact of crack complexity on the developed methodology. Research indicates that DIC is successful at detecting complex branched distortion-induced fatigue cracks, but automation presents challenges.

Chapter 1 Digital Image Correlation Background

1.1 Introduction

Bridges are vital to the movement of goods and people across the country but are prone to damage and deterioration from repetitive loads over their long service life. In their most recent Infrastructure Report Card, the American Society of Civil Engineers gave bridges in the United States a grade of C and found that over 7.5 percent of bridges are considered structurally deficient (ASCE 2021). Identifying and repairing potential issues is vital to properly maintaining bridges and ensuring that they remain in-service for at least the entirety of their intended service life.

One of the major issues impacting older steel bridges is the initiation and propagation of fatigue cracks (Fisher 1984), specifically distortion-induced fatigue cracks, which accounts for almost 90% of fatigue cracks in aging steel bridges in the United States (Connor and Fisher 2006). Steel bridges built prior to the 1980s in the United States were regularly designed without a connection between the flanges and connection plate, which can increase the rate of initiation for distortion-induced fatigue cracks (Zhao and Roddis 2004). When a bridge with this detail experiences traffic loads, the girders are subjected to differential deflection between them. The differential deflection can allow the cross-frame to push or pull on the girder web which causes out-of-plane stresses to be applied to the weak web gap region, resulting in distortion-induced fatigue cracks.

To minimize the potential impact of distortion-induced fatigue cracking, bridges are required to be repaired or retrofitted based on the findings of regular inspections. Bridge inspections are typically performed on a 24-month cycle (FHWA 2004), and the most common method for fatigue crack detection is through visual inspection. Fatigue cracks are caused by cyclic traffic loads, and they are initially very small and challenging to detect through visual inspection.

When cracks go undetected, however, they have the potential to propagate to a critical size, which could compromise a bridge's structural integrity. Although bridge inspections are necessary to ensure the safety of bridge infrastructure, visual inspections have significant monetary and time costs, as well as presenting safety risks to both inspectors and the travelling public. Additionally, the identification of realistic fatigue cracks has been proven to be extremely difficult and inconsistent (Campbell et al. 2020; Whitehead 2015; Zhao and Haldar 1996).

Technologies to detect and monitor cracking has been evaluated by researchers interested in structural health monitoring (SHM) and non-destructive testing (NDT). While sensing technologies have been used successfully to detect and monitor both in- and out-of-plane cracks, many of these approaches require the use of sensors or other components that physically attach to a particular location on a bridge, preventing these methodologies from effectively monitoring the various regions of fatigue susceptibility on steel bridges. The development of a computer vision-based detection methodology that would operate without dependence on a physical attachment would allow large sections of steel bridges to be surveyed safely and efficiently.

Some research has been performed on vision-based crack detection methodologies, but the majority of testing conducted was under highly idealized conditions that only evaluated in-plane fatigue loading or non-metallic materials (Vanlanduit et al. 2009; Rupil et al. 2011; Nowell et al. 2010). Very few research programs have evaluated vision-based crack detection methods on out-of-plane fatigue loading or with the complex geometries commonly found on steel highway bridges. A vision-based crack detection methodology that utilizes digital image correlation (DIC) is being evaluated for performance on both ideal and non-ideal in-plane lab setups and out-of-plane test setups with complex geometry and distortion-induced fatigue cracking.

1.2 Digital Image Correlation Methodology

1.2.1 Computer Vision

Computer vision refers to the branch of technology that utilizes computer algorithms and optics to collect information from pictures and videos. Researchers in engineering and material sciences have evaluated computer vision for different applications, particularly to characterize mechanical parameters. The ability of computer vision to detect cracks has been evaluated by many researchers using a variety of materials. Edge detection methodologies have been proven to be able to successfully identify edge-like features on digital images, allowing for detection and localization of cracks in concrete surfaces (Abdel-Qader et al. 2003). Due to inadvertent detection of corrosion, surface textures, component boundaries, and defects, edge detection in metallic materials continues to have a high rate of false positives (Yeum and Dyke 2015).

Research has been conducted to develop algorithms that could remove thick, short, or exceedingly linear edges that are typically not created by cracking, with the goal of creating a reliable crack detection methodology (Yu et al. 2007). Complex algorithms for detecting cracking in asphalt and concrete pavements have been developed by other researchers (Yamaguchi and Hashimoto 2010; Zou et al. 2012; Cha et al. 2017). Typically, asphalt and concrete pavements have larger crack openings than metallic materials, as well as higher contrast between cracked and uncracked regions, meaning that the application of edge detection methodologies to steel bridges is challenging. Additionally, most computer vision studies focus on macro-indicators of damage, such as extensive corrosion, concrete deck deterioration, and large displacements caused by substructure movement. A computer vision strategy to detect fatigue cracks through the tracking of structural surface motion in a video has been developed, but crack tip identification remains a challenge (Kong and Li 2018).

1.2.2 Digital Image Correlation Background

DIC is a subset of computer vision that utilizes medium- to high-resolution cameras and post-processing computer software to analyze images and outputs full-field surface displacement. A three-dimensional strain field can be developed from the full-field surface displacement. DIC software is capable of analyzing both two- and three-dimensional data, depending on how many cameras are utilized during testing. DIC compares a series of images that are collected during loading and generates relative strain and displacement for each point on the image. DIC has been proven to have potential for detecting and characterizing fatigue cracks, but the majority of testing has been limited to simplified test setups, such as in-plane loading or simple geometry.

DIC has been used in the place of tradition sensing methods, such as strain gauges and extensometers, to determine both strain and deformation (Yuan et al. 2014). Crack detection using DIC has been applied to a concrete structure (Küntz et al. 2006) and in the calculation of stress intensity factors (Zhang and He 2012; Hamam et al. 2007). The applications and limitations of 3D DIC have been evaluated using simplified test setups since the mid-1990s (Helm 1996). Test setups with four cameras have been used to determine out-of-plane displacements, but additional cameras result in challenges with the experimental setup and calibration (Chen et al. 2013). A stereoscopic camera setup with a high shutter speed has been used to measure full-field out-of-plane vibrations, but the use of high-speed cameras resulted in a lack of image resolution (Helfrick et al. 2011). Some complex loading scenarios have been tested using clevis fixtures to generate a mixed mode loading on compact (C(T)) test specimens. For Mode I (opening) and Mode II (in-plane shear) loading, DIC displacement results agreed with results developed using finite element analysis of the crack (Sutton et al. 2007).

DIC has been used to evaluate in-plane displacements for a variety of civil infrastructure. A primary application of DIC is to measure deflections of critical bridge members when subjected to service loading. Bridge deflection has been measured from digital videos through a combination of DIC and an inverse compositional algorithm (Pan et al. 2016). This methodology was validated by testing on an in-service railway bridge. An advanced DIC system was used to investigate the deflections of two historic masonry arch bridges under service loads (Dhanasekar et al. 2018). Similar work was performed by Cigada et al. (2014) and Alipour et al. (2019). 3D-DIC has also been used with an unmanned aerial vehicle to examine surface cracking on a concrete bridge (Reagan et al. 2018). While there have been successful applications of DIC for evaluating deflections of in-service structures, challenges to field deployment have been identified, particularly lighting conditions (Ribeiro et al. 2014) and limitations on how large of a distance there is between the camera and the material surface (Lee and Shinozuka 2006).

Extensive research has been performed on applications of DIC for identifying fatigue cracks in metallic materials, but the research has primarily been conducted in an idealized laboratory setting. Studies have examined in-plane fatigue cracking with the goal of identifying and characterizing cracks. In-plane loading studies have been performed on steel C(T) specimens (Rupil et al. 2011), aluminum channels (Vanlanduit et al. 2008), notched tension specimens (Carrol et al. 2009; Carrol et al. 2012), and tension plates with center drilled bolt holes (Lorenzino et al. 2014; Hutt and Cawley 2009). These studies have contributed to understanding the limitations and abilities of DIC for crack detection. Most of these studies, however, focus on qualitative crack identification and characterization, and the development of a quantifiable methodology for automated steel bridge inspections has only been minimally investigated. Additionally, out-of-plane loading conditions have not been as thoroughly researched as in-plane fatigue loading. This

is likely due to the complexity of the test setup required for out-of-plane fatigue loading (Sutton et al. 2007). Work was performed to begin to evaluate how DIC works for complex, out-of-plane test setups, and initial testing found that the developed methodology had the ability to detect and predict the length of distortion-induced fatigue cracks (Dellenbaugh et al. 2020).

1.2.3 Digital Image Correlation Setup

In theory, accurate DIC results are dependent on the specimen preparation, camera setup, calibration, and image collection. The preparation of the specimen primarily refers to the application of a speckle pattern. The ideal pattern is made of consistent dot sizes that are high contrast and random. The speckle pattern is what provides points of reference for the DIC software. Without a speckle pattern, images cannot be compared to evaluate the movement of the specimen. The camera setup depends on the test specimen's complexity and whether two- or three-dimensional analysis is desired. For two-dimensional analysis, one camera will suffice, since no out-of-plane deformations are expected, which allows for a simplified test setup and easier calibration. When testing for out-of-plane displacements, two or more cameras are needed to capture the three-dimensional strain field. Calibration is the process of converting the images from pixels to real dimensions, ensuring realistic evaluation of the specimen. Additionally, calibration accounts for the location of the cameras relative to one another in test setups with two or more cameras. After calibrating, images are collected at a constant interval while the test specimen is being loaded. These images are analyzed using DIC software to determine full-field displacements and stresses.

Chapter 2 Previous Work Overview

2.1 Initial In-Plane Testing

2.1.1 Initial Testing and Methodology Development

To develop an automated fatigue crack inspection methodology, a method for quantifying cracking was needed. The initial methodology was developed using a DIC test setup with a single camera and a C(T) specimen subjected to in-plane loading in a servo-hydraulic testing machine. The C(T) specimen tested was 6.35 mm (0.25 in.) thick and 127 mm (5.0 in.) wide. The specimen size was chosen such that a single specimen could accommodate extensive crack growth and testing at multiple crack lengths. Since bridges are subjected to highly variable loadings, multiple load cases were defined for testing on the C(T) specimen. Stress intensity ranges of 11, 22, 33, 44, and 55 MPa√m (10, 20, 30, 40, and 50 ksi√in) were chosen to emulate realistic bridge loading, and the stress intensity ranges were tested from lowest to highest to limit crack tip plasticity during testing. Images for DIC processing were collected for each loading case at crack lengths of 12.7, 25.4, 38.1, and 50.8 mm (0.5, 1.0, 1.5, and 2.0 in.). The general location of the crack was identifiable through visual inspection of the DIC results, but a methodology to determine the crack length from the DIC data was developed to move towards automation. The twenty data sets for in-plane testing were used to develop a crack length quantification methodology.

2.1.2 Crack Characterization Methodology

Original testing was performed on a C(T) specimen to ensure that the crack location was easily identified. Using the known crack path, the coordinates of the crack path were extended beyond the crack tip, assuming that crack growth would continue linearly. After identifying the crack path, inspection lines were plotted orthogonal to the crack path at consistent intervals along the crack path and projected crack path. From each orthogonal inspection line, two hundred data

points were extracted to determine the relative displacement between the two sides of the crack. The difference between the displacement on either side of the crack was defined as the relative displacement. Relative displacements were plotted along the length of the crack path, and the best fit line for each side of the crack was determined using an algorithm. The relative displacement for each point along the crack path, Δ_i, was divided by the maximum relative displacement for the data set, Δ_{max}. Convergence of the crack was defined as the difference between 100% and the ratio of relative to maximum displacement, shown below as

$$Convergence = 100\% - \frac{\Delta_i}{\Delta_{max}}. \tag{2.1}$$

Theoretically, convergence should equal 100% at the crack tip as there is no relative displacement on either side of the crack, while at the crack opening where relative displacement is the greatest, compliance should equal 0%. However, initial results indicated that this was rarely true, likely due to non-ideal testing conditions, such as speckle pattern and image resolution. Initial testing showed that the crack tip was located at a convergence between 90% and 95%. This was then tested in an out-of-plane test setup to determine the accuracy and efficacy of the developed methodology.

2.2 Distortion-Induced Fatigue Testing

This section discusses the work performed to verify the applicability of the developed methodology to an out-of-plane fatigue crack using a half-scale girder-to-cross-frame subassembly. The initial testing, contained in Section 2.2.1, evaluated a crack along the stiffener-to-web comprised of two vertical segments connected by a short diagonal segment. The same half-scale girder subassembly was then fatigued extensively, resulting in a complex branched crack with four distinct crack paths that were evaluated as described in Sections 2.2.2 and 2.2.3.

2.2.1 Initial Distortion-Induced Fatigue Testing

2.2.1.1 Initial Distortion-Induced Fatigue Test Setup and Loading

After the crack characterization methodology was developed using a simplified in-plane C(T) specimen, the methodology was evaluated on a crack developed on a half-scale girder-to-cross-frame subassembly. The test specimen was an I-shaped plate girder subassembly fabricated from A36 steel. The half-scale girder had a length of 2845 mm (112 in.), a depth of 917 mm (36.1 in.), and a web thickness of 10 mm (0.375 in.). To approximate the axial stiffness provided by the concrete deck attached to the top flange of a girder, the top of the girder subassembly was connected to the reaction floor of the laboratory, which prevented the top flange from experiencing out-of-plane motion. A cross-frame was installed at the mid-span of the girder, which was attached through a connection plate welded only to the girder web.

The girder was loaded out-of-plane by applying a vertical displacement to the far end of the cross-frame, producing a distortion-induced fatigue crack. Fatigue cracking was initiated in the web-gap region between the connection plate and the flange. A fatigue crack was initiated and propagated on the girder through loading for 21,000 cycles at a load range of 2.2 to 25.5 kN (0.5 to 5.75 kips). This crack spanned between the connection plate weld and the girder web and contained two vertical segments connected by a short diagonal segment, all of which were idealized as linear. The crack was measured to have a total length of 44.5 mm (1.75 in.).

A loading protocol was developed for the out-of-plane testing to have varying and realistic loads that simulate the varying traffic loads that bridges are subjected to. Realistic loading levels were determined using a finite element model of a bridge based on the full-scale proportions of the testing setup. Realistic differential vertical deflections between adjacent girders were determined by applying the AASHTO fatigue truck. On the full-scale finite element model, the

differential deflection was 2.54 mm (0.1 in.), so the target differential deflection for the half-scale test setup was 1.25 mm (0.05 in.), which corresponds to an actuator load of 6.6 kN (1.5 kips) applied to the end of the cross-frame. Seven load cases were defined for loads above and below the target load. All loading cases had a minimum applied load of 0.89 kN (0.2 kip) to simulate the dead load of the bridge, and the load cases had a maximum applied load of 2.2, 4.4, 6.7, 8.9, 11.1, 13.3, and 15.6 kN (0.5, 1.0, 1.5, 2.0, 2.5, 3.0, and 3.5 kips).

2.2.1.2 Initial Distortion-Induced Fatigue DIC Configuration

The main difference between the DIC configuration for in-plane C(T) testing and distortion-induced fatigue testing is that out-of-plane testing requires the use of a two-camera stereo setup, rather than a single camera (see fig. 2.1a and b). A speckle pattern was applied to the fatigue susceptible region to provide reference points for the DIC processing (see fig. 2.1c). For the purpose of processing the DIC data, the web-to-flange weld was defined as the x-axis, the stiffener-to-web weld was established as the y-axis, and the z-axis was located along the direction of the cross-frame.

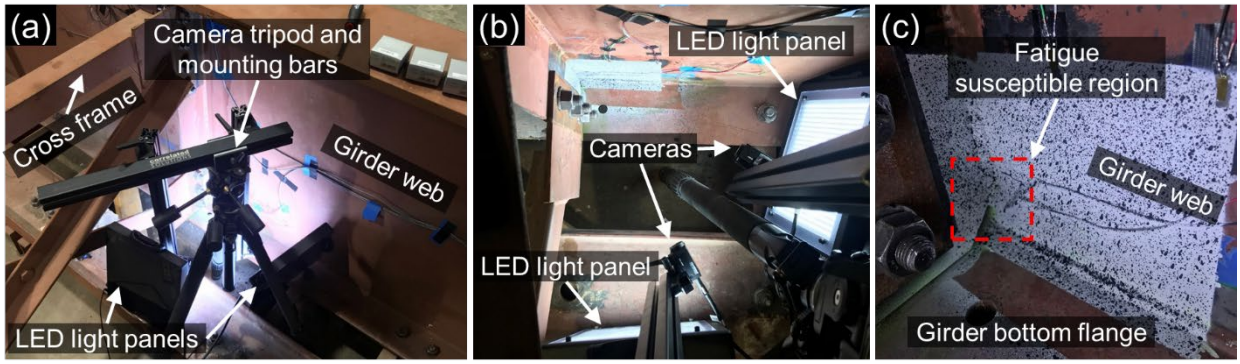

Figure 2.1 (a) Hardware locations for out-of-plane testing, (b) hardware orientation as seen from above, and (c) fatigue susceptible region with speckle pattern applied

2.2.1.3 Initial Distortion-Induced Fatigue Crack Characterization Methodology

The same methodology was used to analyze distortion-induced fatigue specimens as the in-plane specimens. For the initial analysis of distortion-induced fatigue cracks, the displacement values along the z-axis were used to determine convergence. Despite the more complicated geometry, the crack path could be determined through visual inspection of the DIC displacement contours. Orthogonal lines were drawn along the length of the crack in the web gap region. The relative displacements were determined for the entire length of the crack and extended beyond the crack tip. Convergence was calculated for the out-of-plane cracking in the same manner as the in-plane crack using equation 2.1.

The relative displacements for the load case ranging from 0.89 to 2.2 kN (0.2 to 0.5 kip) were very small for the entirety of the crack length, which resulted in large variations in convergence. The high variability of the convergence indicates that the developed methodology is not applicable at low load levels. This applicability threshold will need to be investigated further in future testing.

Because the C(T) specimen testing resulted in typical convergences of 90% to 95%, the known crack length for the distortion-induced fatigue specimen was compared to the 90% and 95% convergence values to determine the accuracy of the developed DIC results. The optically measured crack length was 44.5 mm (1.75 in.). The 90% convergence values tended to under-predict the crack length. On average, the 90% convergence value corresponded to a 40.6 mm (1.59 in.) crack, which is 9% lower than the actual crack. The 95% convergence tended to over-predict the crack length, but only by an average of 1%, corresponding to a predicted crack length of 45.0 mm (1.77 in.). This indicated that the developed methodology for crack length determination was accurate for simple out-of-plane cracks.

2.2.2 Complex Branched Distortion-Induced Fatigue Crack Methodology

An important constraint for applications to DIC is the complexity of crack that is capable of being analyzed. Testing was performed using the same test setup as the simple distortion-induced fatigue crack that was used for initial verification of the developed methodology (see fig. 2.1). For DIC to be implementable in the field, the methodology must be adequate for detection of any distortion-induced fatigue crack found on in-service structures. DIC was evaluated for its ability to quantify a complex, branched, distortion-induced fatigue crack.

2.2.2.1 Complex Branched Crack Pattern

To develop a complex, branched crack, the girder was loaded cyclically at a load range of 2.2 to 25.5 kN (0.5 to 5.75 kip) for approximately 1,700,000 cycles (Al-Salih et al. 2021). During cyclic loading, two fatigue cracks propagated in the web-gap region; vertically along the connection plate-to-web weld and horizontally along the web-to-flange weld. The vertical crack along the connection plate-to-web weld also branched into the web in two locations. The overall crack pattern is shown in figure 2.2a) with white lines drawn over the fatigue crack locations for clarity. For evaluation, the bifurcated cracks were evaluated as three separate cracks. Each of the four crack designations, paths, and lengths are summarized in table 2.1.

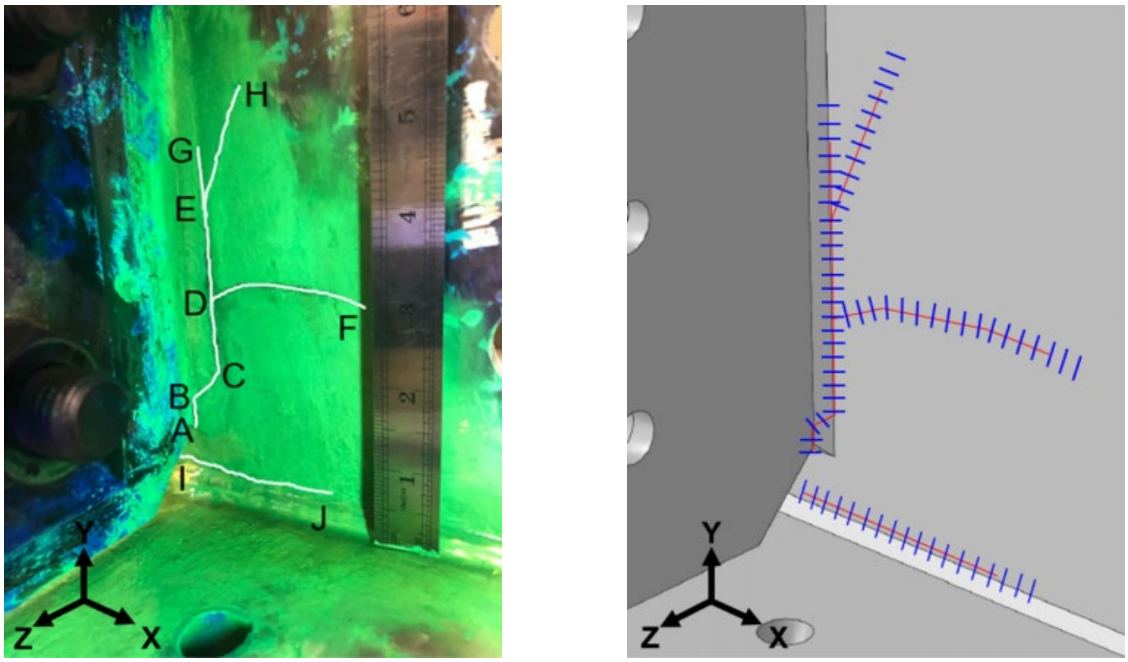

(a) (b)

Figure 2.2 (a) Fatigue cracks in web-gap region and (b) schematic of crack path with orthogonal data extraction lines

Table 2.1 Crack designations and lengths

Crack Name	Crack Path	Crack Length, mm (in.)
Vertical Crack	A-B-C-D-E-G	104.9 (4.14)
Branched Crack I	A-B-C-D-F	111.9 (4.41)
Branched Crack II	A-B-C-D-E-H	138.6 (5.45)
Horizontal Crack	I-J	51.0 (2.00)

2.2.2.2 Complex Branched Crack Data Collection Loading

A loading protocol had to be developed to achieve realistic loads for out-of-plane testing. To this end, a finite element model of a full-scale bridge that matched the half-scale girder proportions was developed. The bridge was loaded with the AASHTO fatigue truck and the differential vertical deflections between adjacent girders were determined. For the full-scale model, the differential deflection was 2.6 mm (0.102 in.), meaning that the target deflection for the half-

scale model was 1.3 mm (0.051 in.). To achieve the desired deflection, an actuator load of 7.8 kN (1.75 kips) was applied (Dellenbaugh et al. 2019). Eleven load cases (LC) for DIC data collection were defined with maximum loads above and below the target load, ranging from 2.2 to 24.5 kN (0.5 to 5.5 kips). The range in maximum load represented the variable loads that bridges are subjected to. For each load case, a minimum load of 0.9 kN (0.2 kip) was applied to simulate the dead load acting on the bridge. The load and displacement ranges for each of the eleven load cases is shown in table 2.2.

Table 2.2 Out-of-plane load cases

Load Case	**Load Range, kN (kips)**	**Displacement Range, mm (in.)**
LC1	0.9 – 2.2 (0.2 – 0.5)	0.025 – 0.046 (0.001 – 0.002)
LC2	0.9 – 4.4 (0.2 – 1.0)	0.025 – 0.074 (0.001 – 0.003)
LC3	0.9 – 6.7 (0.2 – 1.5)	0.025 – 0.965 (0.001 – 0.038)
LC4	0.9 – 8.9 (0.2 – 2.0)	0.025 – 1.651 (0.001 – 0.065)
LC5	0.9 – 11.1 (0.2 – 2.5)	0.025 – 2.464 (0.001 – 0.097)
LC6	0.9 – 13.3 (0.2 – 3.0)	0.025 – 3.302 (0.001 – 0.130)
LC7	0.9 – 15.6 (0.2 – 3.5)	0.025 – 4.141 (0.001 – 0.163)
LC8	0.9 – 17.8 (0.2 – 4.0)	0.025 – 4.902 (0.001 – 0.193)
LC9	0.9 – 20.0 (0.2 – 4.5)	0.025 – 5.741 (0.001 – 0.226)
LC10	0.9 – 22.2 (0.2 – 5.0)	0.025 – 6.553 (0.001 – 0.258)
LC11	0.9 – 24.5 (0.2 – 5.5)	0.025 – 7.315 (0.001 – 0.288)

2.2.2.3 Crack Characterization Methodology

The crack characterization methodology used to analyze the complex, multi-segment distortion-induced fatigue crack was similar to the developed methodology used on the in-plane testing and the simple out-of-plane crack methodology. DIC images were analyzed using coordinate transformation. The *x*-axis was defined as parallel to the web-to-flange weld, the *y*-axis follows the connection plate-to-web weld, and the *z*-axis is in the direction of the cross-frame,

shown in figure 2.2. Displacements in all three directions were analyzed due to the complex geometry of the test setup and the crack. Representative DIC results for each of the three displacements are shown in figure 2.3.

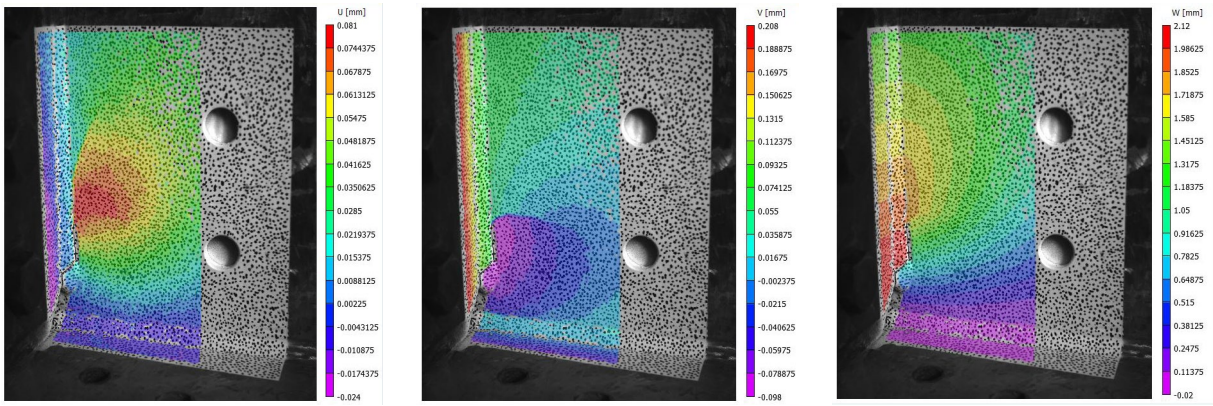

(a) (b) (c)

Figure 2.3 Representative DIC results for (a) U-displacement along the *x*-axis, (b) V-displacement along the *y*-axis, and (c) W-displacement along the *z*-axis

Due to the complexity of the crack, edge detection algorithms were not able to clearly detect the path of the crack. The crack paths were visually identified using dye penetrant in the loaded condition. The raw displacement data was then analyzed following the developed methodology. Orthogonal inspection lines were drawn along the crack length, extending beyond the perceived crack tip. Relative displacements between the complex crack boundaries were calculated for each segment of the crack from the orthogonal lines. The differential displacements were used to determine convergence for each crack segment using equation 2.1.

2.2.3 Complex Branched Distortion-Induced Fatigue Crack Results

Figure 2.4 shows the different strains obtained by the DIC software for the complex crack pattern. The majority of the crack pattern is clearly visible in the strain images with the exception

of the last segment of the vertical crack, segment E-G, which was also difficult to visually detect. While the von Mises strain (figure 2.4f) showed the majority of the crack pattern, an important note is that this computation does not convey differences between tensile and compression regions of the crack. For example, the region surrounding the web-to-flange crack in figure 2.4f) is shown in red, but it is representative of compressive stresses, rather than tensile. A finite element study found that the web-to-flange weld crack is under compression on the connection plate side and under tension on the fascia side (Liu et al. 2015). Similarly, the maximum principal strain is only capable of providing a clear picture of the entire crack pattern when combined with the minimum principal strain.

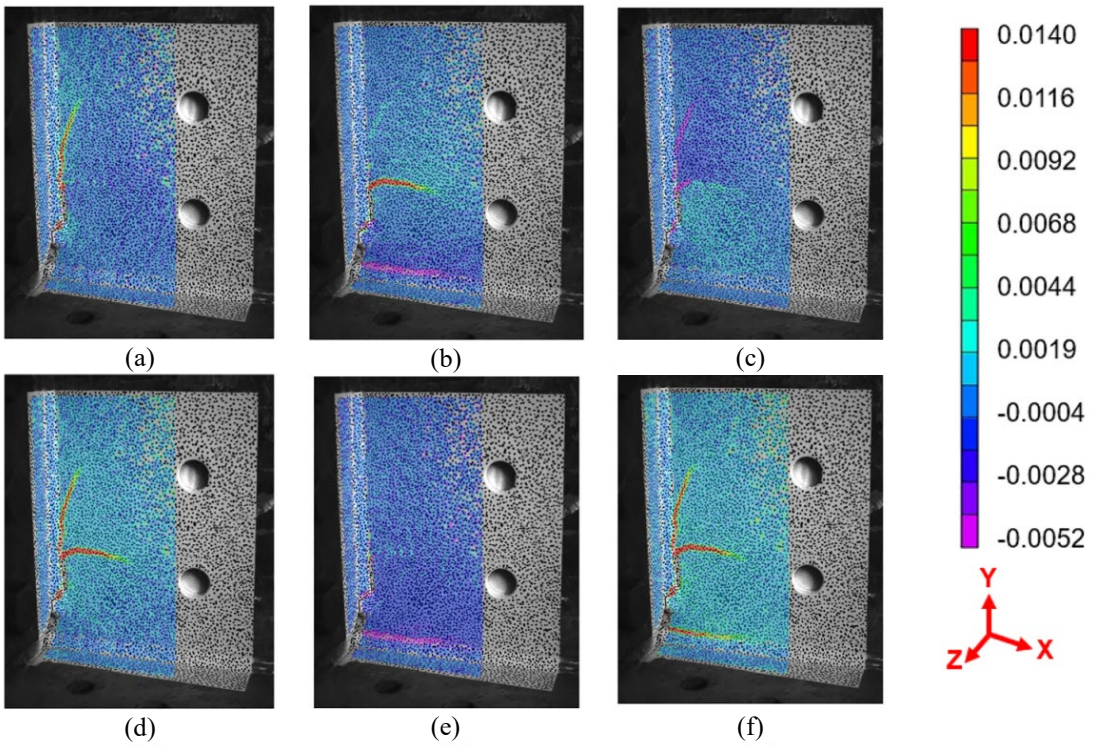

Figure 2.4 Typical visualized DIC strains: (a) strain in *x*-axis; (b) strain in *y*-axis; (c) strain in *xy*-plane; (d) max principal strain; (e) min principal strain; (f) von Mises strain

As previously described, differential displacements were computed along data extraction lines arranged orthogonal to the crack path, and convergence for those displacements values was calculated along the length of the crack path. Due to the complex geometry of the crack and the web-gap region, displacements in all three principal directions were examined using DIC. Additionally, the resultant differential displacement was calculated and evaluated for the crack characterization methodology. The resultant displacement produced very similar trends and magnitudes to the W-displacement since the W-displacement magnitude was significantly higher than the U- and V-displacement. Therefore, results based on the resultant displacement are not discussed in this report. Additionally, as the primary displacements were in the *yz*-plane, the U-displacement was found to have a significantly smaller magnitude than V- and W-displacements, creating a highly variable convergence curve for most loading cases. Therefore, the U-displacement data was not considered to be a useful indicator of crack location for this crack pattern.

The approach applied here was found to perform well under a broad range of applied loads, but a threshold to its applicability was identified as occurring at the lowest magnitude load case studied (LC1). Relative displacements in all the three directions measured under LC1 were extremely small, resulting in highly variable convergence values and indicating that the displacement-driven process was ineffective at this low load. Thus, this level of loading was identified as the threshold of applicability in the development of this approach. Data from LC1 is presented graphically in relative displacement and convergence plots, but is excluded from crack characterization methodologies. It should be noted that for most load cases, the relative displacements values in all the three directions approached zero well before the known crack tip location, resulting in an underprediction of crack length at 90% and 95% convergence values. For

this reason, crack lengths at convergence values of 98% were also examined. Since both the 90% and 95% convergence data underpredicted crack length, the 90% convergence data was excluded from this report. The crack characterization results for each of the four crack segments are summarized in the following sections.

2.2.3.1 Vertical Crack Characterization Results

The relative W- and V-displacements corresponding to the *z*- and *y*-directions for the vertical crack are presented visually in figures 2.5(a) and (c), respectively, with convergence curves for the same directions shown in figures 2.5(b) and (d). The length of the crack at segments B, C, D, E, and G, as determined through traditional visual inspection, are represented by the vertical dotted lines in the figures. In the *y*-direction, both relative displacement and convergence display a step-like trend for the diagonal second crack segment, B-C. This is caused by the low amount of vertical relative displacement occurring in the vertical segments on either side of B-C, compared with the much larger amount of vertical displacement within this segment.

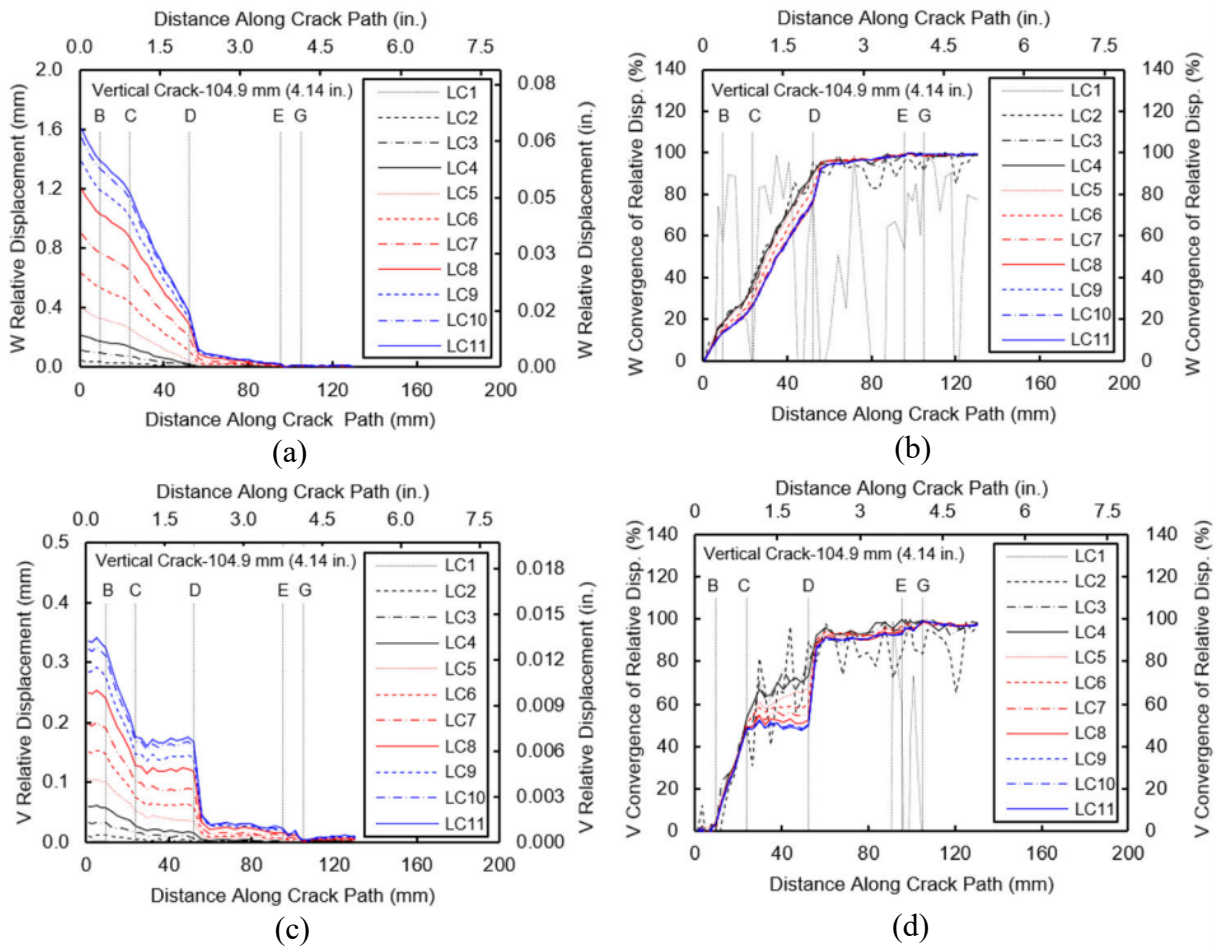

Figure 2.5 Vertical Crack: (a) relative W-displacement; (b) convergence of relative W-displacement; (c) relative V-displacement; (d) convergence of relative V-displacement

The 95% convergence values underpredicted the vertical crack lengths by an average of 42% based on the W-displacement and 17% based on the V-displacement. The 98% convergence resulted in a better prediction of the Vertical Crack length, with an average underprediction of 17% based on the W-displacement and 5% based on the V-displacement. For load cases 6 through 11, with maximum forces between 13.3 to 24.5 kN (3.0 to 5.5 kip), the 98% convergence crack length was accurate to within 1%.

2.2.3.2 Branched Crack I Characterization Results

The relative displacement and convergence values based on W- and V-displacements for Branched Crack I are shown in figure 2.6. The length of actual crack segments B, C, D, and F are represented by vertical dotted lines in the figures. Again, the results based on V-direction displacement produce a step in the relative displacement and convergence curves for segment B-C. This flat section is again caused by the large vertical displacements in the diagonal segment relative to the two vertical crack segments surrounding it.

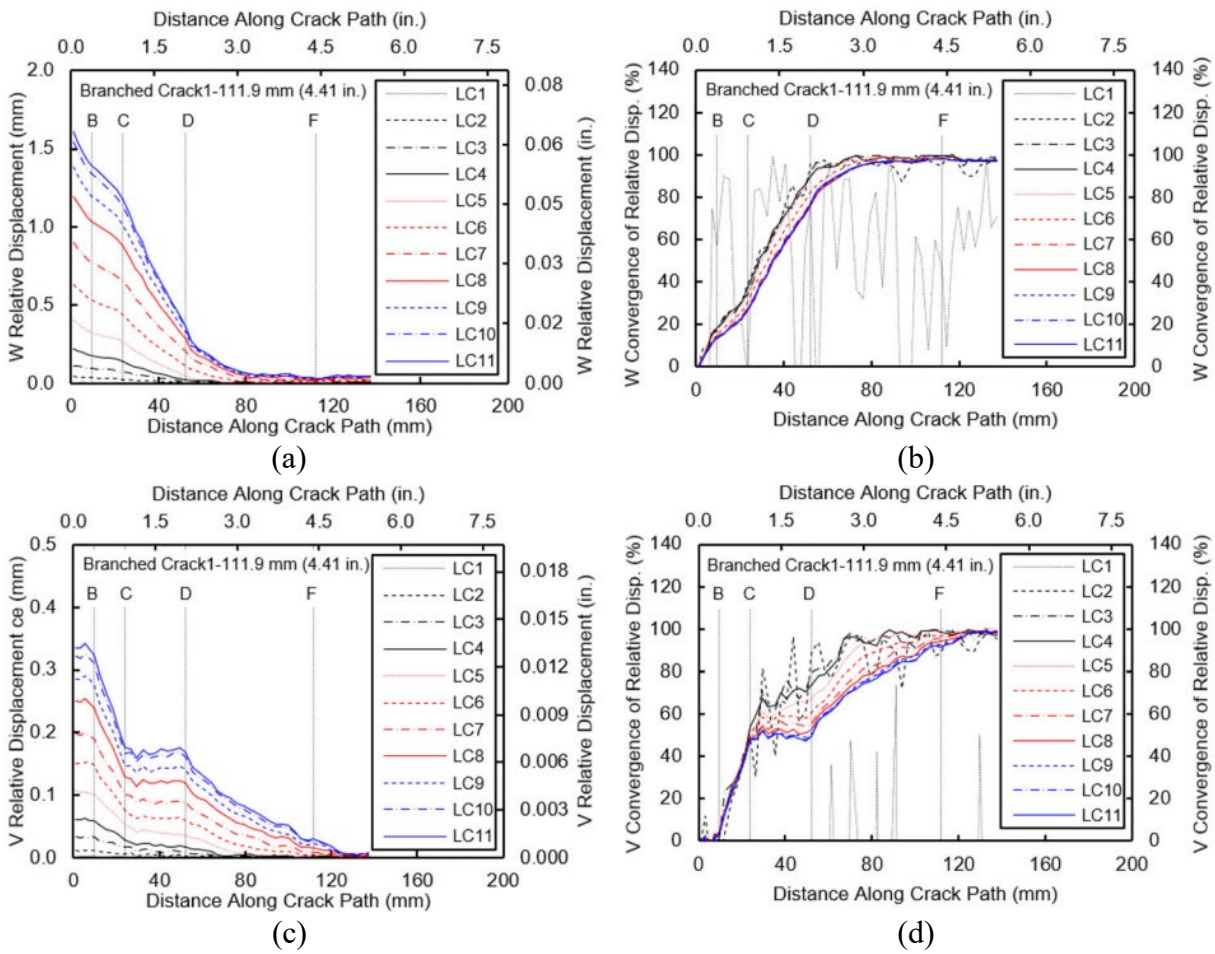

Figure 2.6 Branched Crack I: (a) relative W-displacement; (b) convergence of relative W-displacement; (c) relative V-displacement; (d) convergence of relative V-displacement

Evaluating crack lengths at 98% convergence resulted in significantly less error based on W-displacement, with an average crack length across all eleven load cases of 111.4 mm (4.39 in.), an error of less than 1%. Individual load cases all have errors greater than 1% however, with an absolute average error of 13%. The 98% convergence results based on V-displacement are similar to the 95% convergence results, with load cases 2 through 6 underestimating crack length by 30% to 40% while crack length estimates from load cases 7 through 11 are accurate to within 6%. Due to the significant underestimation of the low load cases, the average error in the crack length estimate based on V-displacement is 19% for 98% convergence.

2.2.3.3 Branched Crack II Characterization Results

The relative displacements and convergence values for Branched Crack II are shown in figure 2.7. The vertical dotted lines in the figures represent the lengths of the actual crack segments B, C, D, E, and H. Again, there is a step-like trend for the vertical segment B-C for the relative V-displacement and convergence due to the low relative vertical displacements for this segment. Although segment E-H is not perfectly vertical, the step-like trend is also seen for this segment for the same reason. This was confirmed by experimental observations, which indicated that the crack opening in segment E-H was very small and difficult to measure with dye penetrant.

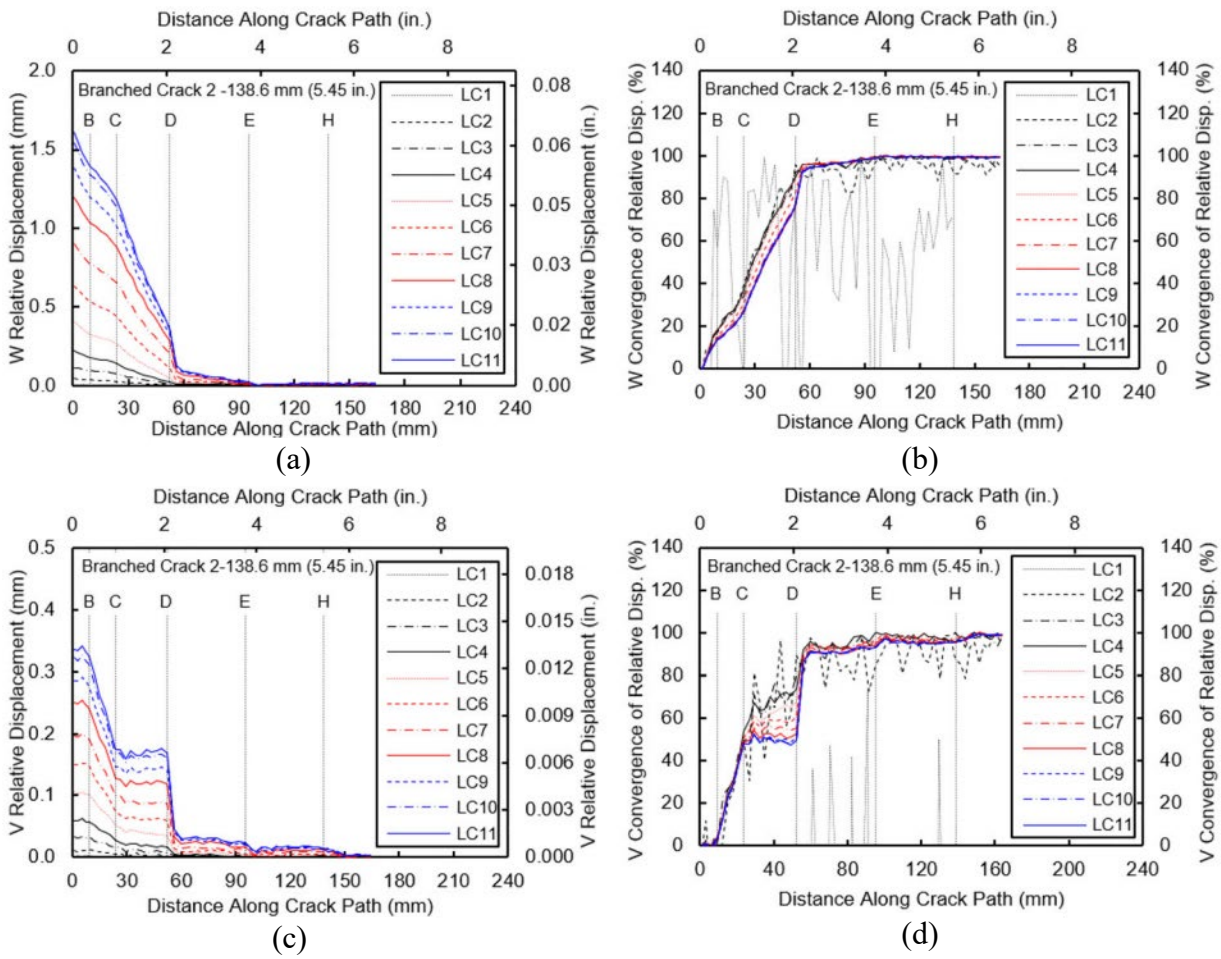

Figure 2.7 Branched Crack II: (a) relative W-displacement; (b) convergence of relative W-displacement; (c) relative V-displacement; (d) convergence of relative V-displacement

Based on W-displacement, both the 95% and 98% convergence results significantly underpredicted the crack length regardless of load case. The average error was 56% and 39% for the 95% and 98% convergence, respectively. Similarly, the crack length was underestimated based on V-displacement for 95% convergence by an average of 37%. For the 98% convergence, the average crack length estimate is 123.2 mm (4.85 in.), an underestimation of 11%. The crack estimates for load cases 7 through 11 are slightly overestimated by approximately 5%, leading to an average absolute error of 17%.

2.2.3.4 Horizontal Web-to-Flange Crack Characterization Results

The relative displacement and convergence values based on the V-direction for the horizontal web-to-flange crack are shown in figure 2.8. The vertical dotted line in the figures represents the length of the actual web-to-flange crack of 51 mm (2.0 in.), based on visual inspection. The horizontal web-to-flange crack exhibited a high level of noise and did not converge well compared to the other cracks on the girder. U-, W-, and R- displacements were all found to be very noisy and did not approach the 95% convergence values expected. For the V-direction, over half of the displacement data sets did not approach 95% convergence.

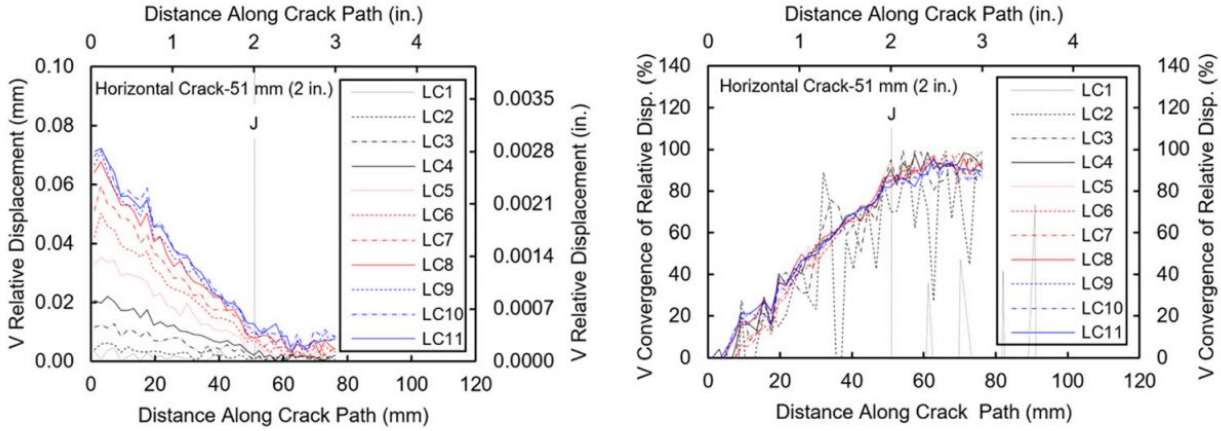

(a) (b)

Figure 2.8 Horizontal web-to-flange crack: (a) relative V-displacement; (b) convergence of relative V-displacement

There are multiple explanations for the difficulty in characterizing the horizontal crack. First, relative displacements between the crack boundaries were very small. For example, the maximum relative W-displacements for the horizontal crack were found to be 0.08 mm (0.003 in.), compared to 1.6 mm (0.06 in.) for vertical and branched cracks. This corresponds with experimental observation, where the opening of the horizontal web-to-flange crack was extremely

small and nearly invisible, making it very difficult to detect during visual inspection. Second, as discussed previously with regard to the strain visualization results, the horizontal crack is under compression on the interior side of the girder, producing crack closure under loading rather than opening. This behavior was confirmed with finite element analyses that showed the horizontal crack is under compression on the interior side of the girder and under tension on the fascia side. For these reasons, the horizontal web-to-flange was not able to be well-characterized using this DIC-based methodology, with convergence values never reaching 95% or 98%. The average convergence at the crack tip was 70% based on W-displacement and 86% based on V-displacement.

2.2.3.5 Complex Branched Distortion-Induced Fatigue Crack Summary

Figure 2.9 shows a visual summary for the predicted crack lengths and the corresponding percent error for the Vertical Crack, Branched Crack I, and Branched Crack II. Figure 2.9(a) shows the absolute average percent errors between the predicted and actual crack lengths for 95% and 98% convergence, while Figure 2.9(b) shows the predicted crack lengths based on the 95% and 98% convergence for relative V- and W-displacements. The dotted lines represent the actual crack lengths.

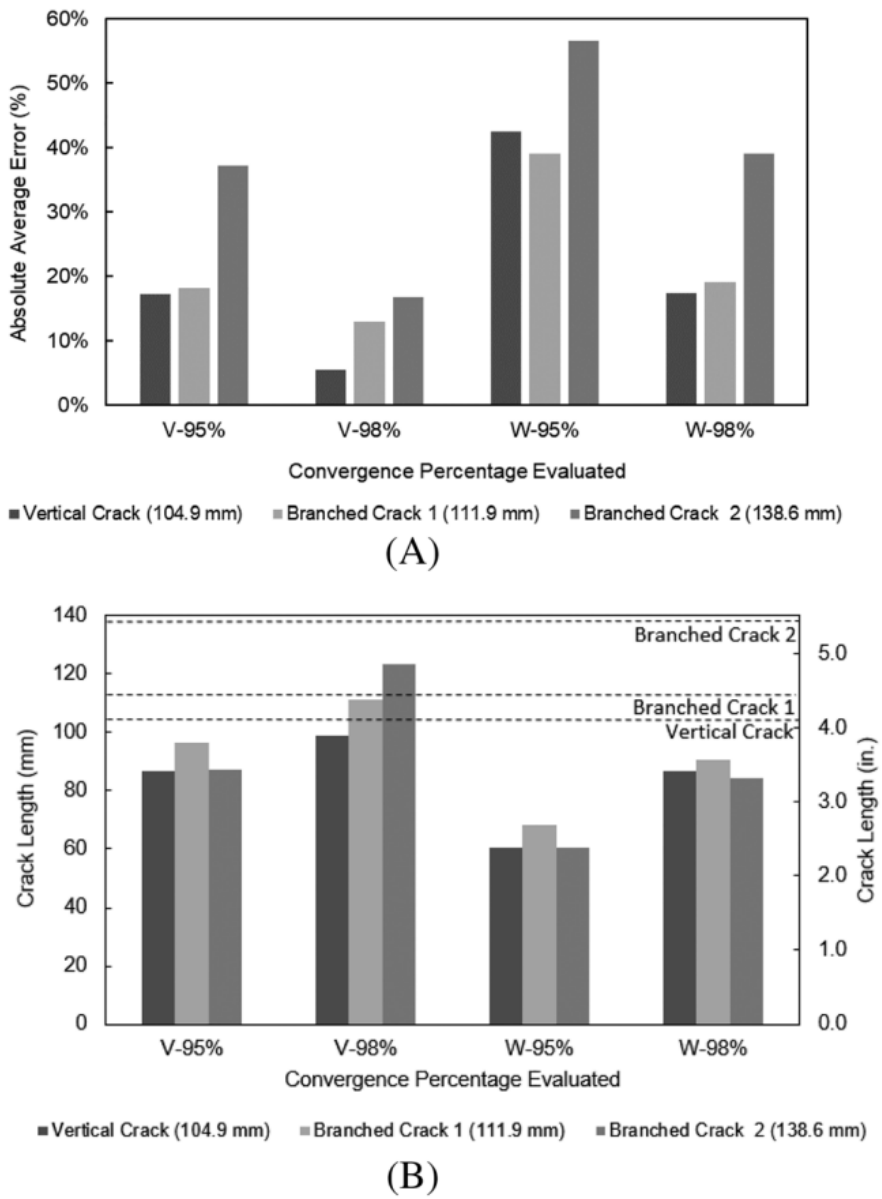

Figure 2.9 (a) Absolute average percent error between predicted and actual crack lengths for 95% and 98% convergence for relative V- and W-displacement; (b) predicted crack lengths based on 95% and 98% convergence for relative V- and W-displacement

For the Vertical and Branched cracks, the crack length estimates from 98% convergence exhibited reduced error compared to 95% convergence. It can also be seen that the crack length estimates based on V-displacement are more accurate than those based on W-displacement. For each crack, LC1, 2, and 3 produced very little crack opening, resulting in higher levels of error

when calculating convergence. The loading threshold where crack length prediction error approaches 10% appears to be between LC4 and LC5 for the Vertical Crack, LC5 and LC6 for Branched Crack I, and LC6 and LC7 for Branched Crack II. Lower load ranges did not produce crack opening along the full crack length, making it difficult to detect the displacement difference occurring at the crack tip, which resulted in crack length underestimation.

2.3 Advancements Towards Automation

This section summarizes previous work performed on evaluating the ability of the developed crack detection methodology to be automated. A more robust and automated process would allow for a diversity of image collection methods and reduce the time required to evaluate each potential crack. Section 2.3.1 describes the lighting and focus condition study. The aperture testing is described in Section 2.3.2. Open-source DIC alternatives that have the potential to be adapted to use in fatigue crack detection are presented in Section 2.3.3. Finally, Section 2.3.4 contains a study on the effectiveness of a single camera in detecting an out-of-plane crack using the distortion-induced fatigue crack test setup.

2.3.1 Lighting and Focus Testing

The accuracy of DIC output is dependent on the preparation of the specimen, camera setup, calibration, and image collection. Work performed during year one was primarily proof-of-concept and was applied under idealized conditions. For DIC to be implementable in the field, the system and methodology needs to be robust enough to handle the varying conditions found on in-service structures. The objective of this study was to evaluate the ability of the developed DIC methodology to characterize an in-plane crack under non-idealized lighting and camera focus conditions.

2.3.1.1 Lighting and Focus Test Setup, Loading, and Conditions

Light and focus testing was performed on steel C(T) specimens loaded in a uniaxial servo-hydraulic loading frame, similar to the testing to develop the in-plane methodology. The fatigue crack investigated had the same four crack lengths used in the initial testing, but loading was redefined to achieve stress intensity ranges of 11, 16, 22, 27, and 33 MPa√m (10, 15, 20, 25, and 30 ksi√in). These load cases are respectively designated LC1 through LC5. The five load cases were modified from year one testing to limit plasticity at the crack tip and to provide a more realistic loading range.

Three lighting conditions and three focus conditions were defined. High light was the brightest light possible from two external LED lamps being set to the maximum brightness, which created an overexposed image with a washed-out speckle pattern. Medium light and low light were approximately 70% and 30% of the high light condition, respectively. Ideal lighting would occur at approximately 85% of the high light condition, meaning that all lighting conditions were non-ideal, based on a range of lumens for each lighting condition.

The crack characterization methodology was developed for a camera distance of 216 mm (8.5 in.). Two additional camera distance, 432 and 648 mm (17.0 and 25.5 in.), were evaluated in this study. At each of the three camera distances, the ideal focus and two additional levels of focus resulting in a 5% and 10% reduction from the ideal focus, respectively, were chosen for testing. Using the uncertainty estimate from the DIC software, ideal focus was defined as having an uncertainty of 0.0003 mm (0.00001 in.) or better under the high lighting condition. Focus was initially varied by manually adjusting the rotation of the camera's focus ring. However, the focus ring used does not measure rotation, therefore an alternative definition for quantifying focus had to be developed. Focus was redefined in terms of camera distance from the specimen. By first

focusing the camera at the ideal distances of 216, 432, and 648 mm (8.5, 17.0, and 25.5 in.), the camera was then moved closer to the specimen, reducing the focal length by 5% and 10% to create the fair and poor focus conditions, respectively. The uncertainty estimates for the fair and poor focus conditions were 0.0007 and 0.0010 mm (0.00003 and 0.00004 in.), respectively.

Six combinations of lighting and focus conditions were evaluated for each of the three camera distances for in-plane crack lengths of 12.7, 25.4, 38.1, and 50.8 mm (0.5, 1.0, 1.5, and 2.0 in.). Appendix A details all the testing conditions defined for each camera to specimen distance. All six of testing condition combinations evaluated were sub-optimal, ignoring the recommended calibration needs of the DIC system.

2.3.1.2 Lighting and Focus Testing Results

DIC data was collected for varying crack lengths and lighting and focus conditions. Typical outputs from the DIC software for LC5 with a crack length of 25.4 mm (1.0 in.) and a camera-to-specimen distance of 648 mm (25.5 in.) are shown in figures 2.10 and 2.11, showing conditions 1 and 5, respectively.

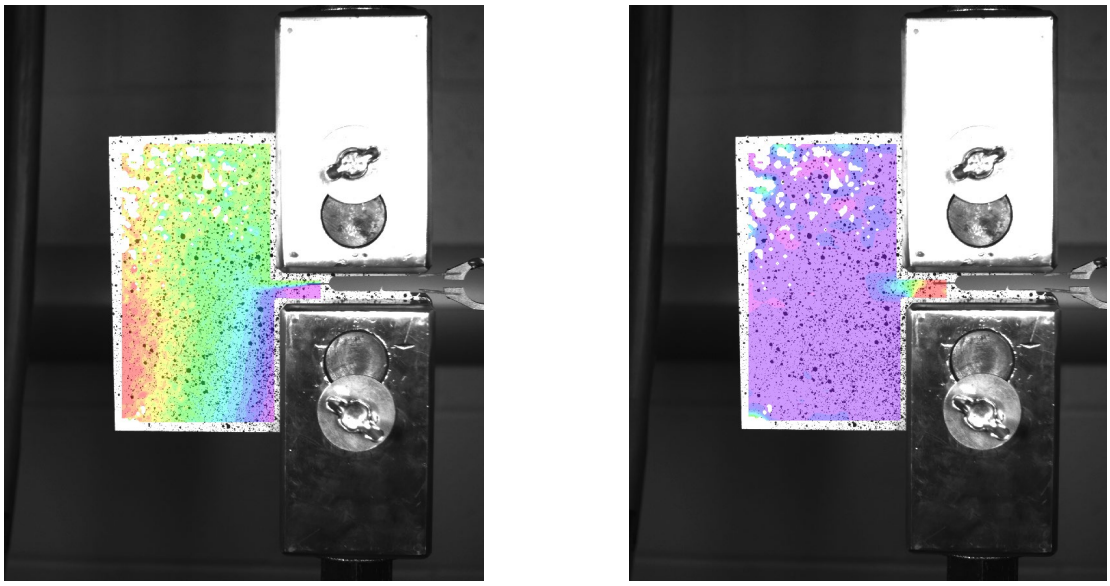

(a) (b)

Figure 2.10 DIC results for a 25.4 mm (1.0 in.) crack with 648 mm (25.5 in.) camera distance under LC5 and Condition 1 in terms of (a) displacement and (b) strain

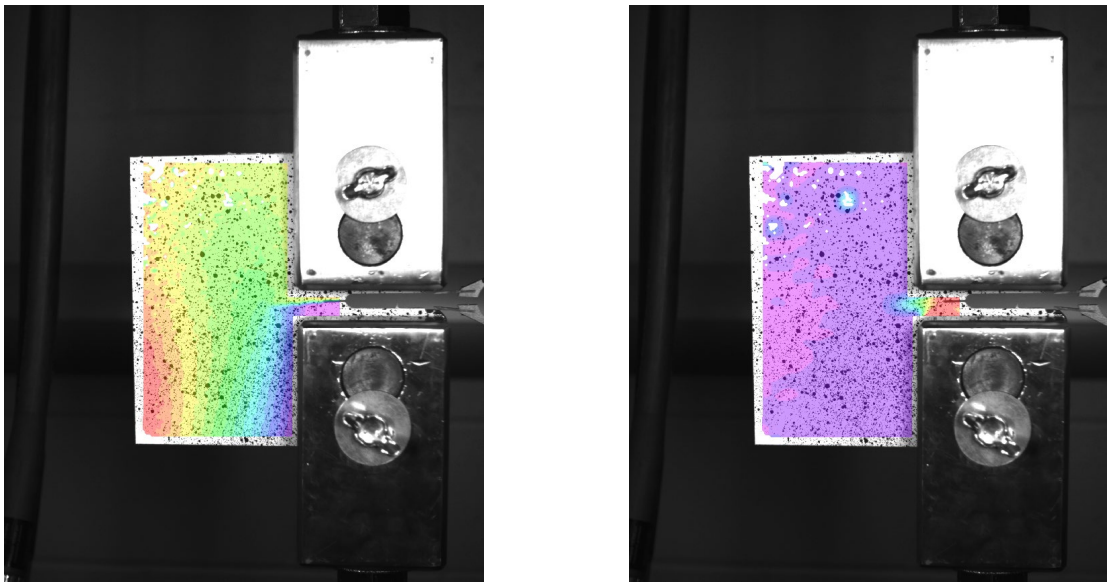

(a) (b)

Figure 2.11 DIC results for a 25.4 mm (1.0 in.) crack with 648 mm (25.5 in.) camera distance under LC5 and Condition 1 in terms of (a) displacement and (b) strain

The expected deflections for C(T) specimens are exclusively in-plane, so relative displacements perpendicular to the crack path were utilized in accordance with the developed crack characterization methodology to calculate the convergence. Due to the distance between the camera and the specimen, the crack was frequently not clearly visible in the DIC strain and displacement data images. Representative relative displacement and convergence values are shown in figures 2.12 and 2.13 for LC5. In each plot, the vertical dotted line represents the actual crack length, as verified through specimen compliance and visual observation. Relative displacement and convergence plots for additional crack lengths, load cases, and camera distances are shown in Appendix A. The high, medium, and low light conditions are denoted using HL, ML, and LL, respectively, while the ideal, fair, and poor focus conditions are denoted by IF, FF, and PF, respectively. Thus, the first condition combining high light and ideal focus is termed HLIF.

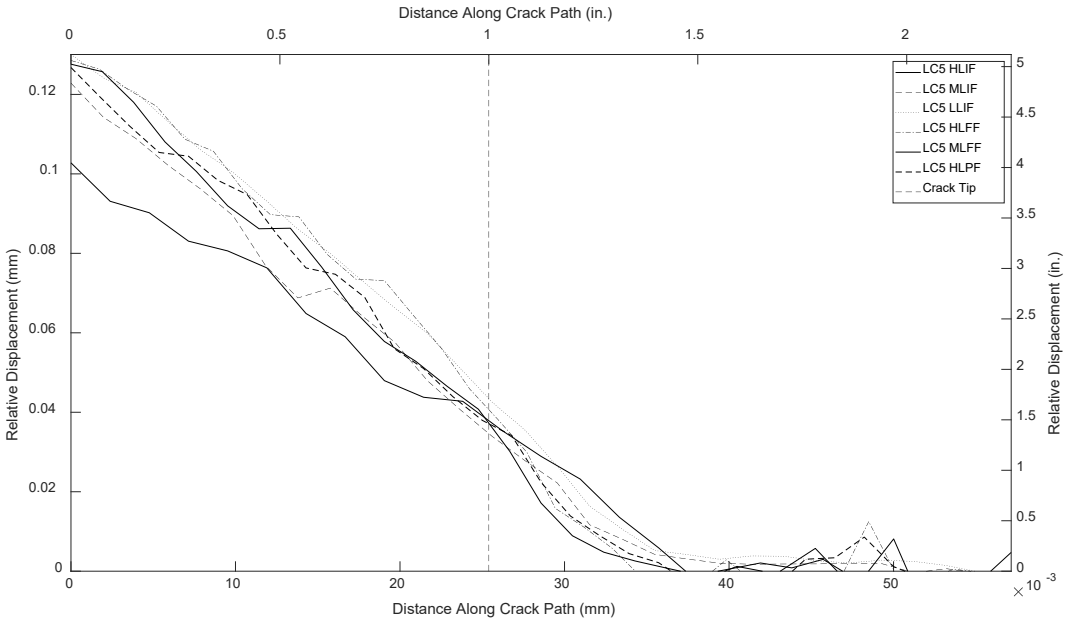

Figure 2.12 Relative displacement of a 25.4 mm (1.0 in.) crack under LC5

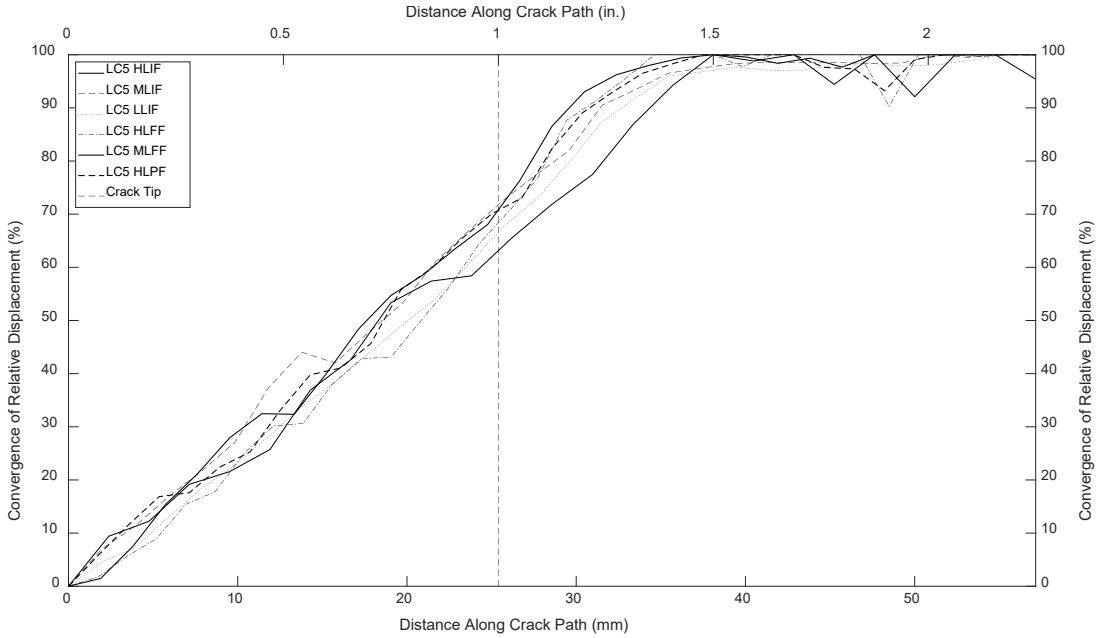

Figure 2.13 Convergence of relative displacement of a 25.4 mm (1.0 in.) crack under LC5

Convergence values for each lighting and focus condition combination were averaged across all five load cases for a crack length of 25.4 mm (1.0 in.) and camera distance of 648 mm (25.5 in.) and are compared to the ideal case in table 2.3. The convergence for each condition and load case is shown visually in figure 2.14. Because of the modified loading cases from the initial methodology development, the non-ideal cases can only be directly compared with the ideal results for load cases 1, 3, and 5. The lines are presented for clarity.

Table 2.3 Average convergence at 25.4 mm (1.0 in.) crack tip for 648 mm (25.5 in.) camera distance

Light and Focus Condition	Average Convergence	Difference
Ideal	92.6%	N/A
1	71.5%	21.1%
2	72.3%	20.3%
3	69.6%	23.0%
4	73.3%	19.3%
5	66.2%	26.4%
6	73.1%	19.5%

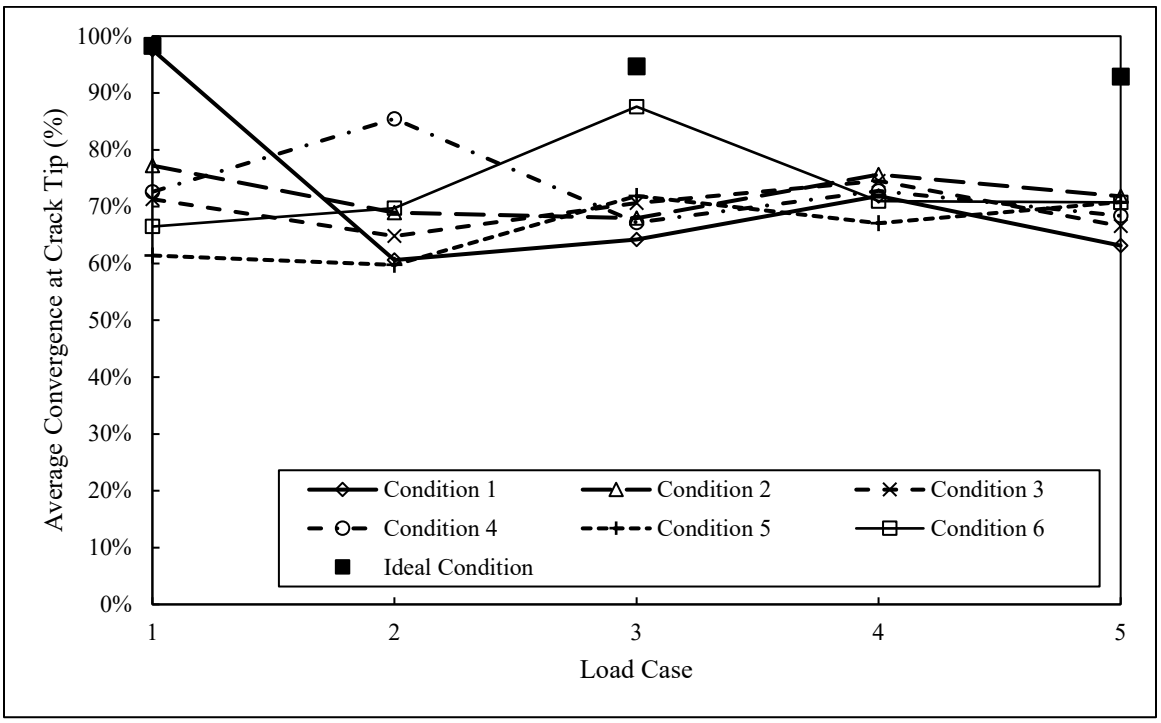

Figure 2.14 Average convergence at crack tip for each load case and condition for a crack of 25.4 mm (1.0 in.) with a camera to specimen spacing of 648 mm (25.5 in.)

Convergence values for non-ideal conditions exhibit significant variability compared to the results from the ideal test conditions. While the non-ideal conditions resulted in a significant decrease in crack convergence and DIC output quality, the presence of a crack was still detected.

This indicates that sub-optimal conditions may not result in accurate crack length measurements, but can be used to detect cracks and flag them for further inspection. Similar results were seen for all crack lengths and camera to specimen distances. Additional information on lighting and focus condition testing can be found in Juno (2020).

2.3.2 Study on the Impact of Aperture

Aperture is a measure of how open the lens of a camera is. This is the component that controls the physical amount of light allowed into the camera. Aperture is defined based on the "f-stop" number, where f/1.4 allows a large amount of light into the camera and f/11 or higher lets a very small amount of light in. Figure 2.15 shows a comparison between different aperture values on a C(T) specimen with a camera to specimen distance of 305 mm (12.0 in.). All photographs were taken with the same external lighting conditions, from the same location, and have no post-processing or editing.

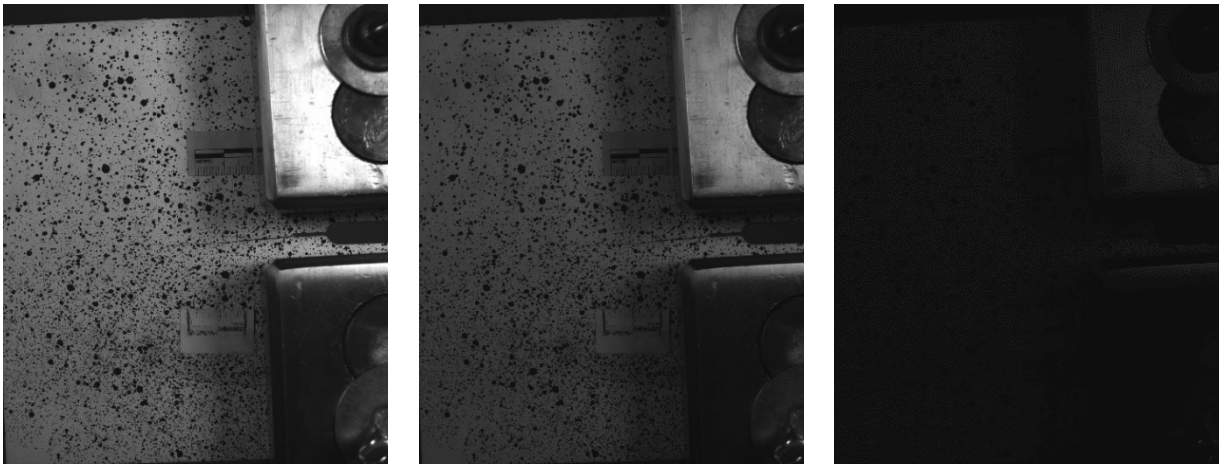

(a) (b) (c)

Figure 2.15 C(T) specimen photographed with apertures of (a) f/2.8; (b) f/4; and (c) f/11

Aperture also has some impact on the depth of the field of the camera. The larger the camera opening is, the smaller the depth of field is, and the closer the camera would need to be to the specimen. Some cameras have lenses that can automatically adjust aperture, but the cameras utilized in this study must be changed manually, making understanding the impact of the aperture on DIC results important.

2.3.2.1 Aperture Test Setup and Loading

Testing for the impact of aperture was performed on the same C(T) specimen after the conclusion of the lighting and focus study, so it was performed on a single crack length of 50.8 mm (2.0 in.) under LC5. Images were collected for four different camera-to-specimen distances and for four different aperture values with idealized light and focus conditions. The four camera-to-specimen distances were 203, 305, 457, and 610 mm (8.0, 12.0, 18.0, and 24.0 in.). Data was collected for apertures of f/1.4, f/2.8, f/4, and f/11, but due to low light and poor quality of the f/4 and f/11 images, only images taken with apertures of f/1.4 and f/2.8 were analyzed using DIC

2.3.2.2 Aperture Study Results

A convergence plot for the 50.8 mm (2.0 in.) crack with a camera distance of 203 mm (8.0 in.) and an aperture of f/1.4 is shown in figure 2.16. The camera distance and aperture setting almost exactly match the initial testing performed on the C(T) specimen, and results in a similar convergence seen in previous testing. This convergence plot is representative of the remaining seven combinations of camera distance and aperture, which are presented in Appendix A. Convergence plots for the other conditions displayed more noise near the middle of the crack, but the amount of noise did not seem to vary with aperture setting or camera distance. The aperture of f/2.8 resulted in higher convergence values for all camera distances except for 305 mm (12.0 in.) as shown in table 2.4.

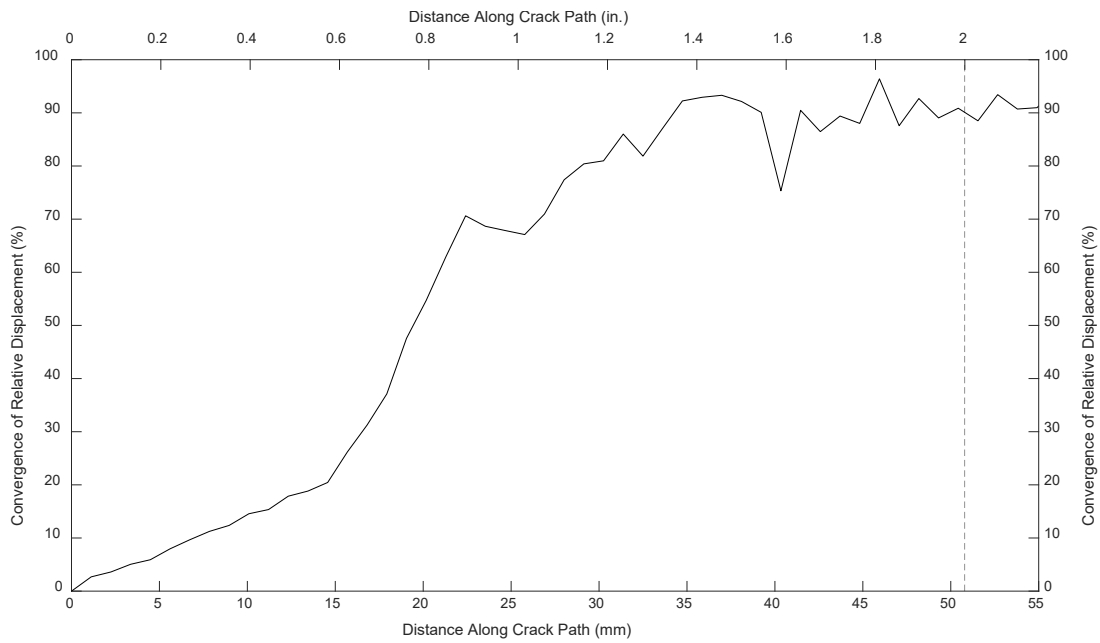

Figure 2.16 Convergence of relative displacement of a 50.8 mm (2.0 in.) crack with a camera distance of 203 mm (8.0 in.) and an aperture of f/1.4 under LC5

Table 2.4 Convergence of 50.8 mm (2.0 in.) crack under varying camera distances and aperture conditions

Camera to Specimen Distance, mm (in.)	**Aperture Setting**	
	f/1.4	**f/2.8**
203 (8.0)	90.1%	95.0%
305 (12.0)	84.9%	78.1%
457 (18.0)	74.7%	87.4%
610 (24.0)	79.3%	82.9%
Avg.	82.3%	85.9%

Aperture could potentially serve to correct for non-ideal lighting and focus conditions. Additional research will need to be performed to evaluate exactly how much aperture impacts the quality of the focus of images. Other than this brief investigation, all testing has been performed with an aperture of f/1.4, which is the largest aperture possible on the cameras used for testing.

Using a camera with an automatically focusing lens and an adjustable aperture could help to simplify the test setup required on a UAV and result in higher quality images.

2.3.3 Investigation into Open-Source DIC Alternatives

Open-source software has the potential to allow for more flexible analysis of DIC data. Additionally, open-source software could allow for different data collection methods, without the need for specialized, idealized test setups. This is important for the development of an accessible inspection system. In this study, three viable open-source alternatives were identified and assessed using the existing data sets.

2.3.3.1 Open-Source Software Alternatives

The International DIC Society (2018) has identified several open-source programs that have been developed by the research community and made available to fellow researchers. Of the options presented, three emerged as potentially viable alternatives for use in automated bridge inspections: *Ncorr*, Augmented Lagrangian DIC (*ALDIC*), and DICengine (*DICe*). There were additional options that were feasible for analyzing fatigue cracks on steel bridge members, but only these three alternatives were investigated deeper than surface level due to incompatible operating systems, lack of knowledge of the software language, or lack of software documentation. These three open-source alternatives were used to analyze both in- and out-of-plane cracks using images obtained during the development of the crack characterization methodology. The results obtained from these open-source software packages are shown in Appendix A.

Ncorr is a 2D DIC program developed by the Georgia Institute of Technology in Georgia, United State (Blaber et al. 2015). Designed to address a lack of user friendly alternatives, *Ncorr* is written entirely in MATLAB and features a high-quality graphical user interface (GUI). It introduces a Eulerian to Lagrangian conversion to attempt to analyze areas of discontinuities in

displacement fields. When discontinuities are detected, the software creates a region of interest around it and then performs DIC on that area. Interpolation and a nonlinear optimization algorithm then determine the best fit for the areas with missing data. This has the potential to prove useful in images with poor focus or lighting conditions or with gaps in data due to non-ideal speckle pattern application. The built in user interface also includes contour plotting tools for visualizing the data quickly.

Developed by the California Institute of Technology in California, United States, *ALDIC* is a 2D DIC code also written in MATLAB (Yang and Bhattacharya 2020). It combines the speed and non-iterative analysis of local DIC and the displacement compatibility and smoothness of global DIC approaches. *ALDIC* utilizes subsets locally to determine multiple smaller displacement fields and then applies a compatibility requirement for global analysis to ensure that there are no gaps or discontinuities in the displacement field without drastically increasing computation time.

DICe is a 2D and 3D DIC alternative written in C++ developed by the Sandia National Laboratories in New Mexico, United States (Turner 2015). It allows the user to choose between local and global DIC analysis methods and can also be applied in the tracking of rigid body motion. Like *Ncorr*, it is presented with an intuitive GUI, but does not feature the easy to use contour plotting options. Instead, output strain and displacement fields must be visualized using separate software or a free open-source data visualization application such as ParaView.

2.3.4 Distortion-Induced Fatigue Crack Single Camera Testing

One of the constraints for applying the developed DIC testing methodology on in-service highway bridges is the limitations of an Unmanned Aerial Vehicle (UAV). The test setup for the developed methodology required two cameras, additional lighting panels, and highly idealized testing conditions. Reducing the number of cameras needed to one would allow for a simplified

testing setup as well as less weight acting on the UAV. The objective of this research was to evaluate the ability of a single camera to detect complex, distortion-induced cracking.

2.3.4.1 Single Camera Test Setup and Loading

DIC post-processing was performed using the original images collected during the initial out-of-plane distortion-induced fatigue testing. Images were obtained with a stereo camera setup, but were processed individually to provide two single-camera data sets with different angles. The crack pattern was made up of three linear segments, shown in figure 2.17. The loading cases used were the same seven that were used for initial testing, with maximum forces ranging from 2.2 to 15.6 kN (0.5 to 3.5 kip), shown in table 2.5. All loading cases had a minimum applied load of 0.9 kN (0.2 kip) to simulate the dead load of the bridge.

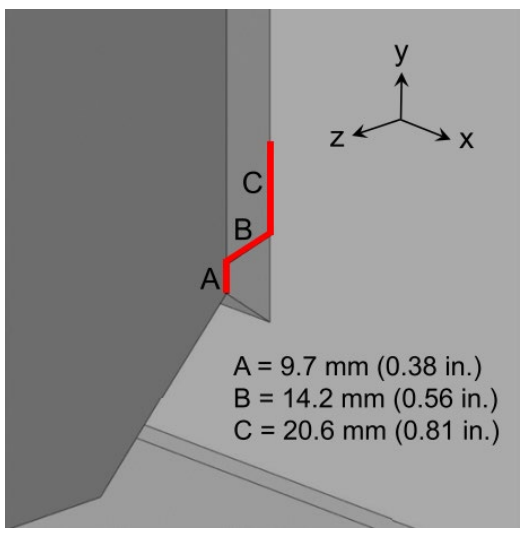

Figure 2.17 Crack location and geometry

Table 2.5 Single camera out-of-plane loading cases

Load Case	Load Range, kN (kip)	Displacement Range, mm (in.)
LC1	0.9 – 2.2 (0.2 – 0.5)	0.025 – 0.046 (0.001 – 0.002)
LC2	0.9 – 4.4 (0.2 – 1.0)	0.025 – 0.074 (0.001 – 0.003)
LC3	0.9 – 6.7 (0.2 – 1.5)	0.025 – 0.965 (0.001 – 0.038)
LC4	0.9 – 8.9 (0.2 – 2.0)	0.025 – 1.651 (0.001 – 0.065)
LC5	0.9 – 11.1 (0.2 – 2.5)	0.025 – 2.464 (0.001 – 0.097)
LC6	0.9 – 13.3 (0.2 – 3.0)	0.025 – 3.302 (0.001 – 0.130)
LC7	0.9 – 15.6 (0.2 – 3.5)	0.025 – 4.141 (0.001 – 0.163)

Post-processing of the images was performed in the VIC-2D software. While the original post-processing compared both images to determine an *x*-, *y*-, and *z*-axis relative displacement, the single camera testing found *x*- and *y*-axis relative displacement, U and V, respectively, for each camera angle, shown in figure 2.18. The data from a single camera was then used to find convergence of relative displacement along the crack length. This was compared to the original convergence values to determine if a single camera can capture the complex crack location.

(a) (b)

Figure 2.18 Cracked web gap region as seen from (a) camera 1 and (b) camera 2

2.3.4.2 Single Camera Results

The ability of a single camera DIC setup to capture the behavior of a complex, out-of-plane crack is highly dependent on the load case and which axis displacement is being evaluated on. Load cases 1 and 2 resulted in high amounts of noise in both the 2D and 3D setup, which made characterizing the crack challenging. Additionally, the results from the relative displacement in the V-direction was highly variable, with convergence frequently jumping and falling along the length of the crack. This can be seen visually for LC7 in figure 2.19. Plots for load cases 1 through 6 are shown in Appendix A. The blue vertical lines represent the transition between different segments of the 44.5 mm (1.75 in.) crack and the crack tip. The red line shows the original data when processed using VIC-3D software. Crack estimates from the U-displacement are accurate for segments B and C of the crack, but do not detect segment A.

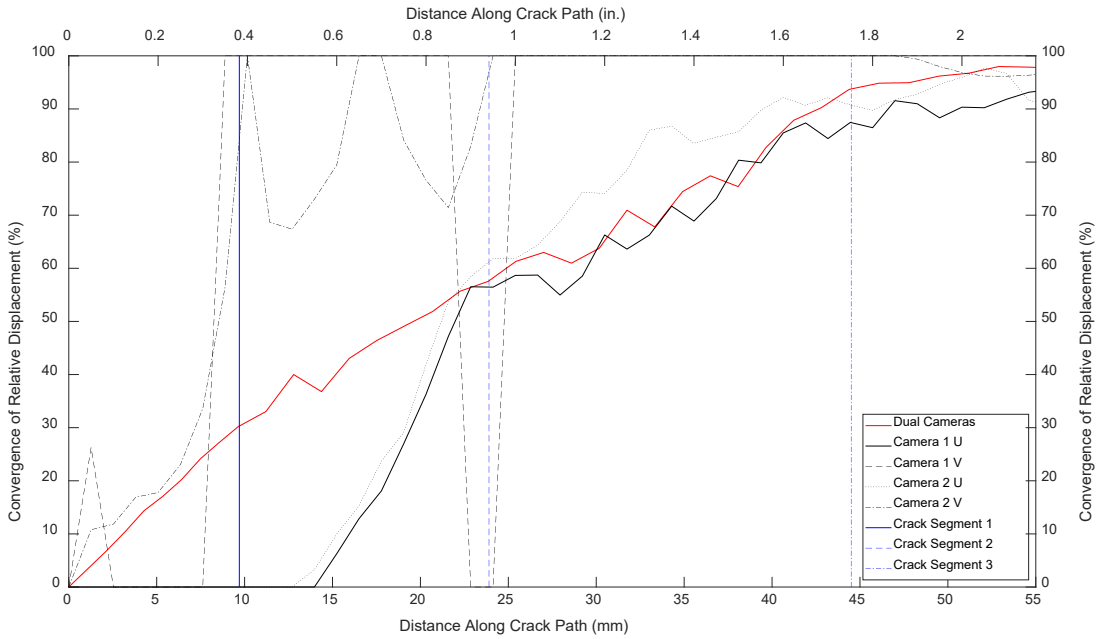

Figure 2.19 Convergence of relative displacement of a 44.5 mm (1.75 in.) complex crack under LC7

Another challenge with a single camera is that results are dependent on the camera angle. Table 2.6 shows the convergence at the crack tip based on relative U-displacement for both cameras and the change in convergence from the 3D analysis. For both 2D and 3D analysis, LC1 resulted in very noisy convergence plots that reached 100% convergence well before the crack tip, indicating a minimum threshold for applicability. As such, results for LC1 are not shown in table 4.2. For load cases 2 through 7, the average convergence for camera 1 was 90.7%, while the average convergence for camera 2 was 90.9%. Compared to the average convergence from 3D analysis of 94.1%, cameras 1 and 2 had an average error of 3.39% and 3.22%, respectively. These results indicate that the 2D 95% convergence would overestimate the crack length.

Table 2.6 Convergence at 44.5 mm (1.75 in.) crack tip from U-displacement

Load Case	**3D**	**Camera 1**		**Camera 2**	
	Convergence	**Convergence**	**Difference**	**Convergence**	**Difference**
LC2	91.8%	93.9%	2.10%	91.8%	0.00%
LC3	97.4%	88.5%	-8.98%	92.3%	-5.13%
LC4	90.0%	90.4%	0.46%	97.4%	7.47%
LC5	95.6%	90.6%	-5.01%	90.5%	-5.12%
LC6	96.1%	90.2%	-5.87%	86.2%	-9.83%
LC7	93.9%	90.8%	-3.06%	87.2%	-6.68%
Avg.	**94.1%**	**90.7%**	**-3.39%**	**90.9%**	**-3.22%**

Average convergence for both cameras based on V-displacement was much higher than for U-displacement, but this was primarily due to the convergence jumping to 100% early along the crack path and remaining there, indicating that convergence in the V-direction was not an effective indicator of crack length regardless of the camera angle. Therefore, results for the V-direction are not shown in this report.

Initial results show that a single camera can detect the behavior of the crack path but is highly dependent upon the direction of the analysis, the camera angle, and the load that the crack is subjected to. Additional research will be needed to determine exactly how important camera angle is when utilizing a single camera, particularly since angle was not measured during this testing. While the camera that captured the crack behavior was looking "directly" at the crack, it was not quantified and was highly subjective. Single-camera DIC results should be evaluated more thoroughly, particularly under varying light and focus conditions, and different UAV alternatives should be assessed to determine whether a UAV would be equipped to carry a stereo camera setup.

Chapter 3 Cantilever Overhead Sign Structure Fatigue Crack Testing

3.1 Cantilever Overhead Sign Structure Fatigue Crack Test Setup and Loading

3.1.1 Cantilever Overhead Sign Structure Background

Cantilever overhead sign structures (COSS) are commonly employed to convey information to highway travelers in the United States. COSS can use between one and four horizontal mast-arms and several connection details between the arms and the vertical pole have been used over the years. In particular, COSS with two mast-arms using a box connection, similar to the one shown in figure 3.1, have been shown to have increased susceptibility to fatigue failures in the state of Kansas. This fatigue detail was characterized using DIC to detect crack initiation, whereas previous crack detection testing used fatigue cracks that had already propagated to at least 12.7 mm (0.5 in.). This study determines the lower threshold of crack length for the applicability of DIC in fatigue crack detection.

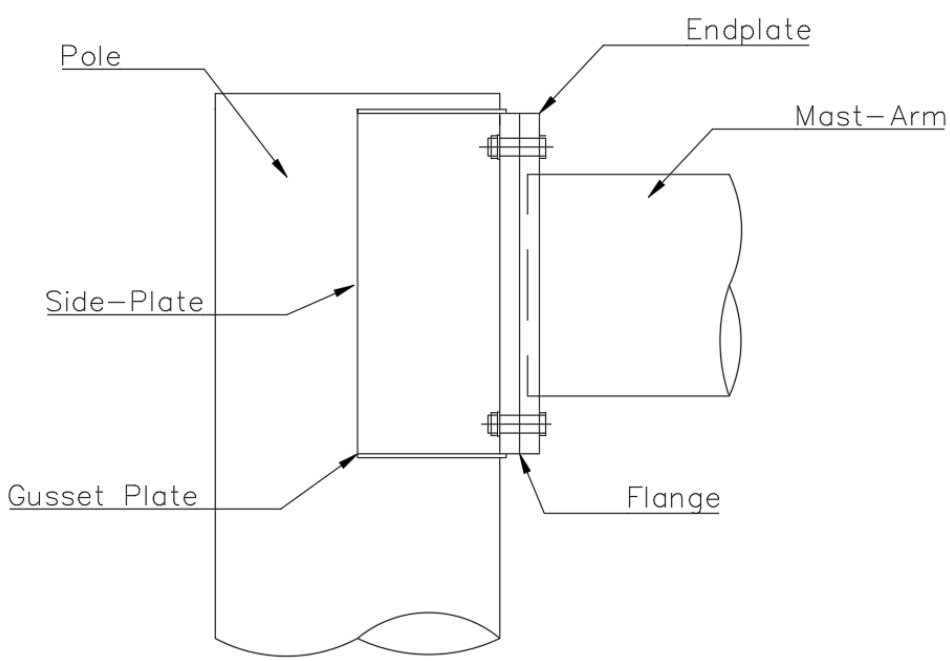

Figure 3.1 Schematic of a COSS box connection

3.1.2 Cantilever Overhead Sign Structure Fatigue Crack Test Setup

The COSS box connection detail was categorized using six sub-sized poles with a single mast-arm that were modified from a 1981 Kansas Department of Transportation (KDOT) tapered design. The pole, arm, and baseplate dimensions for the full-size COSS and the sub-size test specimens are given in table 3.1. Note that the baseplate is square, so only the width and thickness are shown. Because this design uses a pole that is tapered at 1.17 cm/m (0.14 in/ft), the pole diameter varies at the box connection. For the test specimens, a straight pole with a 45.7 cm (18.0 in.) diameter was chosen for ease of fabrication.

Table 3.1 COSS dimensions

Geometry	Full-Size Structure	Test Specimen
Pole Height, m (ft)	**7.92 (26.0)**	**2.59 (8.50)**
Pole Diameter, cm (in.)	**Varies**	**45.7 (18.0)**
Pole Thickness, mm (in.)	**7.94 (0.3125)**	**9.53 (0.375)**
Arm Length, m (ft)	**9.45 (31.0)**	**2.13 (7.00)**
Arm Diameter, cm (in.)	**33.0 (13.0)**	**35.6 (14.0)**
Arm Thickness, mm (in.)	**7.94 (0.3125)**	**11.8 (0.465)**
Baseplate Width, cm (in.)	**67.3 (26.5)**	**76.2 (30.0)**
Baseplate Thickness, mm (in.)	**63.5 (2.50)**	**50.8 (2.00)**

Test specimens were installed by bolting the baseplate down to a strong floor system using Superbolt multi-jackbolt tensioners. A servo-hydraulic actuator was attached to a support girder that was then attached to the strong wall system. The actuator was oriented orthogonal to the mast-

arm and attached to the end of the mast-arm using two plates with semi-circular cuts that were bolted together. Figure 3.2 shows schematics of the test setup and figure 3.3 shows a picture of the first specimen after installation.

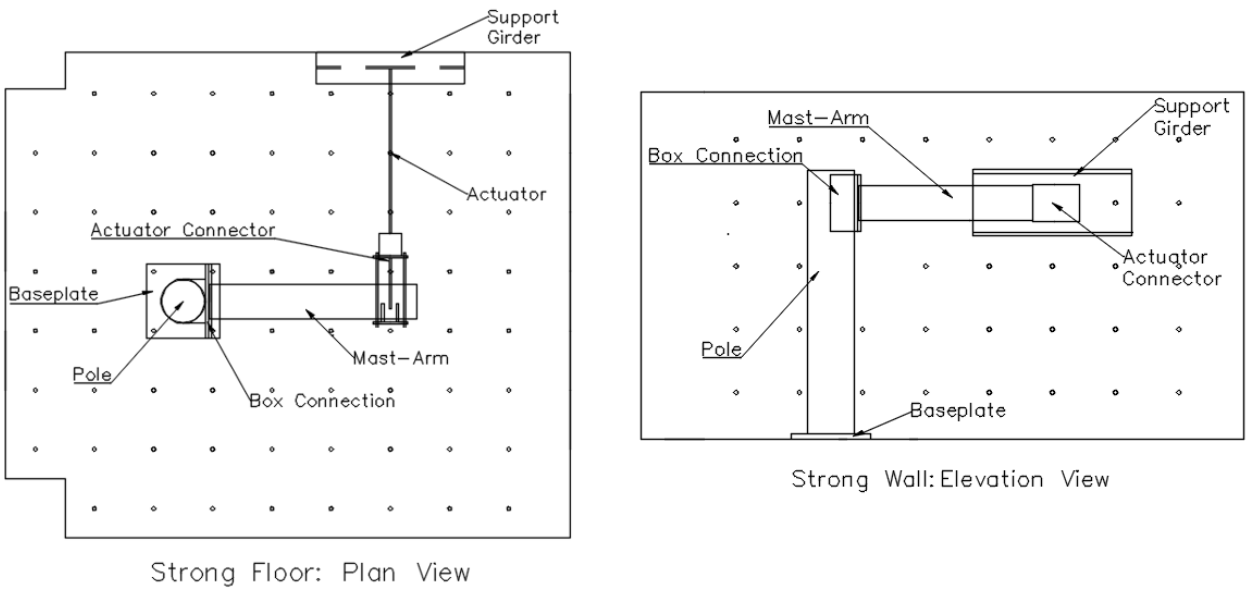

Figure 3.2 Schematic of the COSS test setup

Figure 3.3 COSS test specimen

3.1.3 Cantilever Overhead Sign Structure Fatigue Crack Loading

The test specimens were loaded cyclically by retracting the actuator, applying a tensile point load at the end of the mast-arm. This resulted in bending of the mast-arm and Mode 1 loading on the mast-arm-to-flange and the box-to-pole welds. The COSS also experienced bending and torsion in the pole, causing a mixed Mode 1 and 3 condition at the baseplate-to-pole weld.

To determine the load that should be applied by the actuator for the first specimen, the stress at the box connection was considered to be purely in bending, as the differential torsional stresses at the weld would be of negligible magnitude. The initial bending stress was chosen to be 68.9 MPa (10 ksi), matching the AASHTO Category C constant amplitude fatigue threshold for

infinite life. The equation for bending stress was rearranged to solve for the required actuator force range, F, shown below as

$$F = \frac{\sigma \cdot I}{L \cdot c}. \tag{3.1}$$

Here, σ is the bending stress range of 68.9 MPa (10 ksi), I is the moment of inertia of the pole of 10,280 cm^3 (679 in^3), L is the distance between the point of load application and the centerline of the pole, approximately 213 cm (84.0 in.), and c is the distance to the extreme fiber of the pole, equal to the radius of 22.9 cm (9.0 in.).

This resulted in a force range for the first specimen of 40.0 kN (9.0 kip). For the remaining five specimens, the force range was scaled by 1/2, 3/8, or 1/4 to provide fatigue categorization data at several stress ranges. Cycles were applied at either 0.5 or 1.0 Hz depending on load range and the number of cycles left until fatigue crack initiation was expected. All six specimens were loaded with a minimum force equal to one-tenth of the maximum force. Full load reversals were not done to avoid instability when applying compression. The actuator minimum and maximum load and nominal stress ranges at the box connection are summarized in table 3.2.

Table 3.2 COSS load and box connection stress ranges

Specimen Number	Actuator Load Range kN (kip)	Box Connection Stress Range MPa (ksi)
1	**4.45 – 44.5 (1.00 – 10.0)**	**68.9 (10.0)**
2	**2.22 – 22.2 (0.50 – 5.00)**	**34.5 (5.00)**
3	**1.11 – 11.1 (0.25 – 2.50)**	**17.2 (2.50)**
4	**2.22 – 22.2 (0.50 – 5.00)**	**34.5 (5.00)**
5	**1.67 – 16.7 (0.375 – 3.75)**	**25.9 (3.75)**
6	**2.22 – 22.2 (0.50 – 5.00)**	**34.5 (5.00)**

3.2 Cantilever Overhead Sign Structure Fatigue Crack Detection

3.2.1 DIC System Configuration and Specifications

In addition to the box connection weld, the mast-arm-to-flange and baseplate welds were identified as potential hotspots for fatigue cracks. Prior to testing, a high contrast speckle pattern was applied to each region of interest by coating the surface with white paint and then using black spray paint and markers to create random patterns. The black speckle sizes ranged from 0.5 to 2.5 mm (0.02 to 0.10 in.). Two cameras were used to capture 3D images from each location. Figure 3.4 illustrates typical 3D DIC setup at the box, mast-arm and baseplate connections.

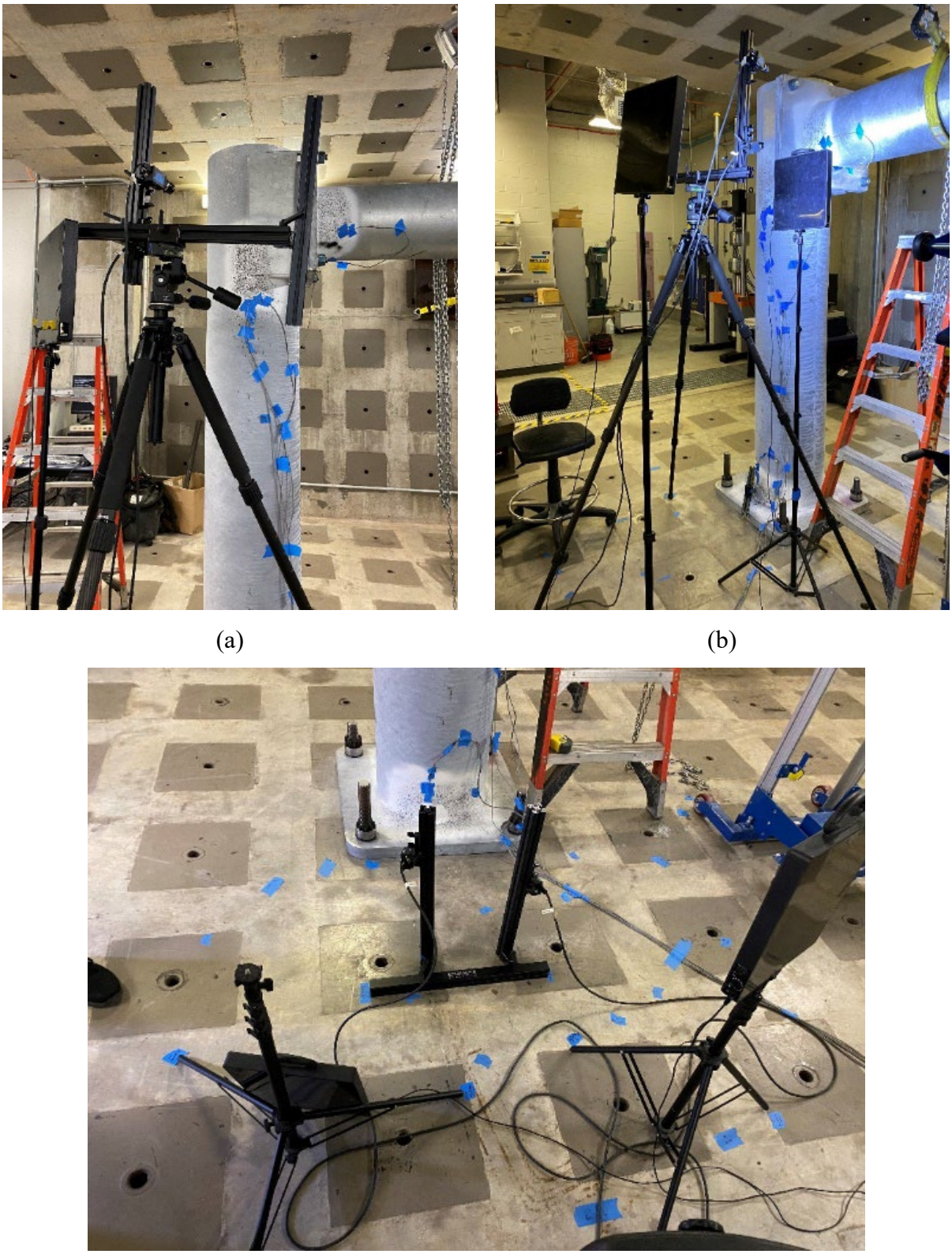

(a) (b)

(c)

Figure 3.4 3D DIC setup for the (a) box connection, (b) mast-arm, and (c) baseplate

Cameras were mounted on horizontal and vertical Unistrut bars to monitor each of the three fatigue susceptible connections. For the box and mast-arm welds, the horizontal Unistrut bar was mounted to an adjustable tripod. To ensure consistency in each set-up, which involved dismantling and reassembling the system between tests, markers were placed on the ground to indicate where the legs of the camera and light tripods should be placed. The position of the cameras on the vertical Unistrut bars, the angles of the cameras, and the angles of the vertical Unistrut bars were also measured to ensure the setups were able to be replicated.

For the box connection monitoring, the two cameras were spaced 58 cm (23 in.) apart. The arm connection crack monitoring setup only used one vertical Unistrut bar with the cameras spaced 30 cm (12 in.) apart. Monitoring of the baseplate was done by placing the horizontal Unistrut bar on the ground with the cameras spaced 30 cm (12 in.) apart. In each case, the distance from the cameras to the region of interest was approximately 58 cm (23 in.).

The cameras used in this investigation were five megapixel (2448 x 2048 pixel) PGR Grasshopper3 cameras which used a Sony IMX250 complementary metal oxide semiconductor (CMOS) sensor and a frame rate of 50 frames/second. The cameras were equipped with a 17mm Schneider Xenoplan lens with aperture of f/1.4 resulting a field of view of 240 x 200 mm (9.45 x 7.87 in.). External adjustable LED lighting panels were used to reduce shadows caused by surrounding laboratory lighting and also provide good contrast for data analysis. The sigma value in VIC-3D was used to estimate the noise level during the test. Sigma values ranging from 0.002 to 0.009 were observed, and these ranges were considered conservative for the desired area of interest within the specimen.

Images used for DIC analysis were collected at regular intervals during the application of constant amplitude fatigue. For specimens 1, 2, 4, and 6, this was every 10,000 cycles due to

fatigue initiating within 100,000 cycles for each. The other two specimens did not show signs of fatigue until more than 500,000 cycles, so DIC images were taken every 100,000 cycles to expedite testing. The stiffness of the test setup was monitored by constantly collecting load and displacement data from the actuator, and tests were stopped if a noticeable decrease in stiffness occurred.

3.2.2 DIC Post-Processing

Once the system was set up, the unloaded specimen was used to calibrate the cameras and take the reference image. After calibration, the cameras were used to take pictures by running the cyclic load at 0.1 Hz for 5 cycles. Images were captured during the cyclic loading using Correlated Solutions software VIC-3D. Strain fields were generated using images captured during the peak load condition. Prior to post-processing of the images, a subset size of 29x29 pixels and a step size of 7 pixels was defined. These values maintained a high-quality spatial resolution as well as reasonable processing time.

3.3 Cantilever Overhead Sign Structure Fatigue Crack Results

3.3.1 Crack Detection Results

For each of the six specimens, the box connection was the first of the three regions of interest to initiate a fatigue crack. At each data collection interval, the developed strain field was compared with the pre-fatigue strain field. When a significant increase in strain was identified, the specimen was inspected visually under load to determine if a fatigue crack had initiated. The initial and final strain fields for specimens 1-6 are shown in figure 3.5(a-f), respectively.

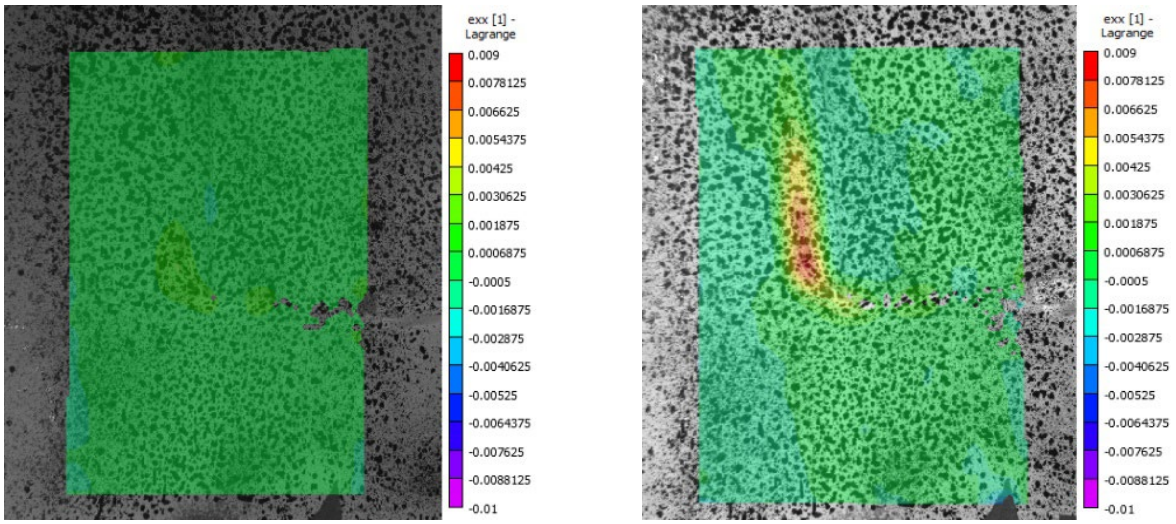
exx [1] - Lagrange
0.009
0.0078125
0.006625
0.0054375
0.00425
0.0030625
0.001875
0.0006875
-0.0005
-0.0016875
-0.002875
-0.0040625
-0.00525
-0.0064375
-0.007625
-0.0088125
-0.01
exx [1] - Lagrange
0.009
0.0078125
0.006625
0.0054375
0.00425
0.0030625
0.001875
0.0006875
-0.0005
-0.0016875
-0.002875
-0.0040625
-0.00525
-0.0064375
-0.007625
-0.0088125
-0.01

(a)

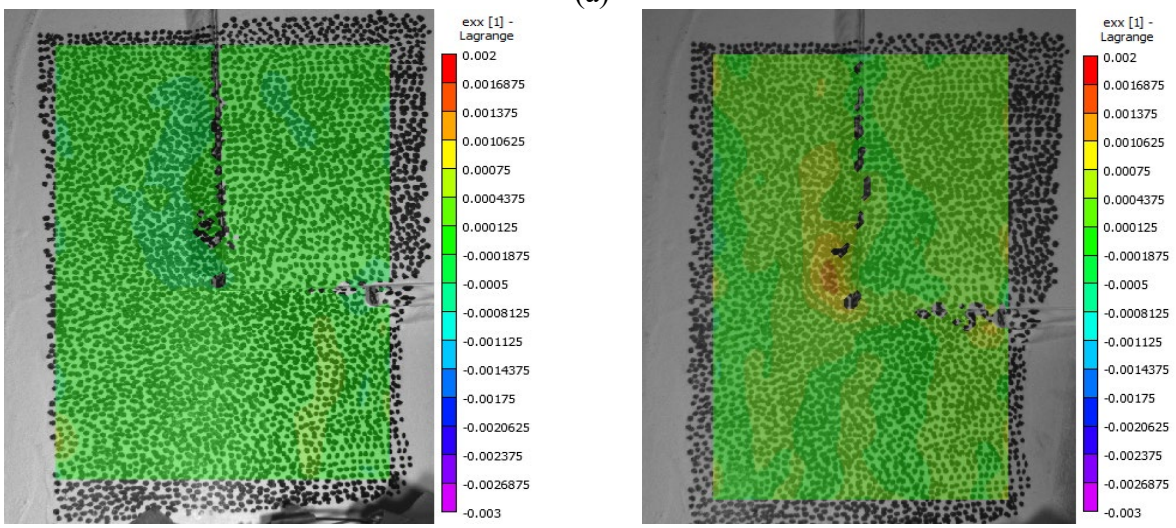
exx [1] - Lagrange
0.002
0.0016875
0.001375
0.0010625
0.00075
0.0004375
0.000125
-0.0001875
-0.0005
-0.0008125
-0.001125
-0.0014375
-0.00175
-0.0020625
-0.002375
-0.0026875
-0.003
exx [1] - Lagrange
0.002
0.0016875
0.001375
0.0010625
0.00075
0.0004375
0.000125
-0.0001875
-0.0005
-0.0008125
-0.001125
-0.0014375
-0.00175
-0.0020625
-0.002375
-0.0026875
-0.003

(b)

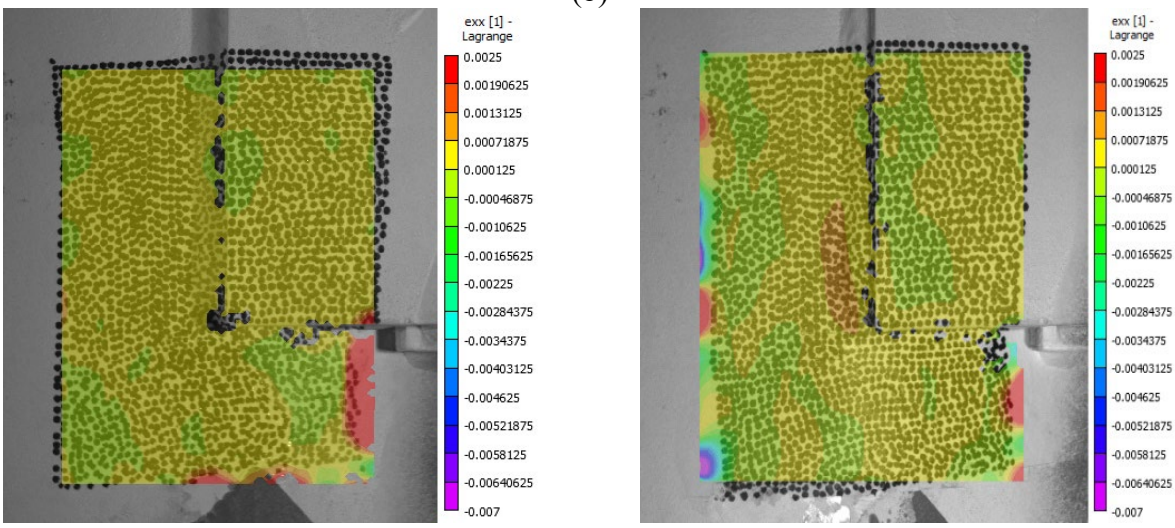
exx [1] - Lagrange
0.0025
0.00190625
0.0013125
0.00071875
0.000125
-0.00046875
-0.0010625
-0.00165625
-0.00225
-0.00284375
-0.0034375
-0.00403125
-0.004625
-0.00521875
-0.0058125
-0.00640625
-0.007
exx [1] - Lagrange
0.0025
0.00190625
0.0013125
0.00071875
0.000125
-0.00046875
-0.0010625
-0.00165625
-0.00225
-0.00284375
-0.0034375
-0.00403125
-0.004625
-0.00521875
-0.0058125
-0.00640625
-0.007

(c)

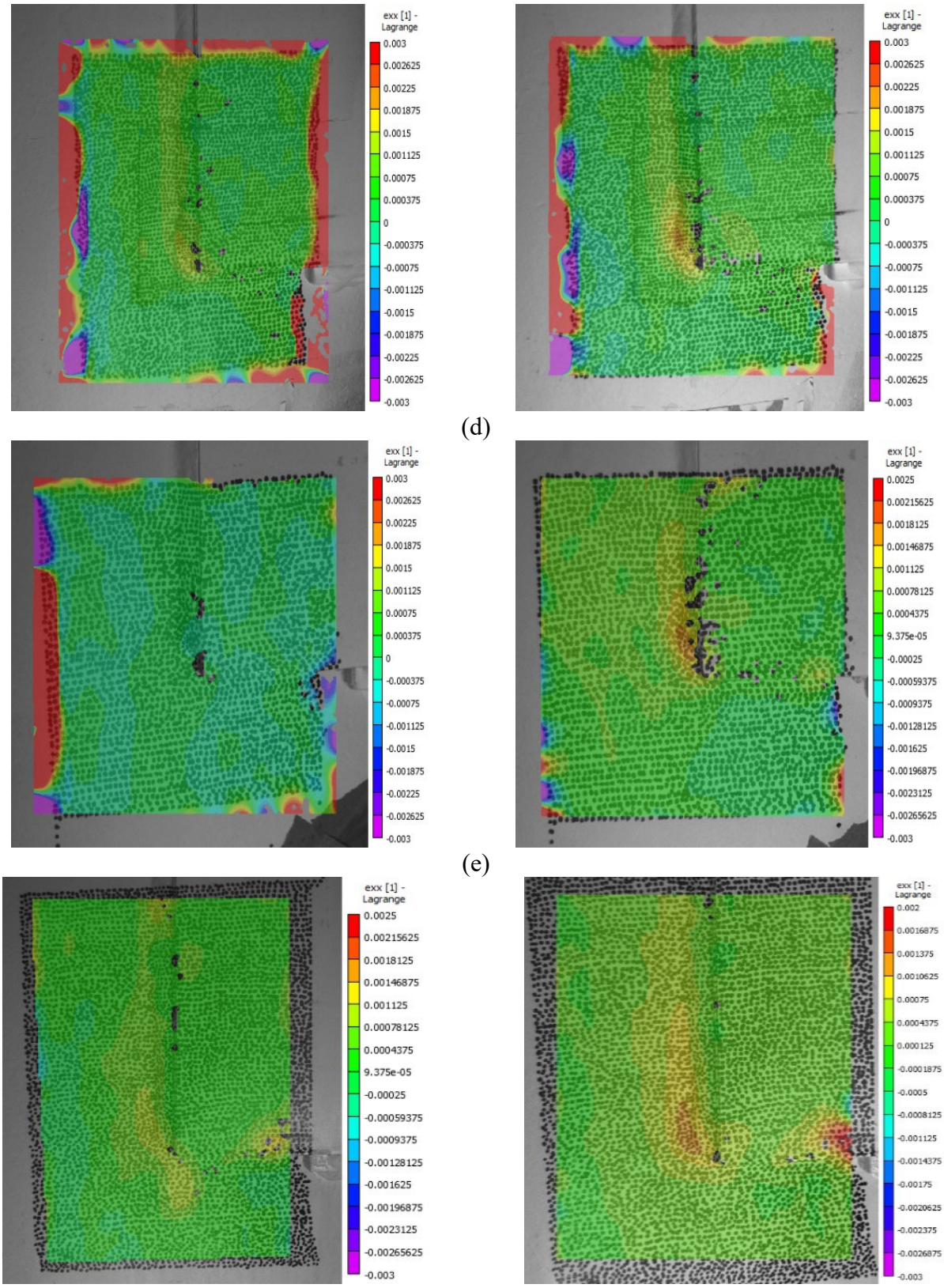

Figure 3.5 Strain fields before and after fatigue crack initiation

In each case, fatigue cracks that had yet to grow greater than 6.4 mm (0.25 in.) in length or through the thickness of the pole were confirmed by visual inspection. While this study shows that it is possible to detect fatigue crack initiation with DIC, these images illustrate that the difference in strain before and after fatigue crack initiation can be difficult to detect. Additionally, the detection of fatigue crack initiation requires frequent or continuous image collection, manual user inspection, and a high likelihood false positives under poor lighting, focus, and surface conditions. Nevertheless, this study establishes that fatigue cracks with minimal propagation are able to be detected using DIC.

Chapter 4 Application of DIC to Fracture-prone Component Evaluation

4.1 Recognition of Potential for Application to Fracture-prone Component Evaluation

4.1.1 Potential Applications

Evaluation of the cantilever overhead sign structure fatigue test revealed the potential for DIC to characterize and possibly predict cracking prior to the onset of initiation. Although the initial intent of the research was to identify and characterize cracks in the box connection that have already initiated and started to propagate, data analysis revealed that the DIC could identify the accumulation of strain prior to any visual crack formation. This led the research team to believe DIC could be useful in the evaluation of fracture-prone details, especially those that are known to fail without prior warning. Specifically, the research performed on this project identifying and characterizing fatigue cracks indicated DIC could be an excellent tool for evaluating details prone to constraint-induced fracture (CIF).

4.1.2 Brief Background on Constraint-induced Fracture

Constraint-induced fracture can be a confusing term to those unfamiliar with the definition as used in the highway bridge industry of the United States. Fracture in metallic materials and structural components is always a function of material resistance to flaws (fracture toughness), geometry, and applied stress. The combination of geometric details and applied stress produces the demand, and the level of constraint, or triaxial stress, developing at the point of interest is a major factor in fracture behavior, and all fractures require the presence of some level of constraint. However, following the fracture of the Hoan Bridge in 2000, the term constraint-induced fracture was used to describe fracture occurring from a detail when no prior fatigue cracking had occurred (Coletti et al. 2021). The details in question generally include components intersecting in three planes, as occurs when girder webs, transverse stiffeners or connection plates, and longitudinal

stiffeners or gusset plates intersect on a structure. Although there have been other examples of constraint-induced fracture in bridges (Connor et al. 2007; Ellis et al. 2013; Bowman 2002), and detailing practices have been modified to avoid some of the geometries used on these structures, this is a phenomenon that is still not well understood. Therefore, characterizing behavior at the locations of details susceptible to CIF could help in the understanding of this behavior and reduce the likelihood of catastrophic failure in the future.

4.2 Constraint-induced Fracture Testing and Results

4.2.1 Constraint-induced Fracture Specimen Design

A large-scale specimen, approximately 4.4 m (14.5 ft) in length, was designed to be able to evaluate the details known to increase the likelihood of constraint-induced fracture occurrence. The specimen was intended to replicate conditions found on highway bridges where components intersect in three planes. The specimen evaluated as part of this study is comprised of a primary plate representing a girder web, a continuous longitudinal stiffener running the majority of the length of the specimen, and a discontinuous transverse stiffener. Tensile loading is applied to the specimen through large-diameter loading pins within a self-reacting frame. The specimen is schematically represented in figure 4.1, and can be seen in figure 4.2 with half of the self-reacting frame removed from view.

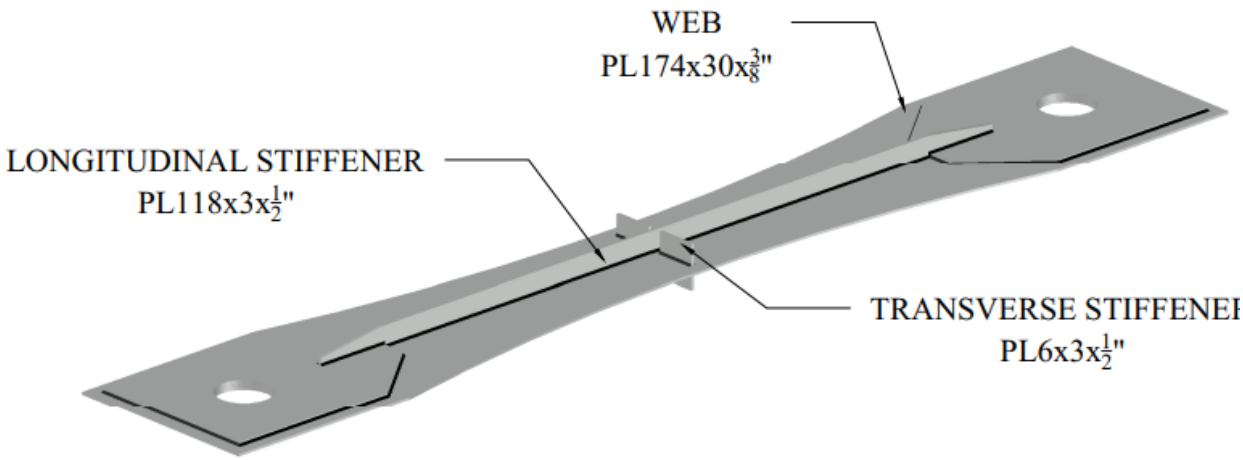

Figure 4.1. Schematic representation of discontinuous transverse stiffener CIF specimen

Figure 4.2 CIF specimen in place with partial self-reacting load frame

Loaded in tension, the primary plate has a reduced section at the point of interest measuring 457 mm x 9.5 mm (18 in. x 3/8 in.). Stiffeners in both directions are 8 mm (5/16 in.) thick and 89

mm (3.5 in.) tall. The specimen was detailed such that the distance between the longitudinal stiffener and the transverse stiffener was 20.6 mm (13/16 in.) with a gap of 12.5 mm (0.5 in.) between the longitudinal stiffener weld toe and the transverse stiffener. Details of the stiffener geometry is shown in figure 4.2.

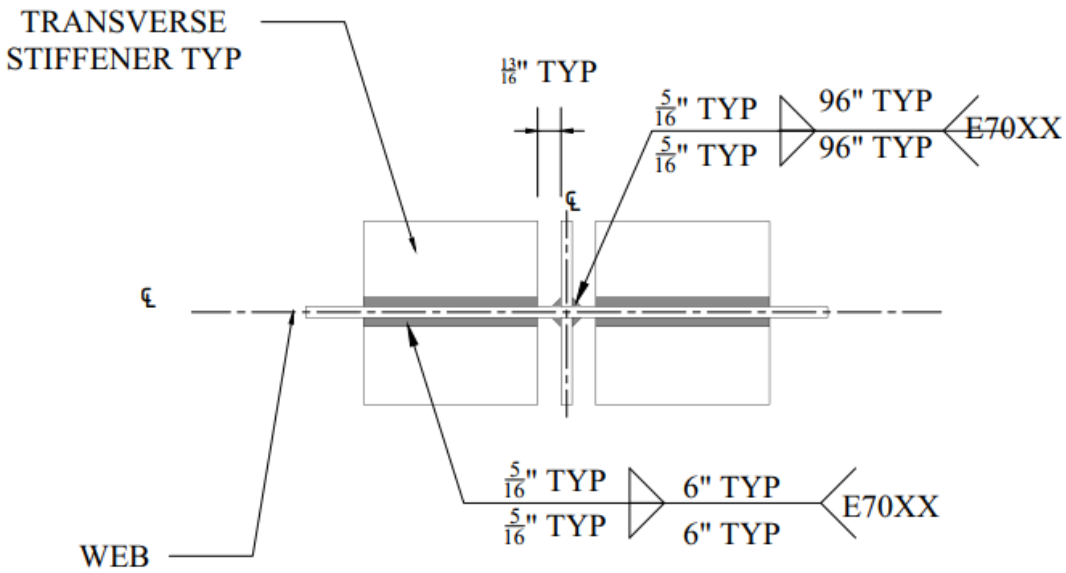

Figure 4.3 Stiffener details

4.2.2 Results of DIC during Constraint-induced Fracture Testing

A high-contrast speckle pattern was applied to parts of the web plate and stiffeners to facilitate digital image correlation data collection. However, a primary challenge in collecting DIC data on the CIF specimen was the temperature at which testing was conducted. Metallic materials become less ductile at low temperatures, making them more prone to sudden fracture. A metered liquid nitrogen system was developed to cool the specimen to -51 °C (-60 °F), matching the AASHTO Zone III minimum service temperature. This caused ice to form on the steel surfaces, obstructing the field of view for the DIC cameras. To help with this, isopropyl alcohol was sprayed onto the surface, which was then wiped with a squeegee. For safety reasons during testing, the

spray bottle and squeegee were attached to extending rods, allowing for ice removal without the need to be near the specimen. The high-contrast pattern can be seen on the web plate and stiffeners in figure 4.5.

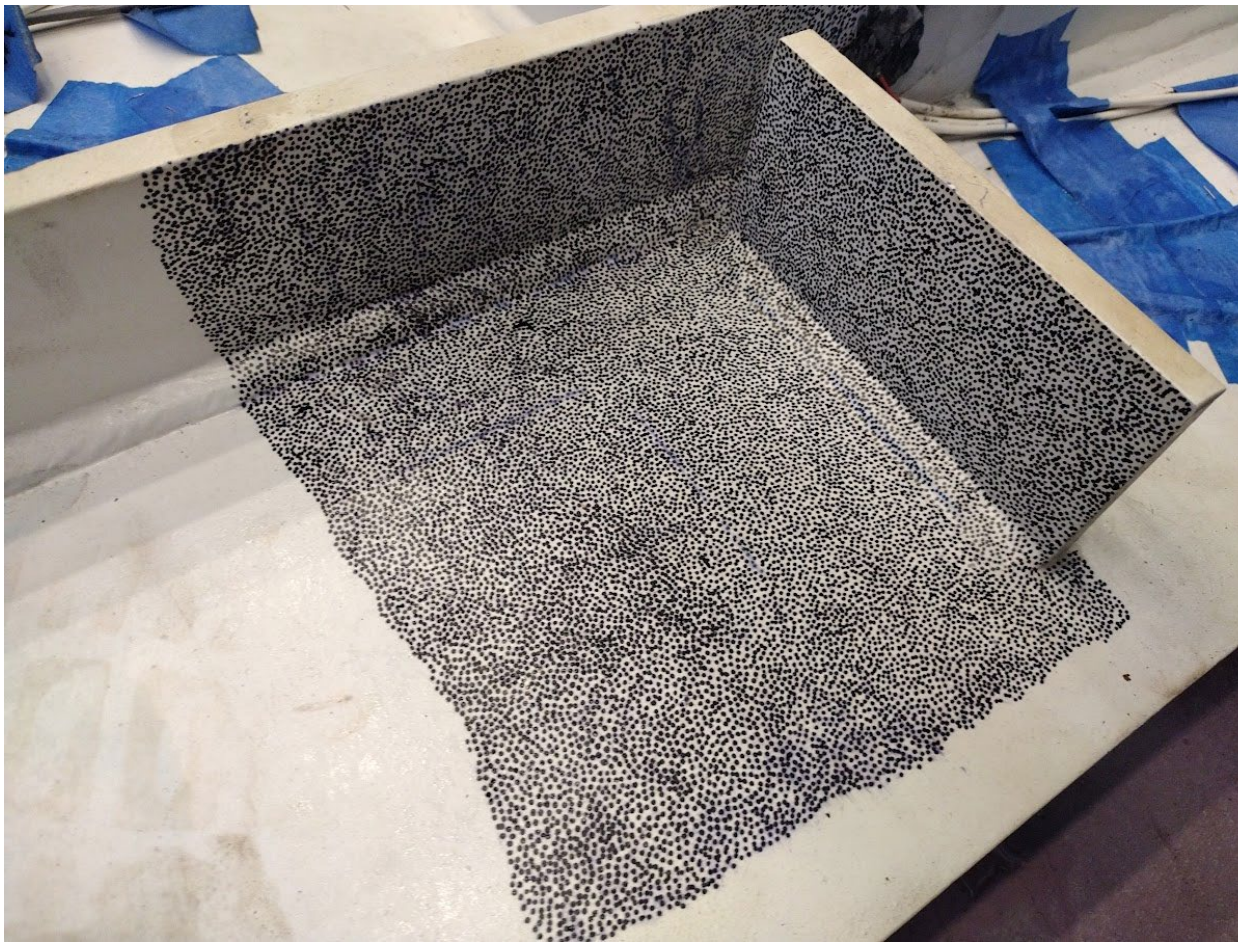

Figure 4.4 High-contrast pattern on CIF specimen prior to testing

DIC was collected through a stereo camera setup, with the cameras and lighting positioned on a frame suspended above the specimen, allowing for appropriate spacing and angles to capture data in the area of interest. The cameras and lighting can be seen above the test specimen in figure 4.5.

Figure 4.5 DIC cameras and lighting suspended above the CIF specimen

The digital image correlation equipment was calibrated prior to testing and specimen cooling. The principal strain field of the specimen at the initiation of testing is shown in figure 4.6.

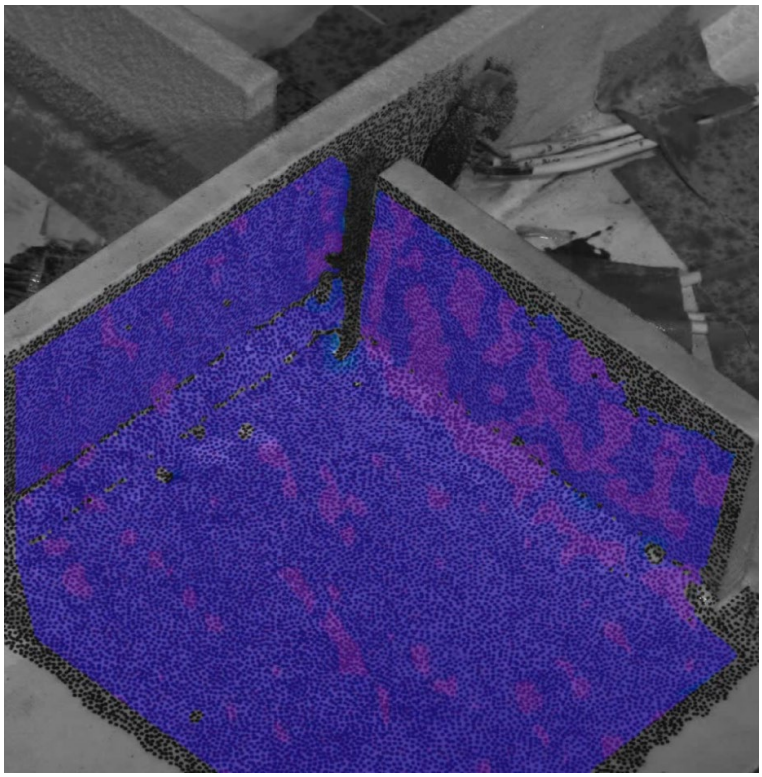

Figure 4.6 DIC calibration image of CIFC cameras and lighting suspended above the CIF specimen

The specimen was loaded in tension up to a total force of 1926 kN (433 kips), which corresponds to a nominal stress of approximately 441 MPa (64 ksi) on the primary web plate, neglecting the load-carrying capacity of the longitudinal stiffener. However, the specimen did not experience fracture at the location of interest prior to failure by bearing at the loading pins. However, DIC data was successfully captured in the region of interest at various points throughout loading. Figure 4.7 presents the visual DIC strain results at various levels of load prior to test termination. Although the specimen did not fail in fracture, and ice buildup blocked some the surface area available for data recording, the DIC was able to capture strain localization around the area of high constraint, as shown through with the warmer colors in the strain heat map. This

indicates that DIC can possibly be used to quantify behavior in this region, potentially leading to the future characterization of constraint-induced fracture behavior.

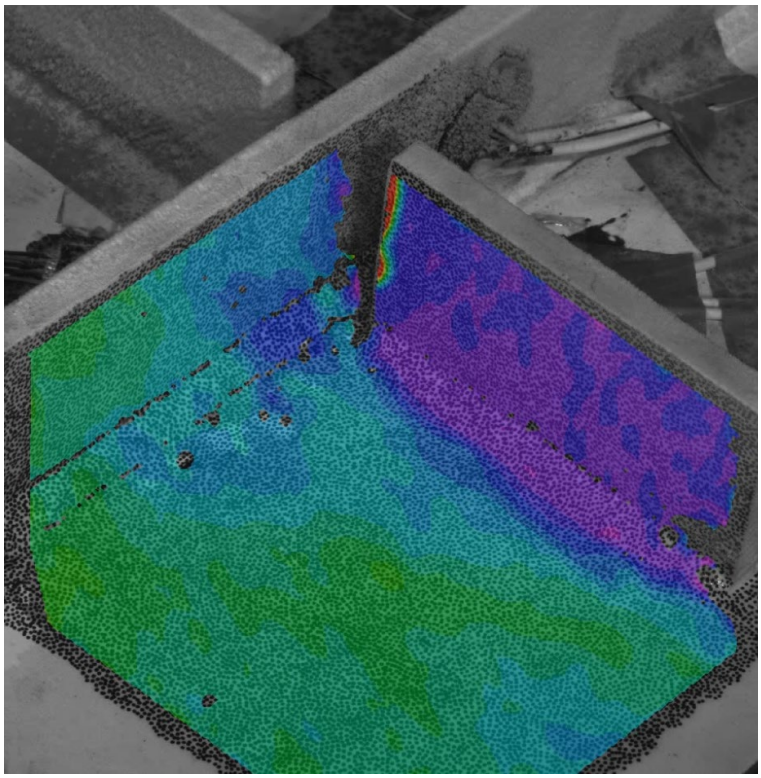

(a)

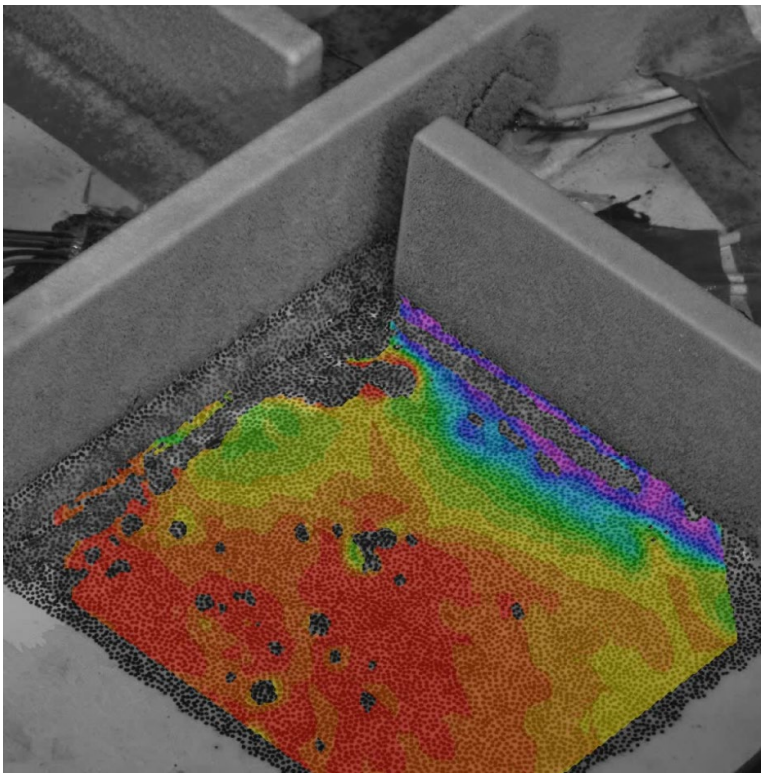

(b)

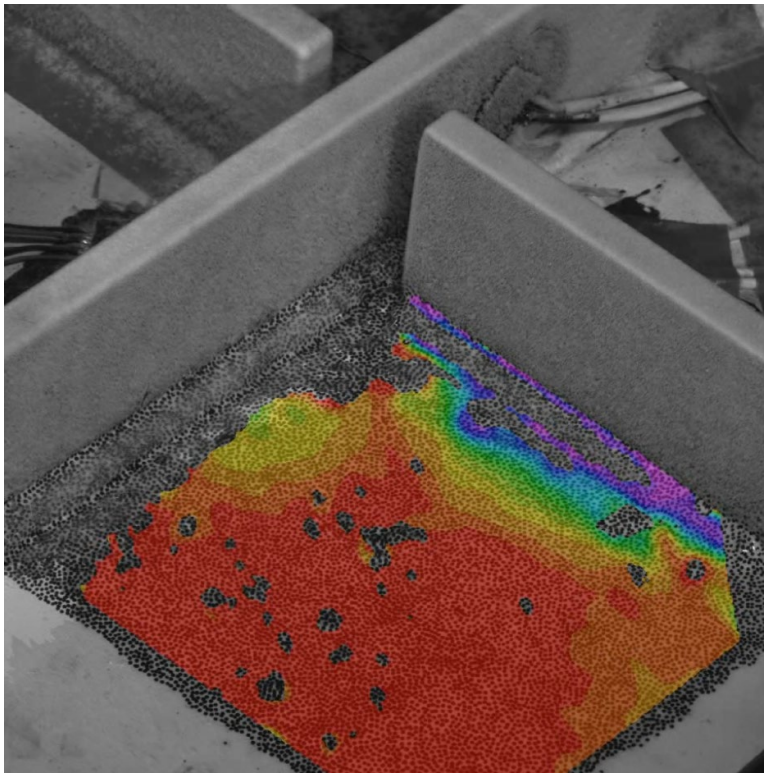

(c)

Figure 4.7 DIC principal strain fields at a) 657 kN (148 kips), b) 897 kN (202 kips), and c) 1926 kN (433 kips) of tensile force

Chapter 5 Continued Advancements Towards Automation

5.1 Digital Image Correlation Using Deep Learning Algorithms

5.1.1 Deep Learning Background

The current DIC crack detection methodology relies on conventional correlation techniques, which are time-consuming and costly, with systems typically costing over $50,000 and requiring extensive user training. The calibration process is also lengthy and varies significantly between cases. In this context, advanced technologies like deep learning and computer vision offer potential solutions to reduce both cost and time. Over the past decade, scientific fields have been transformed by data-driven methodologies, thanks to advances in computing power and storage. The availability of large datasets, such as millions of labeled images, has facilitated these developments. A key breakthrough has been the success of deep neural networks (Goodfellow et al. 2016) in various signal processing tasks, marking a paradigm shift towards data-driven approaches in scientific research.

Neural networks are structured with interconnected neurons arranged in layers within a feedforward architecture, as depicted in figure 5.1. Each layer has a specific role in data processing, culminating in the output layer's final interpretation. The input layer encodes raw data, such as images for classification tasks or image pairs for other applications. The output layer provides the final output, such as class probabilities or displacement fields. The hidden layers, situated between the input and output layers, perform complex computations. Neurons in these layers function as computational units, receiving weighted inputs and applying non-linear activation functions, such as the Rectified Linear Unit (ReLU). This non-linearity allows the network to model complex data relationships. In regression tasks, the output layer typically presents the predicted value without additional activation functions.

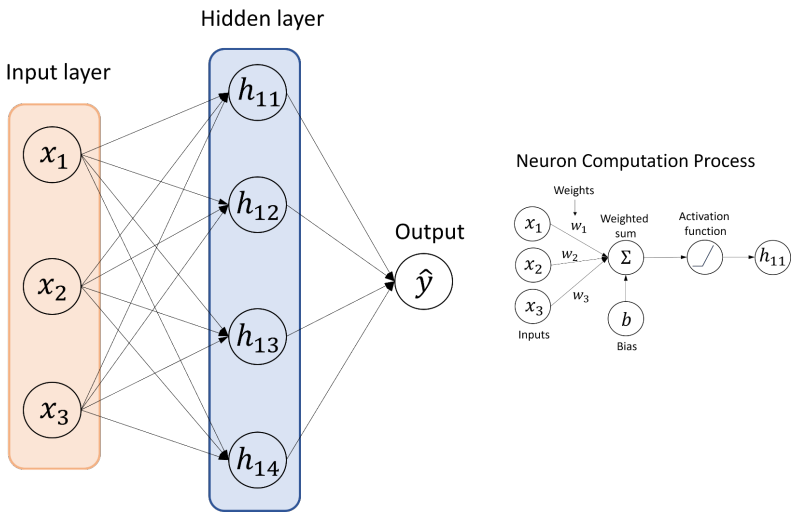

Figure 5.1 Artificial neural network structure

In computer vision, convolutional neural networks (CNNs) have emerged as a predominant subclass of deep neural networks, effectively processing visual data by adhering to essential signal processing principles. The convolution process, a fundamental component of CNNs, integrates signal filtering with feature extraction, thereby reducing trainable parameters and enhancing computational efficiency. Convolutional layers, as opposed to traditional fully connected layers, facilitate the interaction between signal patterns and learned filters, making CNNs indispensable for tasks like image classification (Krizhevsky et al., 2012), object detection (Ouyang et al., 2016), and 3D reconstruction (Chen et al., 2018). Additionally, CNNs have proven superior in optical flow estimation, surpassing traditional techniques in accuracy and speed (Hur and Roth, 2020). By employing multiple convolutional and deconvolutional layers, along with appropriate pooling and activation functions (Ilg et al., 2017), CNNs achieve sub-pixel accuracy in recovering optical flow fields, even for large displacements (Sun et al., 2018).

There are notable similarities between CNNs and DIC algorithms. Both use kernel-based methods: subset correlation in DIC resembles the convolution operation in CNNs, and peak

searching in DIC is akin to max-pooling in CNNs. However, while DIC uses a highly nonlinear correlation criterion, CNNs extract feature maps through linear kernel calculations followed by activation functions. By stacking multiple layers, CNNs can model complex nonlinear relationships between inputs and outputs, potentially surpassing traditional DIC algorithms.

Recent advancements in deep learning applications to digital image correlation have yielded promising results. Min et al. (2019) introduced a 3D convolutional neural network for extracting spatial and temporal features from image sequences in DIC, though it faced challenges due to limited training data. Boukhtache et al. (2021) adapted optical flow CNNs for DIC by utilizing synthetic speckle images, achieving sub-pixel displacement accuracy through a hybrid method combining traditional correlation and post-processing techniques. Yang et al. (2022) developed two novel CNNs, DisplacementNet and StrainNet, specifically for DIC. These networks, trained exclusively on a synthetic dataset, were designed to separately predict displacement and strain fields. This approach addresses the noise and errors commonly associated with strain field computations derived from displacement fields and preserves high spatial resolution without post-filtering.

The synthetic dataset used by Yang et al. featured a uniform distribution of grayscale intensity, represented by a bell-shaped histogram. However, in structural health monitoring, speckle patterns often exhibit clusters of bright and dark spots, resulting in a bimodal grayscale intensity histogram. This can lead to convergence issues and instability during training, as indicated by higher loss values and slower convergence rates. Furthermore, while the displacement fields in their study showed smooth transitions with localized Gaussian noise, real-world scenarios with structural cracks exhibit abrupt shifts in the displacement field at the crack location.

Our study aims to address these challenges with two primary objectives: (1) to generate a synthetic dataset of speckle pattern images featuring clusters of dark regions on a white background, representing both cracked and uncracked areas; and (2) to develop a CNN capable of predicting displacement fields with accuracy comparable to or exceeding current commercial hardware and software solutions.

5.1.2 Synthetic Data Generation Method

Training of the CNN DIC model used exclusively synthetic datasets to reduce costs and enhance data quality control. This section outlines the technique for creating realistic, high-quality datasets comprising both reference and deformed images, along with displacement field ground truths. Data was generated in two categories: 1) uncracked and 2) cracked datasets. Initially, 256 x 256 pixel speckle pattern images were generated using a speckle generator tool from Correlated Solutions. For the uncracked dataset, random motions and deformations are analytically applied to create displacement fields. In contrast, for the cracked dataset, a C(T) specimen with a horizontal crack is modeled in Abaqus to obtain displacement fields for cracked specimens. These fields serve as ground truths for the CNN, and are then used to distort the original speckle images, producing deformed counterparts. Each data sample includes the reference image, its deformed version, and the corresponding displacement field, shown in figure 5.2.

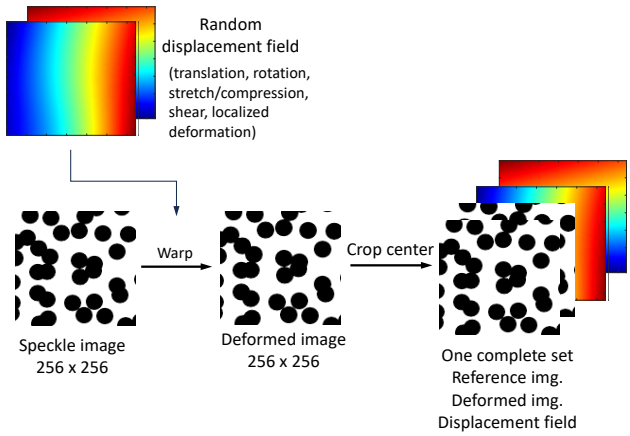

Figure 5.2 Uncracked dataset generation

For the uncracked dataset's displacement field, the methodology outlined by Yang et al. (2021) was utilized. This method combines various deformation elements, including random rigid body movements (translation and rotation), stretch/compression, shear, and localized deformations modeled using 2D Gaussian functions. The specific range of values for these deformation elements, as employed in our study, is detailed in table 5.1.

Table 5.1 Minimum and maximum values of different deformation elements

Deformation element	Minimum value	Maximum value
Translation	-6 pixels	6 pixels
Rotation	-0.005 rad	0.005 rad
Scaling	0.98	1.02
Shear	-0.0015	0.0015
2D Gaussian function	Amplitude = -1 Sigma = 30 (spread of local noise) Center = 0 (noise center location in image)	Amplitude = 1 Sigma = 80 (spread of local noise) Center = 126 (noise center location in image)

The deformed image is created by first applying predefined displacements to each pixel, resulting in deformed grid coordinates. These coordinates are then interpolated back to a uniform

grid using MATLAB's built-in function *griddata*. Following this, both the reference and deformed images are centrally cropped to a size of 128 x 128 pixels.

The methodology for creating the cracked dataset is described in the following section. In this process, a compact specimen (C(T)) was modeled using the Finite Element Analysis (FEA) software, Abaqus. Abaqus is renowned for its capability in structural analysis, particularly in simulating structural responses under various load conditions, including static, dynamic, and thermal stresses. The choice of a C(T) specimen for modeling aligns with our experimental objectives to validate our proposed model on similar physical specimens. The user can also model different specimen types in Abaqus as required.

A dataset comprising 60,000 images was created, evenly divided between cracked and uncracked regions. This dataset was then partitioned into training and testing sets, with a 90%-10% split. Both the training and testing sets maintained an equal ratio of cracked and uncracked images, ensuring balanced representation in each set.

5.1.3 Deep Learning DIC Architecture

An encoder-decoder based CNN with basic Unet architecture was trained for this project. The model architecture is presented in figure 5.3. The network consists of encoder and decoder parts. The encoder path, which downsamples the data, consists of a series of convolutional blocks, each followed by maxpooling. The purpose of the encoder is to extract features from the input image while reducing the spatial dimensions. The typical encoder block consists of a 3x3 convolution layer, padding of size 1, ReLu activation, followed by a maxpooling layer. The first block has a convolution layer with 64 channels; the second encoder block consists of convolution layers with 128 channels; the third block has 256 channels; and the fourth layer has 512 channels. The last encoder block does not have a maxpooling layer.

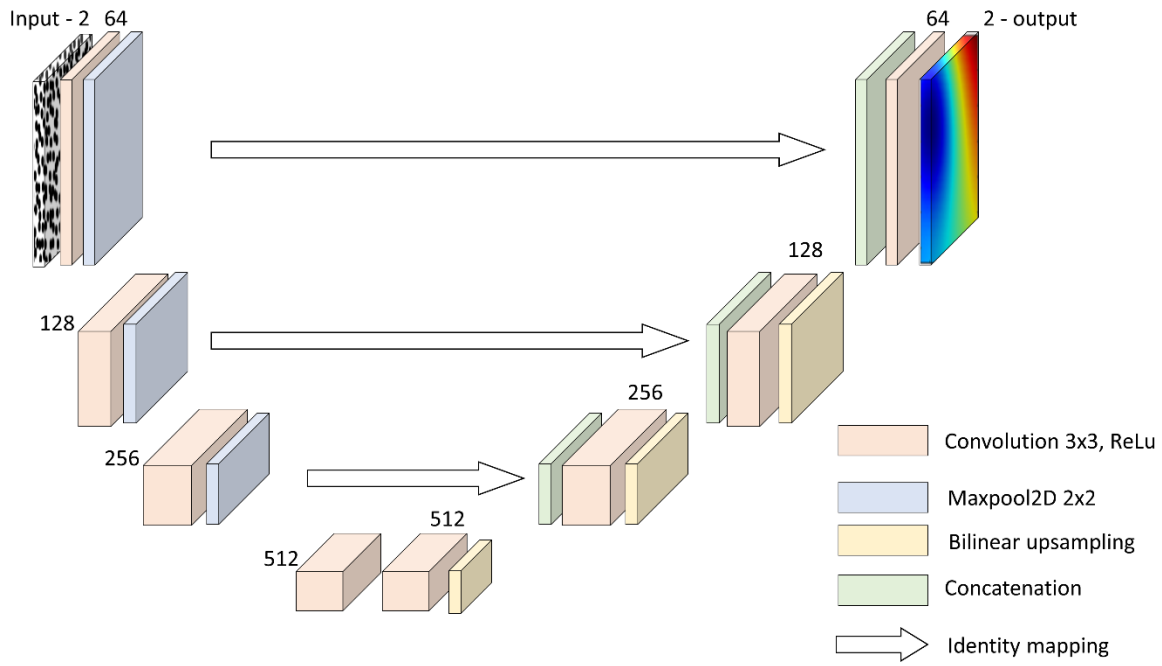

Figure 5.3 Unet architecture

The decoder path, which upsamples the encoded data, consists of a series of upsample blocks followed by concatenation with the corresponding encoder block and a convolutional block. The purpose of the decoder is to reconstruct the spatial dimensions and refine the features learned by the encoder. The first decoder block with 512 output channels followed by bilinear upsampling is mapped to the last encoder block. The second decoder block has 256 output channels; the third, 128 channels; and the fourth, 64 channels. An output convolution layer with kernel size 1 and 2 output channels was applied to the last decoder block.

5.1.4 Deep Learning DIC Training and Results

The training process was set to run for 500 epochs, and the Adam optimizer was used with a learning rate of 0.001. A mean squared error loss (MSE) function was employed for training, as it is generally considered suitable for regression tasks. The training loss function is presented in figure 5.4. The zoomed in view of training loss is presented in figure 5.4b. The loss function is

very high initially with MSE of 1.58 pixels and rapidly decreases to 0.0058 pixels in 10 epochs only. Then the MSE loss reduction is gradual and reduces to 0.000368 pixels at the end of the training process suggesting the model is improving and learning from the training data as expected.

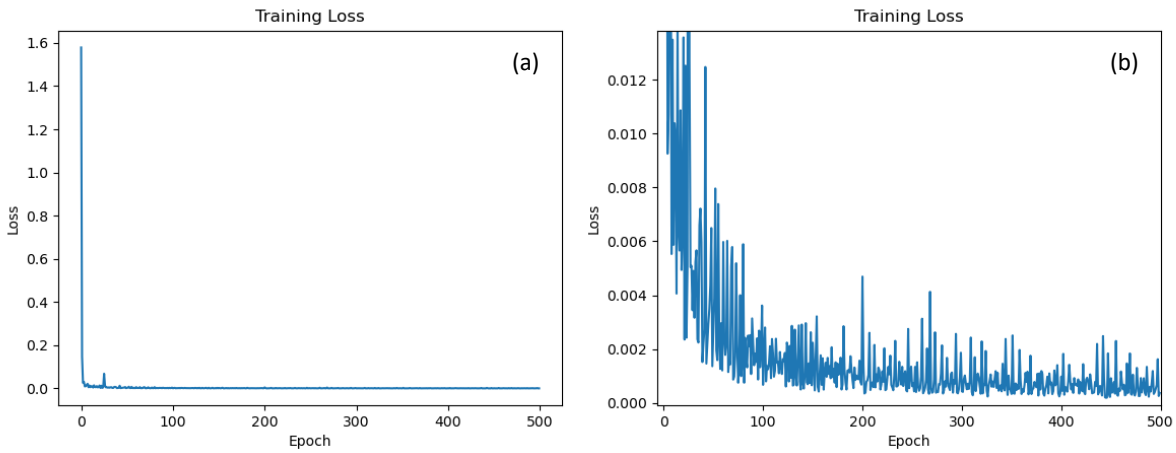

Figure 5.4 Training loss for the proposed model

Upon completion of the training phase, the model underwent evaluation using the designated testing dataset. The performance and accuracy of the model's inferences were quantified using several statistical metrics, including Mean Absolute Error (MAE), Mean Squared Error (MSE), Root Mean Squared Error (RMSE), and R-squared (R^2). The outcomes of these evaluations are comprehensively detailed and presented in table 5.2, collectively indicate a high level of predictive accuracy and reliability. The MAE of 0.0227 reflects the model's precision in predicting displacement fields, with the average predictions closely aligning with the actual values. This accuracy is further supported by the MSE of 0.00113, indicating minimal variance in the model's predictions from the true values, and a low likelihood of large errors. The RMSE at 0.0336 reinforces this observation, suggesting a consistent accuracy across the model's predictions, considering the distribution of errors. Moreover, the high R^2 value of 0.9985 demonstrates the

model's effectiveness in explaining nearly all the variability of the response data around its mean. This ensemble of metrics underlines the model's robustness in accurately predicting the displacement fields in the testing dataset with minimal error.

Table 5.2 Model Performance Metrics

Measure of Accuracy	**Model Accuracy**
Mean Absolute Error (MAE)	0.0227
Mean Squared Error (MSE)	0.00113
Root Mean Squared Error (RMSE)	0.0336
R-squared (R^2)	0.9985

Two sample inferences from the proposed model are presented in figure 5.5. The first column shows the ground truths. Adjacent to them are model's predicted displacement fields which aim to replicate the ground truth patterns. The third column in each row highlights the difference between the predicted and ground truth fields, with color intensities representing the magnitude of the discrepancies in terms of pixels. In the top row, the sample features a cracked region, with a sharp discontinuity in the vertical displacement field. Here, model's predictions closely align with the ground truths, evidenced by the near-zero values across the error map. This indicates a high level of accuracy in the network's inference, even in the presence of a structural anomaly such as a crack. The bottom row presents a sample from an uncracked region, characterized by a broader range of displacement values and a more complex field with nonlinear gradients. Despite these complexities, the proposed model successfully captures the nonlinear relationship in the displacement field between the image pairs, as reflected by the precise predictions in the corresponding error map. This example underscores the network's proficiency in handling varying patterns of displacement without the presence of discontinuities.

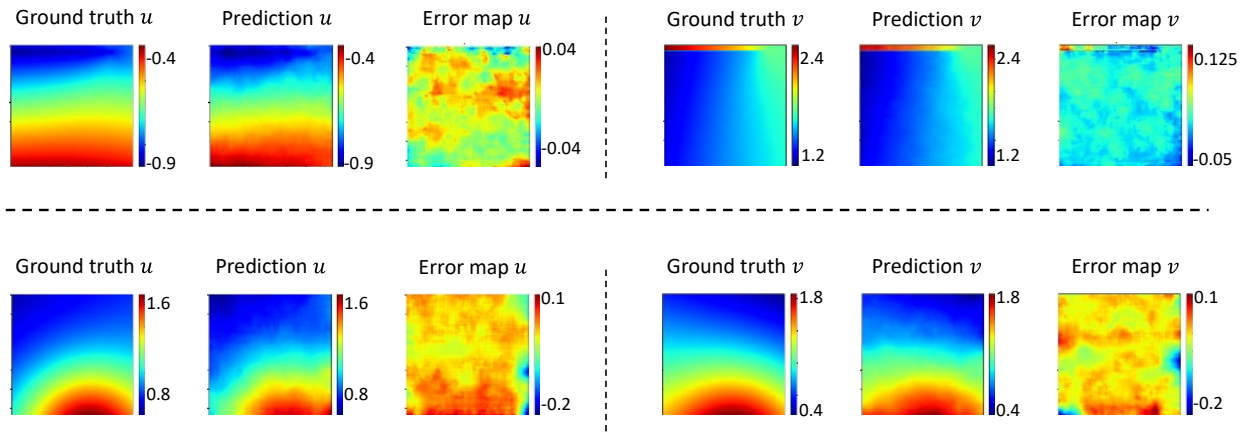

Figure 5.5 Two sample predictions from the test dataset

Chapter 6 Conclusions and Future Work

6.1 Conclusions

The COSS fatigue testing confirmed that 3D DIC strain fields are capable of detecting fatigue cracks at or near the point of initiation with lengths less than 6.4 mm (0.25 in.). This minimum threshold was established under ideal lighting, focus, and surface conditions, and therefore may be difficult to achieve in the field. Monitoring for fatigue crack initiation also requires frequent evaluation by the user and is unlikely to be feasible for structures in the field. Despite these limitations, this study indicates that fatigue cracks will be able to be detected using DIC well before they reach critical lengths.

DIC data was also collected on a laboratory test of a fracture-prone detail. The full-scale constraint-induced fracture specimen test did not result in a fracture, but the strain characterization in the region of high constraint is indicative that DIC is capable of characterizing behavior in this region. Significant additional work is needed to fully characterize CIF behavior, but DIC will be helpful in those efforts.

An innovative deep learning-based DIC approach has been developed for the end-to-end quantification of displacement fields, specifically tailored for fatigue crack inspection. In an effort to reduce training expenses, a novel methodology was devised for the generation of a realistic and exhaustive training dataset that encompasses reference and deformed speckle images, alongside the ground truths of the predefined displacement fields. The model's proficiency, as evidenced by its performance on this synthetic dataset, underscores the potential of deep learning to decipher complex correlations between paired images.

6.2 Future Work

Future work involves experimental validation of the proposed approach to estimate displacement field in a C(T) specimen with fatigue crack subjected to uniaxial loading. The process of Deep DIC during tensile tests is depicted in figure 6.1. Initially, a series of images of the specimen are captured throughout the application of the load. The first image is used to select the Region of Interest (ROI) for displacement field analysis. If the images have a higher resolution than the CNN model's input size, patches corresponding to the model's input dimensions are extracted from the ROI to maintain a high spatial resolution in the displacement field prediction. These patches are then fed into the CNN for displacement field estimation. After processing all patches, the predicted displacement fields are assembled and mapped onto the specimen's image.

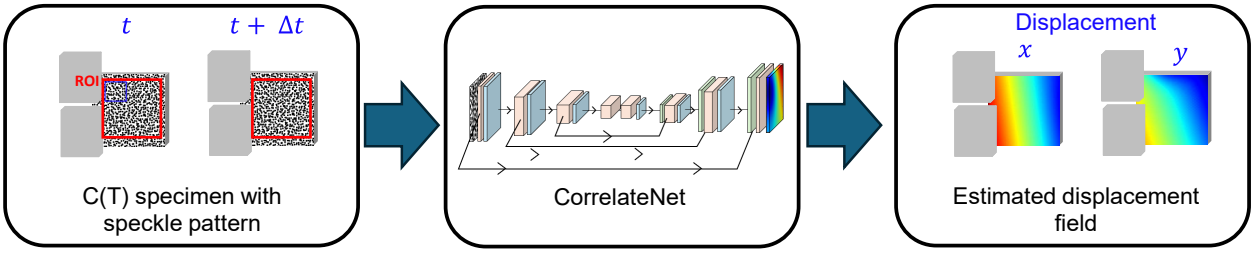

Figure 6.1 Overall methodology of experimental validation

The compact specimens were prepared, each painted with a high-contrast speckle pattern, and captured laboratory images of these specimens under load. Figure 6.2 illustrates the C(T) specimen loaded in a uniaxial frame, along with extracted patches of the speckle pattern on the specimen. As evident from the figure, the speckle pattern exhibits irregular shapes, contrasting with the regular patterns in our synthetic dataset. To align more closely with the actual images, the dataset generation methodology is being revised and new algorithms are being developed. Once the synthetic dataset more accurately mirrors the real images, the CorrelateNet model will be

retrained on the updated dataset. Subsequently, the performance of the model will be evaluated using images of the actual C(T) specimen and compared against the output from commercial DIC software.

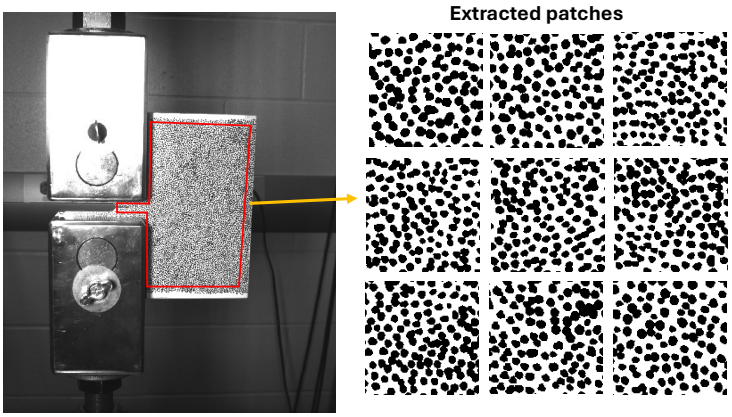

Figure 6.2 Laboratory images of speckle pattern patches from C(T) specimen

References

Abdel-Qader, I., Abudayyeh, O., & Kelly, M. E. (2003). Analysis of edge-detection techniques for crack identification in bridges. *J. Comp. Civil Eng.*, 17(4), 255-263.

Alipour, M., Washlesky, S. J., & Harris, D. K. (2019). Field Deployment and Laboratory Evaluation of 2D Digital Image Correlation for Deflection Sensing in Complex Environments. *J. Bridge Eng.*, 24(4), 04019010. doi: 10.1061/(ASCE)BE.1943-5592.0001363.

Al-Salih, H., Juno, M., Collins, W., Bennett, C., & Li, J. (2021). Application of a digital image correlation bridge inspection methodology on geometrically complex bifurcated distortion-induced fatigue cracking. *Fatigue Fract. Eng. Mater. Struct.*, 1-16. doi: 10.1111/ffe.13453.

Al-Salih, H., Juno, M., Collins, W., Bennett, C., Li, J., & Sutley, E. (2019). Evaluation of a Digital Image Correlation Bridge Inspection Methodology on Complex Distortion-Induced Fatigue Cracking. *In Procedia Structural Integrity*, 17, 682-689.

American Society of Civil Engineers (ASCE). (2021). 2021 Infrastructure Report Card – Bridges, https://www.infrastructurereportcard.org/wp-content/uploads/2020/12/Bridges-2021.pdf.

Blaber, J., Adair, B., and Antoniou, A. (2015). Ncorr: Open-Source 2D Digital Image Correlation Matlab Software. *Exp. Mech.*, 55, 1105-1122. doi: 10.1007/s11340-015-0009-1.

Boukhtache, S., Abdelouahab, K., Berry, F., Blaysat, B., Grediac, M., & Sur, F. (2021). When deep learning meets digital image correlation. *Opt. Lasers Eng.*, 136. doi: 10.1016/j.optlaseng.2020.106308.

Bowman, M. (2002). Fatigue Behavior of Beam Diaphragm Connections with Intermittent Fillet Welds, Part II: Brittle Fracture Examination of the I-64 Blue River Bridge. Final Report FHWA/IN/JTRP-2001/10-II. FHWA.

Campbell, L. E., Connor, R. J., Whitehead, J. M., & Washer, G. A. (2020). Benchmark for Evaluating Performance in Visual Inspection of Fatigue Cracking in Steel Bridges. *J. Bridge Eng.*, 25(1). doi: 10.1061/(ASCE)BE.1943-5592.0001507.

Carroll, J., Abuzaid, W., Lambros, J., & Sehitoglu, H. (2012). High resolution digital image correlation measurements of strain accumulation in fatigue crack growth. *Int. J. Fatigue*. doi: 10.1016/j.ijfatigue.2012.06.010.

Carroll, J., Efstathiou, C., Lambros, J., Sehitoglu, H., Hauber, B., Spottswood, S. & Chona, R. (2009). Investigation of fatigue crack closure using multiscale image correlation experiments. *Eng. Fract. Mech.*, 76(15): 2384.

Cha, Y. J., Choi, W., & Büyüköztürk, O. (2017). Deep Learning-Based Crack Damage Detection Using Convolutional Neural Networks. *Comp.-Aided Civil Infrastruct. Eng.*, 32(5), 361-378.

Chen, F., Chen, X., Xie, X., Feng, X., & Yang, L. (2013). Full-field 3D measurement using multi-camera digital image correlation system. *Opt. Lasers Eng.*, 51(9), 1044-1052. doi: 10.1016/j.optlaseng.2013.03.001.

Chen, L., Zhang, D., Zhou, Y., Liu, C., & Che, S. (2018). Design of a high-precision and non-contact dynamic angular displacement measurement with dual-Laser Doppler Vibrometers. Scientific Reports, 8(1), 9094.

Cigada, A., Mazzoleni, P., & Zappa, E. (2014). Vibration monitoring of multiple bridge points by means of a unique vision-based measuring system. *Exp. Mech.*, 54(2), 255-271.

Coletti, D., Chavel, B., & Ream, A. (2021). Evaluation of Steel Bridge Details for Risk of Constraint-Induced Fracture. FHWA.

Connor, R. J., & Fisher, J. W. (2006). Identifying effective and ineffective retrofits for distortion fatigue cracking in steel bridges using field instrumentation. *J. Bridge Eng.*, 11(6), 745-752.

Connnor, R. J., Kaufmann, E., Fisher, J., & Wright, W. (2007). Prevention and mitigation strategies to address recent brittle fractures in steel bridges. *J. Bridge Eng.*, 12(2), 164-173.

Dellenbaugh, L., Kong, X., Al-Salih, H., Collins, W., Bennett, C., Li, J., & Sutley, E. (2020). "Development of Distortion-Induced Fatigue Crack Characterization Methodology using Digital Image Correlation." *J. Bridge Eng.*, 25(9). doi: 10.1061(ASCE)BE.1943-5592.0001598.

Dhanasekar, M., Prasad, P., Dorji, J., & Zahra, T. (2018). Serviceability Assessment of Masonry Arch Bridges Using Digital Image Correlation. *J. Bridge Eng.*, 24(2), 04018120. doi: 10.1061/(ASCE)BE.1943-5592.0001341.

Dosovitskiy, A., Fischer, P., Ilg, E., Hausser, P., Hazirbas, C., Golkov, V., van der Smagt, P., Cremers, D., & Brox, T. (2015). FlowNet: Learning optical flow with convolutional networks. In *Proceedings of the IEEE international conference on computer vision* (2758-2766).

Ellis, R., Connor, R., Medhekar, M., MacLaggan, D., & Bialowas, M. (2013). Investigation and Repair of the Diefenbaker Bridge Fracture. 2013 Conference of the Transportation Association of Canada, Winnipeg, Canada.

Federal Highway Administration (FHWA). (2004). *National bridge inspection standards*, Federal Register, 69 (239).

Fisher, J. W. (1984). *Fatigue and fracture in steel bridges. Case studies*. J. Wiley and Sons, Limited; Sussex, England.

Goodfellow, I., Bengio, Y., & Courville, A. (2016). Deep learning. MIT press.

Hamam, R., Hild, F., & Roux, S. (2007). Stress Intensity Factor Gauging by Digital Image Correlation: Application in Cyclic Fatigue. *Strain*, 43(3), 181-192. doi: 10.1111/j.1475-1305.2007.00345.x.

Helfrick, M. N., Niezrecki, C., Avitabile, P., & Schmidt, T. (2011). 3D digital image correlation methods for full-field vibration measurement. *Mech. Systems and Signal Processing*, 25(3), 917-927. doi: 10.1016/j.ymssp.2010.08.013.

Helm, J. D. (1996). Improved three-dimensional image correlation for surface displacement measurement. *Opt. Eng.*, 35(7), 1911. doi: 10.1117/1.600624.

Hur, J., & Roth, S. (2020). Optical flow estimation in the deep learning age. Modelling Human Motion: From Human Perception to Robot Design, 119-140. doi: 10.48550/arXiv.2004.02853

Hutt, T., & Cawley, P. (2009). Feasibility of digital image correlation for detection of cracks at fastener holes. *NDT & E International*. 42, 141-149. doi: 10.1016/j.ndteint.2008.10.008.

Ilg, E., Mayer, N., Saikia, T., Keuper, M., Dosovitskiy, A., & Brox, T. (2017). Flownet 2.0: Evolution of optical flow estimation with deep networks. In Proceedings of the IEEE conference on computer vision and pattern recognition (pp. 2462-2470).

International Digital Image Correlation Society, Jones, E. M. C., & Iadicola, M. A. (Eds.). (2018). A Good Practice Guide for Digital Image Correlation. doi: 10.32720/idics/gpg.ed1.

Juno, M., Al-Salih, H., Collins, W., Bennett, C., Li, J., & Sutley, E. (2020). Investigating lighting and focus limitations of digital image correlation as a bridge inspection tool. *Structures Congress 2020*, 341-348. doi: 10.1061/9780784482896.032.

Kong, X., & Li, J. (2018). Vision-based Fatigue Crack Detection of Steel Structures Using Video Feature Tracking. *Comp.-Aided Civil Infrastruct. Eng.*, 33(9), 783-799.

Krizhevsky, A., Sutskever, I., & Hinton, G. E. (2012). Imagenet classification with deep convolutional neural networks. Advances in neural information processing systems, 25.

Küntz, M., Jolin, M., Bastien, J., Perez, F., & Hild, F. (2006). Digital image correlation analysis of crack behavior in a reinforced concrete beam during a load test. *Canadian J. Civil Eng.*, 33(11), 1418-1425. doi: 10.1139/l06-106.

Lee, J. J., & Shinozuka, M. (2006). A vision-based system for remote sensing of bridge displacement. *NDT & E International*, 39(5), 425-431. doi: 10.1016/j.ndteint.2005.12.003.

Liu, H. In: Bennett, C. R., Li, J., Matamoros, A., Rolfe, S., & Ward, D., (Eds). (2015). A Finite-Element-Based Approach to Modeling Cracking & Repairs for Distortion-Induced Fatigue in Steel Bridges. *ProQuest Dissertations Publishing.*

Lorenzino, P., Beretta, G., & Navarro, A. (2014). Application of Digital Image Correlation (DIC) in resonance machines for measuring fatigue crack growth. *Frattura ed Integrità Strutturale*. 30, 369-374. doi: 10.3221/IGF-ESIS.30.44.

Min, H. G., On, H. I., Kang, D. J., & Park, J. H. (2019). Strain measurement during tensile testing using deep learning-based digital image correlation. *Measurement Science and Tech.*, 31(1). doi: 10.1088/1361-6501/ab29d5.

Nowell, D., Paynter, R. J., & Matos, P. F. (2010). Optical methods for measurement of fatigue crack closure: Moiré interferometry and digital image correlation. *Fatigue & Fracture of Engineering Materials & Structures*, 33(12), 778-790. doi: 10.1111/j.1460-2695.2010.01447.x.

Pan, B., Tian, L., & Song, X. (2016). Real-time, non-contact and targetless measurement of vertical deflection of bridges using off-axis digital image correlation. *NDT & E International*, 79, 73-80. doi: 10.1016/j.ndteint.2015.12.006.

Reagan, D., Sabato, A., & Niezrecki, C. (2018). Feasibility of using digital image correlation for unmanned aerial vehicle structural health monitoring of bridges. *Structural Health Monitoring*, *17*(5), 1056–1072. doi: 10.1177/1475921717735326.

Ribeiro, D., Calçada, R., Ferreira, J., & Martins, T. (2014). Non-contact measurement of the dynamic displacement of railway bridges using an advanced video-based system. *Engineering Structures*, 75, 164-180. doi: 10.1016/j.engstruct.2014.04.051.

Rupil, J., Roux, S., Hild, F., & Vincent, L. (2011). Fatigue microcrack detection with digital image correlation. *The Journal of Strain Analysis for Engineering Design*. 46. 492-509. doi: 10.1177/0309324711402764.

Sun, D., Yang, X., Liu, M. Y., & Kautz, J. (2018). Pwc-net: Cnns for optical flow using pyramid, warping, and cost volume. In Proceedings of the IEEE conference on computer vision and pattern recognition (pp. 8934-8943).

Sutton, M. A., Yan, J. H., Deng, X., Cheng, C. S., & Zavattieri, P. (2007). Three-dimensional digital image correlation to quantify deformation and crack-opening displacement in ductile aluminum under mixed-mode I/III loading. *Optical Engineering*, 46(5), 051003. doi: 10.1117/1.2741279.

Turner, D. Z. (2015.) Digital Image Correlation Engine (DICe) Reference Manual. Sandia Nat. Lab.: Livermore, California, USA. http://dicengine.github.io/dice/.

Vanlanduit, S., Vanherzeele, R., Longo, R., & Guillaume, P. (2008). Investigation of fatigue cracks using digital image correlation. *Emerging Technologies in NDT*. 4, 53-58.

Vanlanduit, S., Vanherzeele, R., Longo, R., & Guillaume, P. (2009). A digital image correlation method for fatigue test experiments. *Optics and Lasers in Engineering*, 47(3-4), 371-378. doi: 10.1016/j.optlasend.2008.03.016.

Whitehead, J. (2015). "Probability of detection study for visual inspection of steel bridges." Master's Thesis, Purdue University, West Lafayette, IN.

Yamaguchi, T., & Hashimoto, S. (2010). Fast crack detection method for large-size concrete surface images using percolation-based image processing. *Machine Vision and Applications*, 21(5), 797-809.

Yang, J., & Bhattacharya, K. (2020). Augmented Lagrangian Digital Image Correlation (AL-DIC) Code Manual. CaltechDATA. doi: 10.22002/D1.1443.

Yang, R., Li, Y., Zeng, D., & Guo, P. (2022). Deep DIC: Deep learning-based digital image correlation for end-to-end displacement and strain measurement. *J. Mat. Process. Tech.*, 302. doi: 10.1016/j.jmatprotec.2021.117474.

Yeum, C. M., & Dyke, S. J. (2015). Vision-based automated crack detection for bridge inspection. *Comp.-Aided Civil Infrastruct. Eng.*, 30(10), 759-770.

Yu, S. N., Jang, J. H., & Han, C. S. (2007). Auto inspection system using a mobile robot for detecting concrete cracks in a tunnel. *Automation in Construction*, 16(3), 255-261.

Yuan, Y., Huang, J., Peng, X., Xiong, C., Fang, J., & Yuan, F. (2014). Accurate displacement measurement via a self-adaptive digital image correlation method based on a weighted ZNSSD criterion. *Opt. Lasers Eng.*, 52, 75-85. doi: 10.1016/j.optlaseng.2013.07.016.

Zhang, R., & He, L. (2012). Measurement of mixed-mode stress intensity factors using digital image correlation method. *Opt. Lasers Eng.*, 50(7), 1001-1007. doi: 10.1016/j.optlaseng.2012.01.009.

Zhao Z., & Haldar, A. (1996). Bridge fatigue damage evaluation and updating using non-destructive inspections. *Eng. Fracture Mech*., 53(5), 775-88.

Zhao, Y., & Roddis, W. M. K. (2004). Fatigue Prone Steel Bridge Details: Investigation and Recommended Repairs, *K-TRAN: KU-99-2, Final Report.* Kansas Department of Transportation, Topeka, KS.

Zou, Q., Cao, Y., Li, Q., Mao, Q., & Wang, S. (2012). CrackTree: Automatic crack detection from pavement images. *Pattern Recognition Letters*, 33(3), 227-238.

Appendix A Previous Work

Tables A.1 through A.3 show the light and focus testing conditions for camera to specimen distances of 648, 432, and 216 mm (25.5, 17.0, and 8.5 in.), respectively.

Table A.1 Light and focus conditions for 648 mm (25.5 in.) distance

Condition	**Focus**	**Focal Length, mm (in.)**	**Lighting**	**Light Range, lumens**
1	Ideal	648 (25.5)	High	5850 – 6600
2	Ideal	648 (25.5)	Medium	4450 – 5000
3	Ideal	648 (25.5)	Low	2000 – 2350
4	Fair	615 (24.2)	High	5850 – 6600
5	Fair	615 (24.2)	Medium	4450 – 5000
6	Poor	583 (22.9)	High	5850 – 6600

Table A.2 Light and focus conditions for 432 mm (17.0 in.) distance

Condition	**Focus**	**Focal Length, mm (in.)**	**Lighting**	**Light Range, lumens**
1	Ideal	432 (17.0)	High	5850 – 6600
2	Ideal	432 (17.0)	Medium	4450 – 5000
3	Ideal	432 (17.0)	Low	2000 – 2350
4	Fair	410 (16.2)	High	5850 – 6600
5	Fair	410 (16.2)	Medium	4450 – 5000
6	Poor	389 (15.3)	High	5850 – 6600

Table A.3 Light and focus conditions for 216 mm (8.5 in.) distance

Condition	**Focus**	**Focal Length, mm (in.)**	**Lighting**	**Light Range, lumens**
1	Ideal	216 (8.5)	High	5850 – 6600
2	Ideal	216 (8.5)	Medium	4450 – 5000
3	Ideal	216 (8.5)	Low	2000 – 2350
4	Fair	205 (8.1)	High	5850 – 6600
5	Fair	205 (8.1)	Medium	4450 – 5000
6	Poor	195 (7.7)	High	5850 – 6600

Typical DIC results for each camera to specimen distances are shown in figures A.1 through A.6. This shows the comparison between more and less ideal conditions.

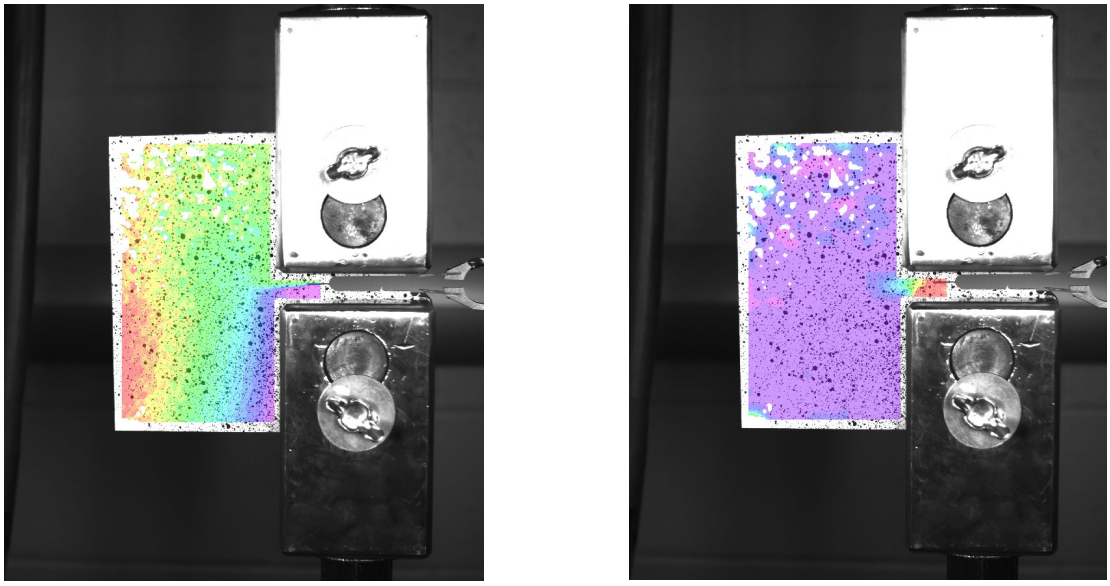

(a) (b)

Figure A.1 DIC results for a 25.4 mm (1.0 in.) crack with 648 mm (25.5 in.) camera distance under LC5 and Condition 1 in terms of (a) displacement and (b) strain

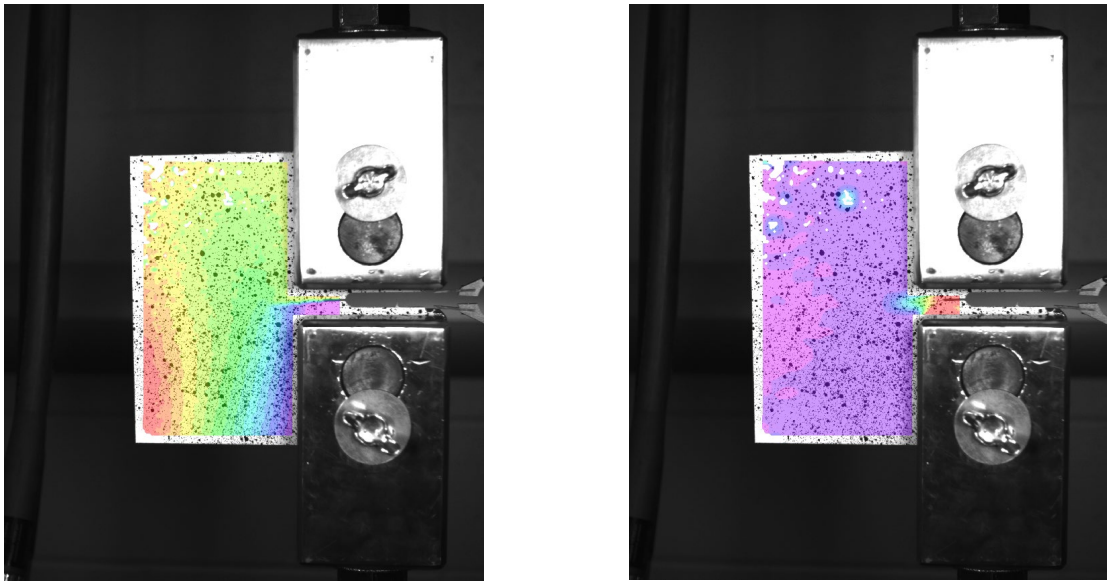

(a) (b)

Figure A.2 DIC results for a 25.4 mm (1.0 in.) crack with 648 mm (25.5 in.) camera distance under LC5 and Condition 5 in terms of (a) displacement and (b) strain

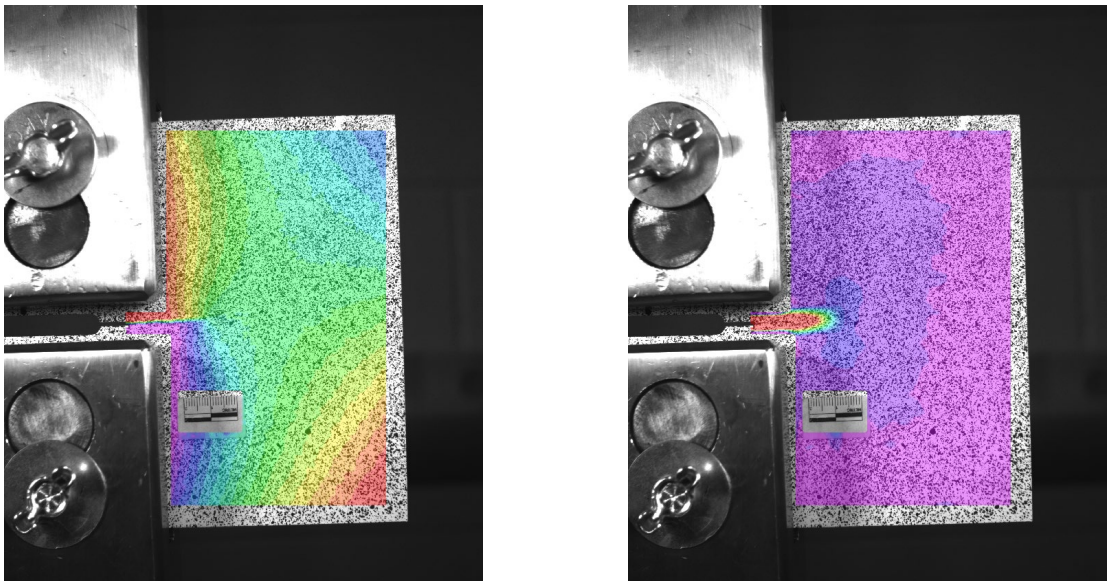

(a) (b)

Figure A.3 DIC results for a 25.4 mm (1.0 in.) crack with 432 mm (17.0 in.) camera distance under LC5 and Condition 1 in terms of (a) displacement and (b) strain

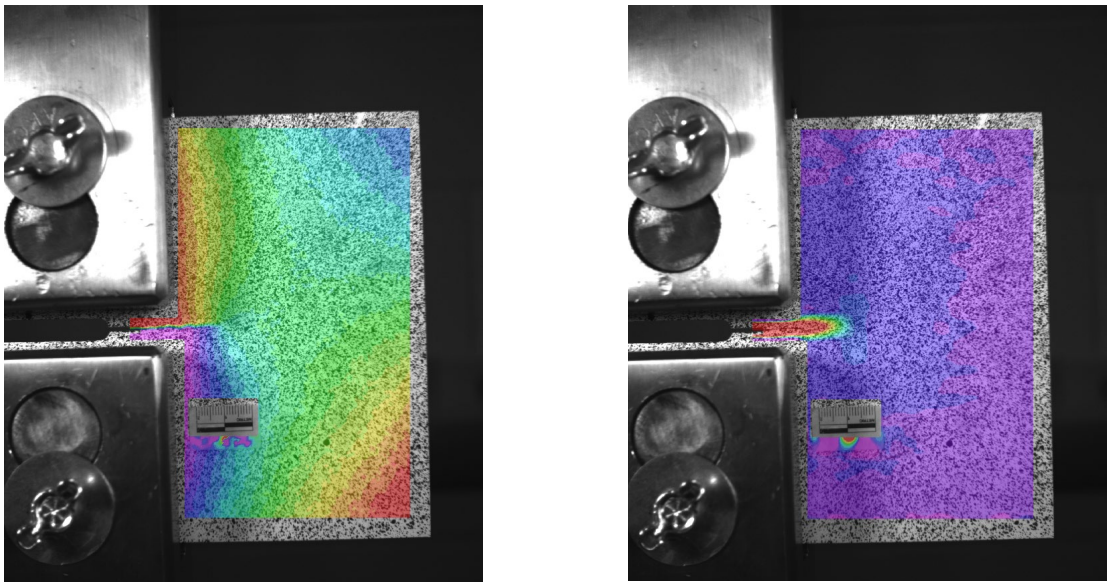

(a) (b)

Figure A.4 DIC results for a 25.4 mm (1.0 in.) crack with 432 mm (17.0 in.) camera distance under LC5 and Condition 5 in terms of (a) displacement and (b) strain

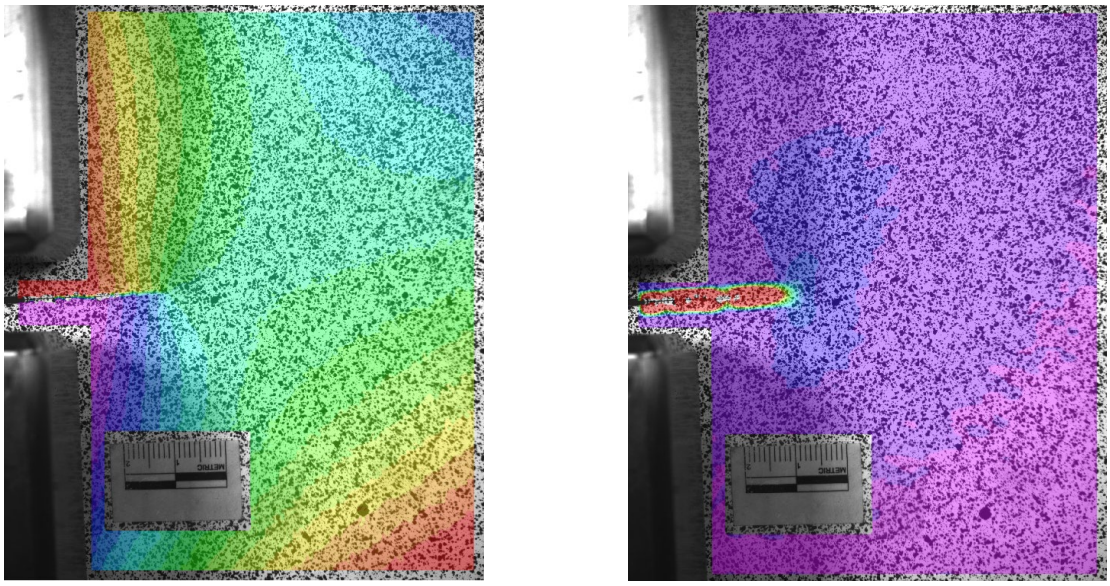

(a) (b)

Figure A.5 DIC results for a 25.4 mm (1.0 in.) crack with 216 mm (8.5 in.) camera distance under LC5 and Condition 1 in terms of (a) displacement and (b) strain

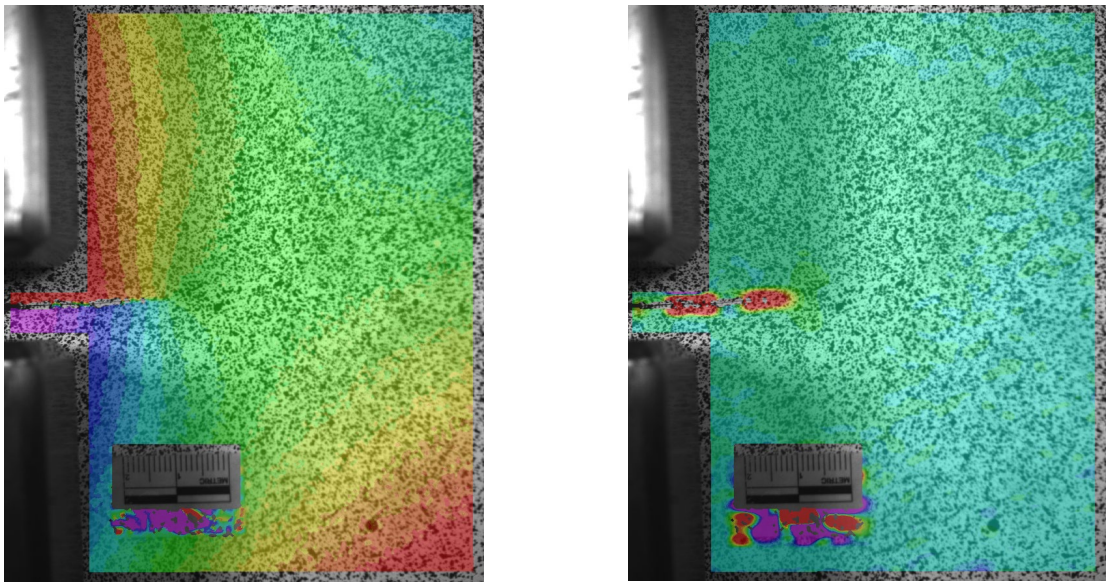

(a) (b)

Figure A.6 DIC results for a 25.4 mm (1.0 in.) crack with 216 mm (8.5 in.) camera distance under LC5 and Condition 5 in terms of (a) displacement and (b) strain

The relative displacement and convergence for each camera to specimen distance is shown in figures A.7 through A.12. These are representative of each load case evaluated.

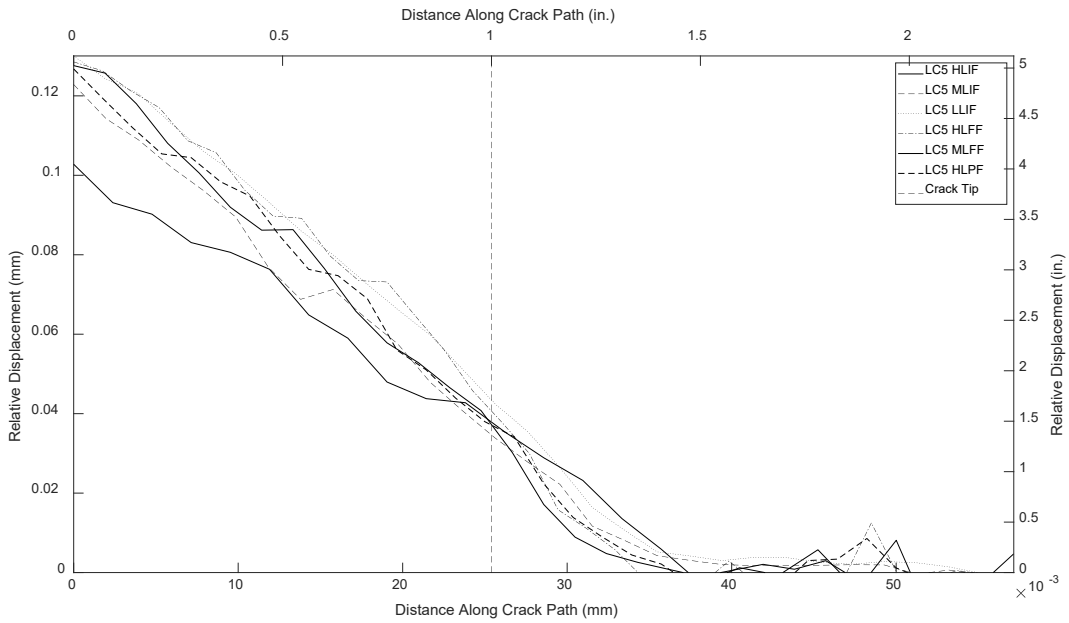

Figure A.7 Relative displacement of a 25.4 mm (1.0 in.) crack with a camera distance of 648 mm (25.5 in.) under LC5

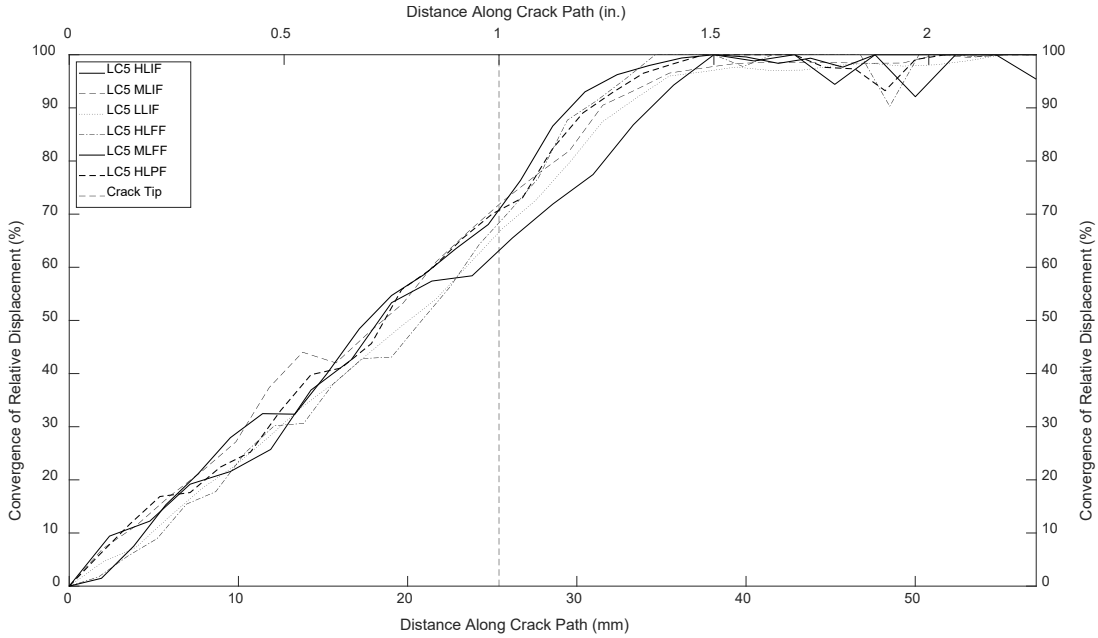

Figure A.8 Convergence of relative displacement of a 25.4 mm (1.0 in.) crack with a camera distance of 648 mm (25.5 in.) under LC5

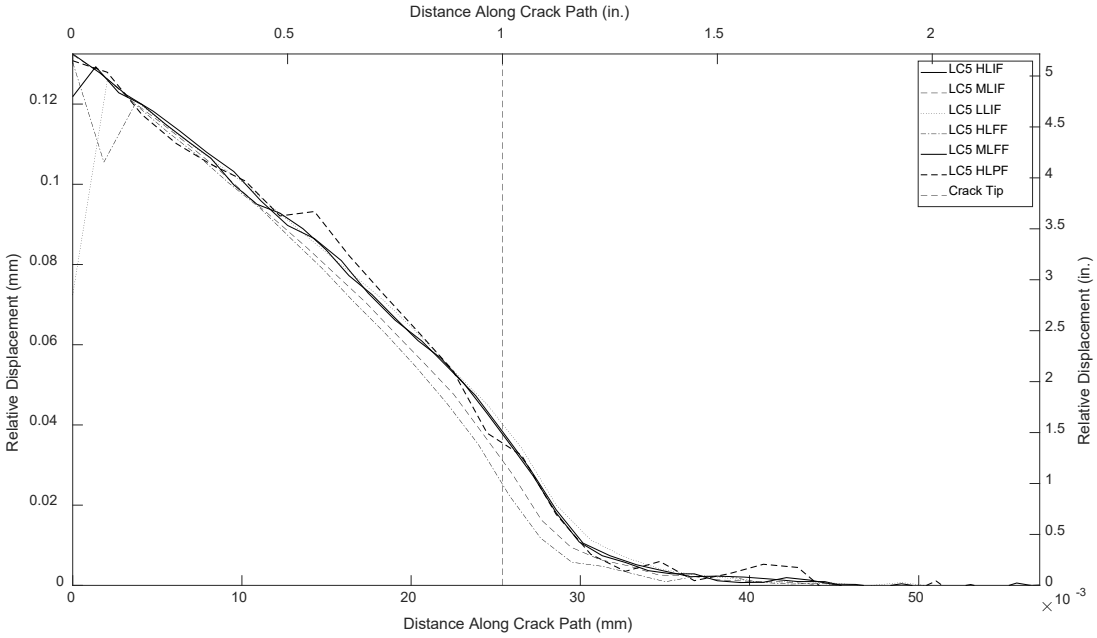

Figure A.9 Relative displacement of a 25.4 mm (1.0 in.) crack with a camera distance of 432 mm (17.0 in.) under LC5

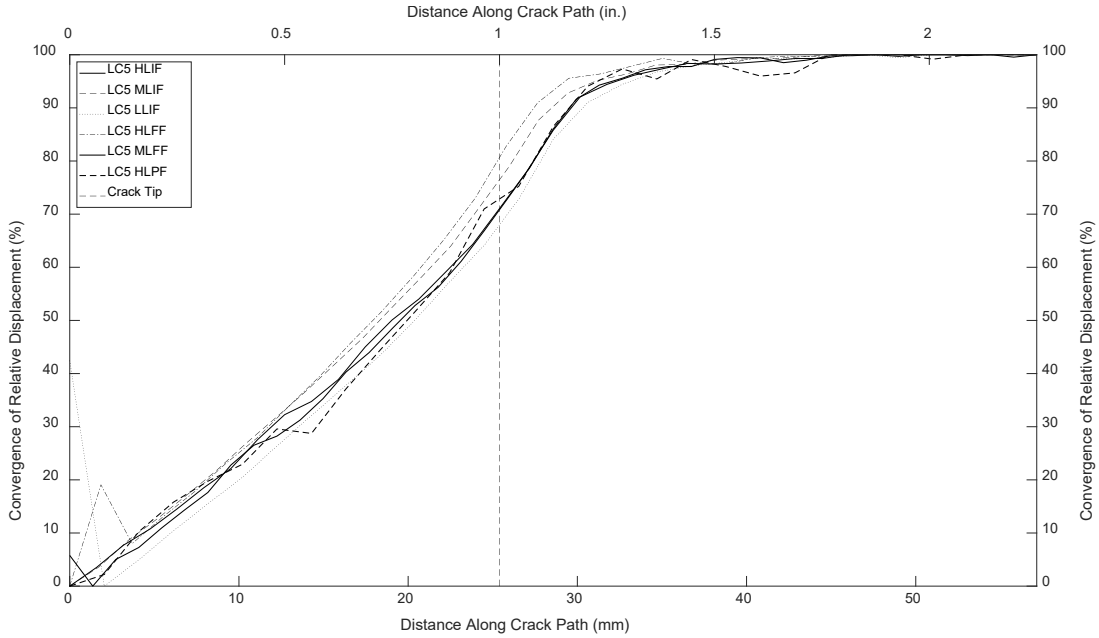

Figure A.10 Convergence of relative displacement of a 25.4 mm (1.0 in.) crack with a camera distance of 432 mm (17.0 in.) under LC5

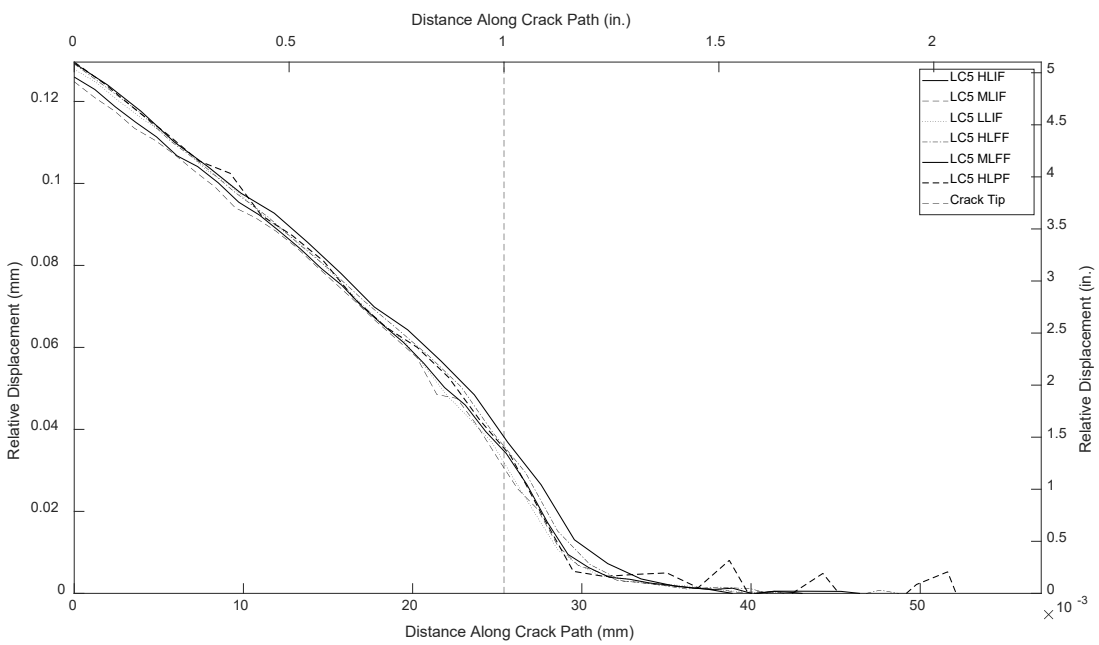

Figure A.11 Relative displacement of a 25.4 mm (1.0 in.) crack with a camera distance of 216 mm (8.5 in.) under LC5

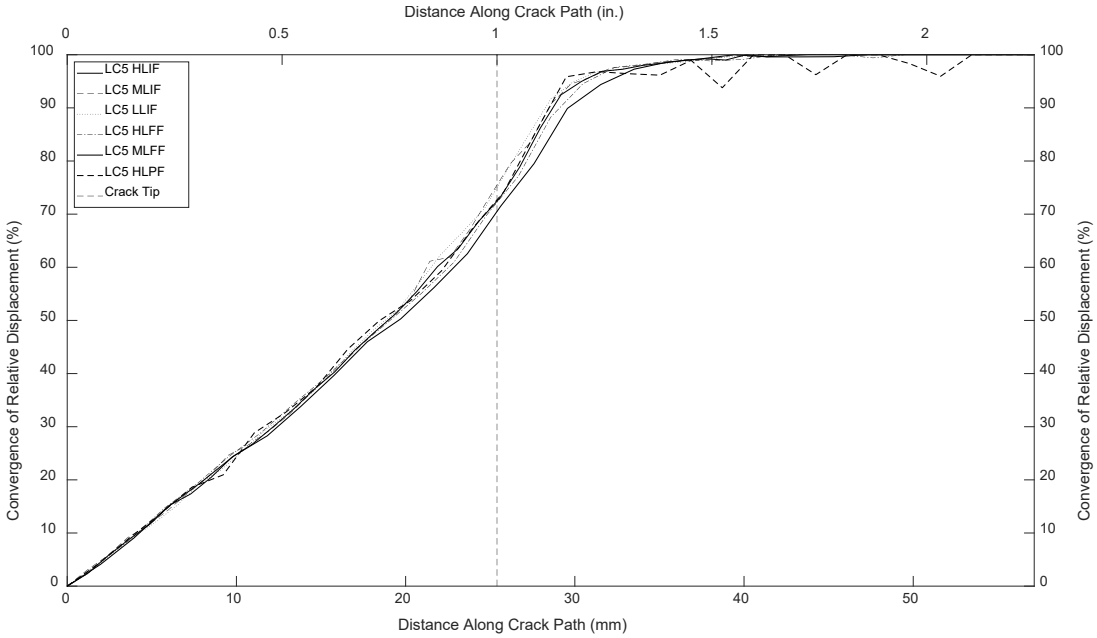

Figure A.12 Convergence of relative displacement of a 25.4 mm (1.0 in.) crack with a camera distance of 216 mm (8.5 in.) under LC5

Convergence values for each condition were averaged across all five load cases for a crack length of 25.4 mm (1.0 in.), shown in tables A.4 through A.6. These tables show a camera-to-specimen distance of 648, 432, and 216 mm (25.5, 17.0, and 8.5 in.), respectively. The convergence for each condition and load case is shown visually in figures A.13 through A.15. These results are representative of each crack length.

Table A.4 Average convergence at 25.4 mm (1.0 in.) crack tip for 648 mm (25.5 in.) camera distance

Light and Focus Condition	Average Convergence	Difference
Ideal	92.6%	N/A
1	71.5%	21.1%
2	72.3%	20.3%
3	69.6%	23.0%
4	73.3%	19.3%
5	66.2%	26.4%
6	73.1%	19.5%

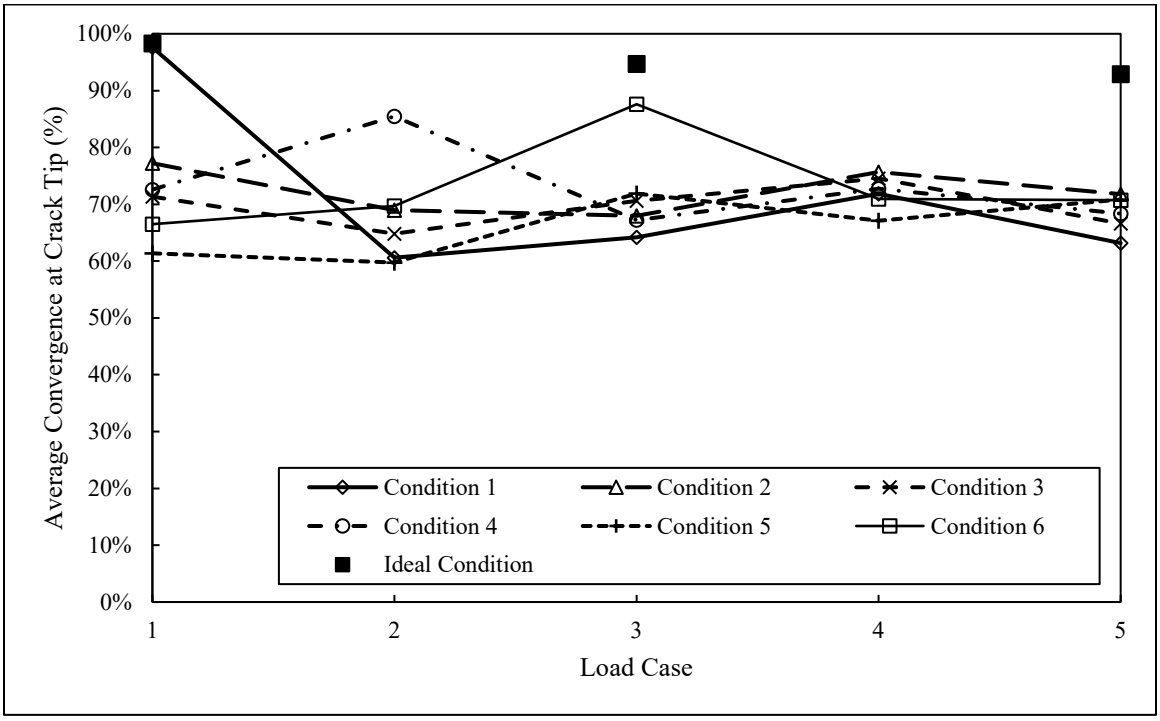

Figure A.13 Average convergence at crack tip for each load case and condition for a 25.4 mm (1.0 in.) crack with a camera distance of 648 mm (25.5 in.)

Table A.5 Average convergence at 25.4 mm (1.0 in.) crack tip for 432 mm (17.0 in.) camera distance

Light and Focus Condition	Average Convergence	Difference
Ideal	92.6%	N/A
1	70.7%	21.9%
2	76.6%	16.0%
3	69.9%	22.7%
4	80.5%	12.1%
5	72.0%	20.6%
6	72.9%	19.7%

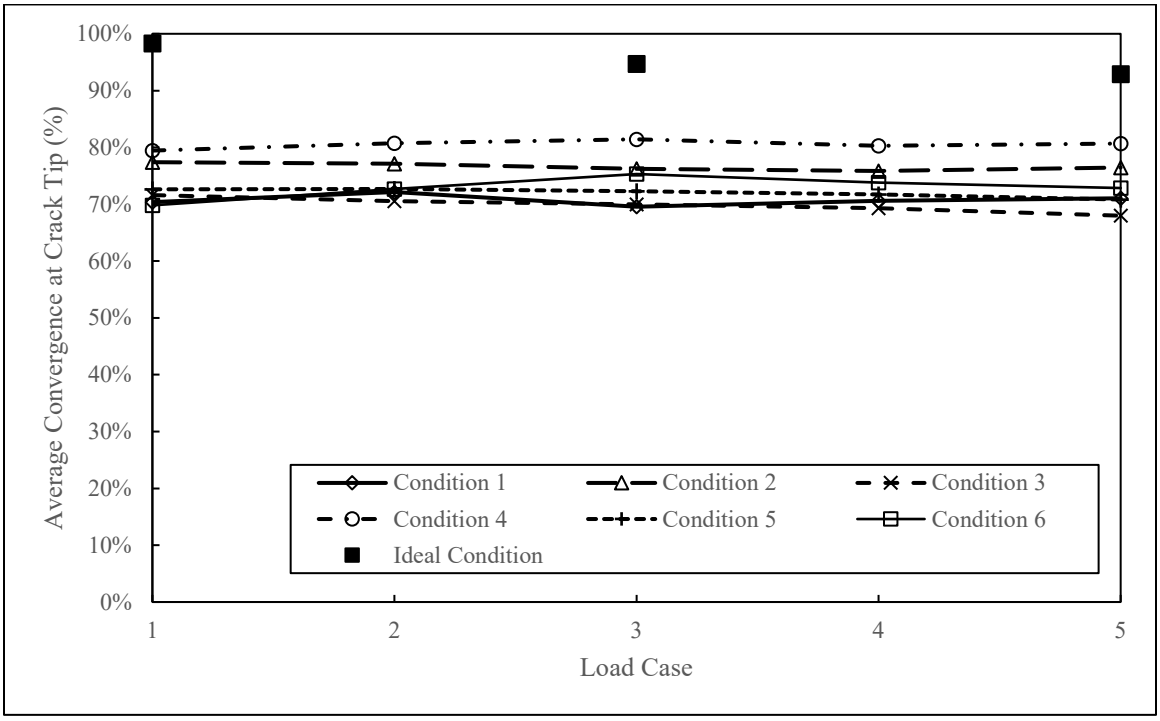

Figure A.14 Average convergence at crack tip for each load case and condition for a 25.4 mm (1.0 in.) crack with a camera distance of 432 mm (17.0 in.)

Table A.6 Average convergence at 25.4 mm (1.0 in.) crack tip for 216 mm (8.5 in.) camera distance

Light and Focus Condition	Average Convergence	Difference
Ideal	92.6%	N/A
1	73.0%	19.6%
2	75.7%	16.9%
3	75.6%	17.0%
4	72.6%	20.0%
5	70.1%	22.5%
6	72.8%	19.8%

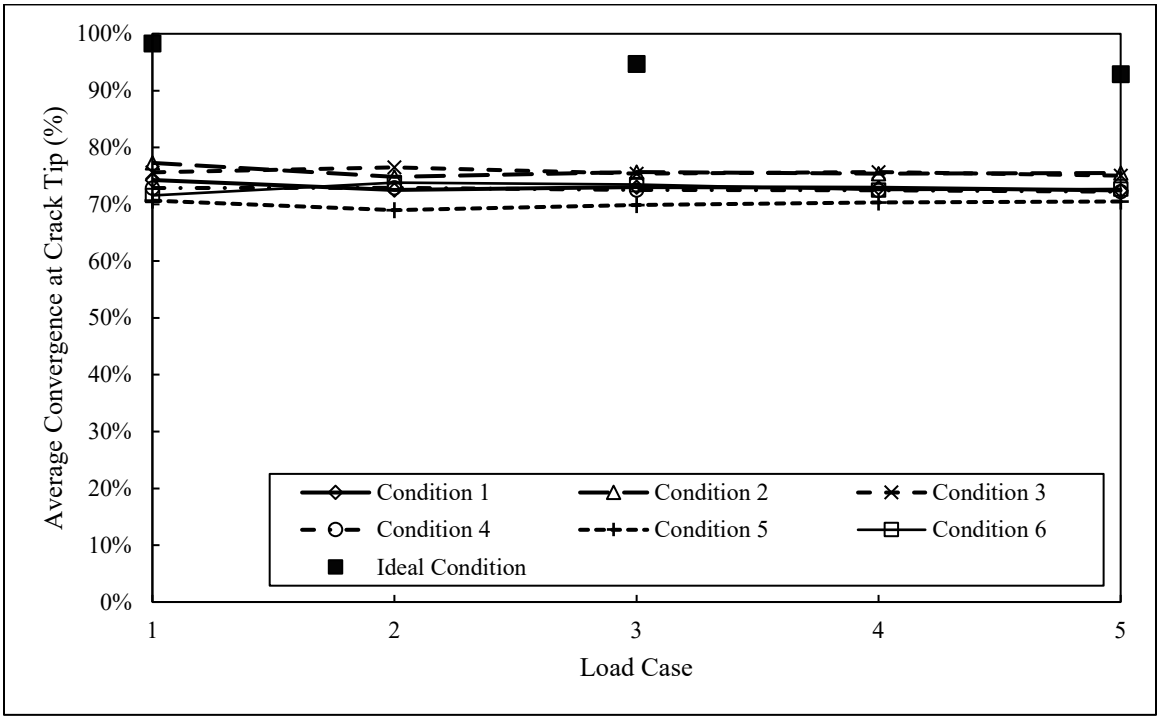

Figure A.15 Average convergence at crack tip for each load case and condition for a 25.4 mm (1.0 in.) crack with a camera distance of 216 mm (8.5 in.)

Figures A.16 through A.23 show the plots of convergence of relative displacement for different aperture values and camera to specimen distances. The vertical dotted line represents the 50.8 mm (2.0 in.) crack length.

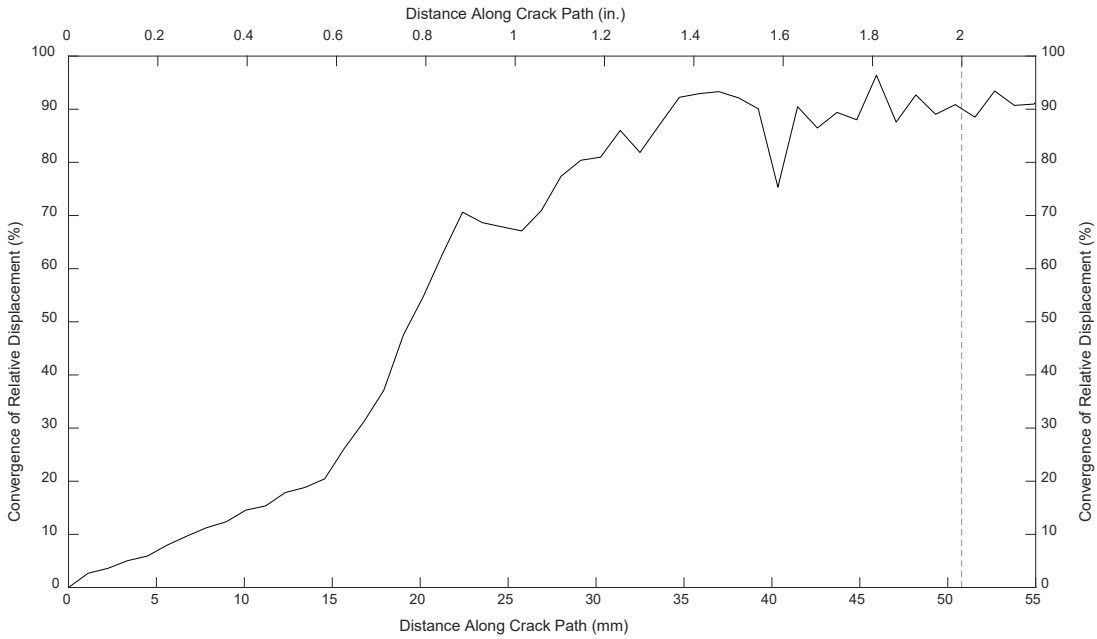

Figure A.16 Convergence of relative displacement of a 50.8 mm (2.0 in.) crack with a camera distance of 203.2 mm (8.0 in.) and an aperture of f/1.4 under LC5

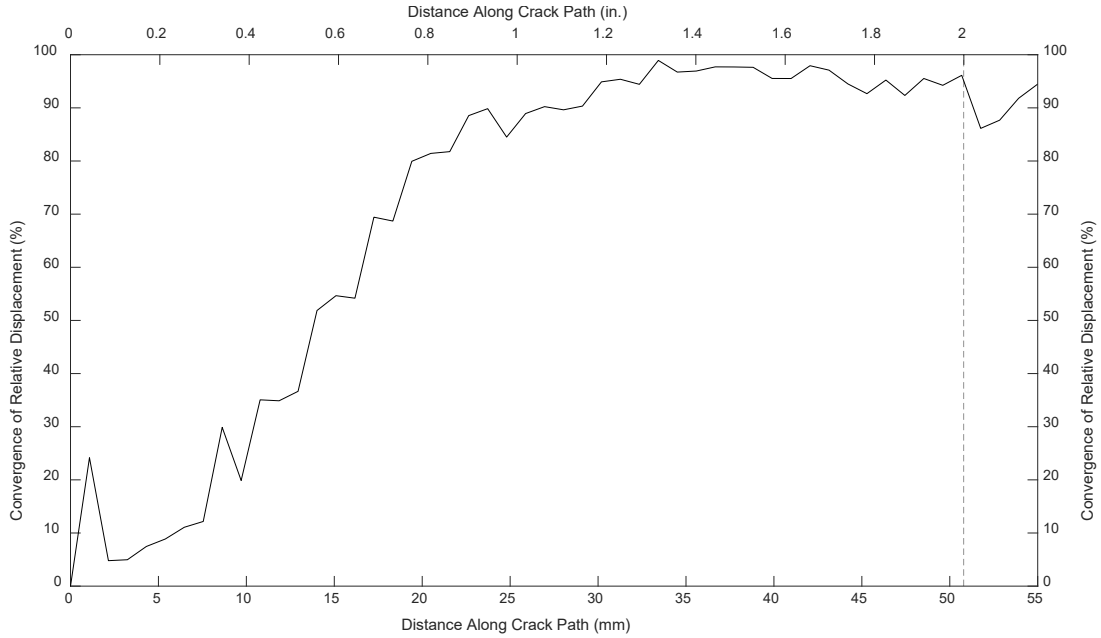

Figure A.17 Convergence of relative displacement of a 50.8 mm (2.0 in.) crack with a camera distance of 203.2 mm (8.0 in.) and an aperture of f/2.8 under LC5

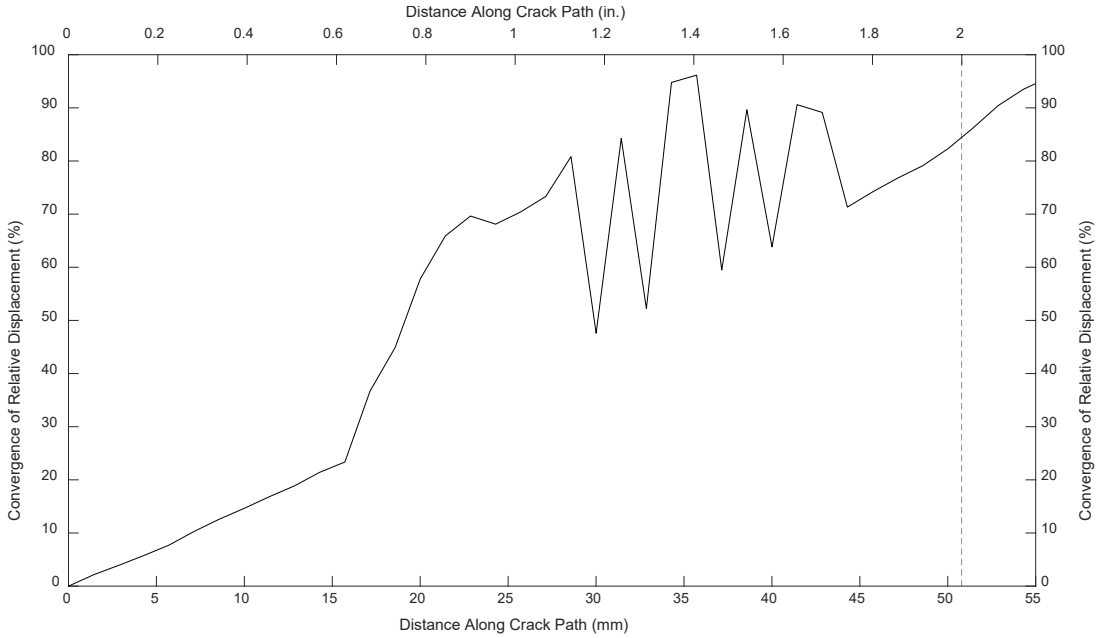

Figure A.18 Convergence of relative displacement of a 50.8 mm (2.0 in.) crack with a camera distance of 304.8 mm (12.0 in.) and an aperture of f/1.4 under LC5

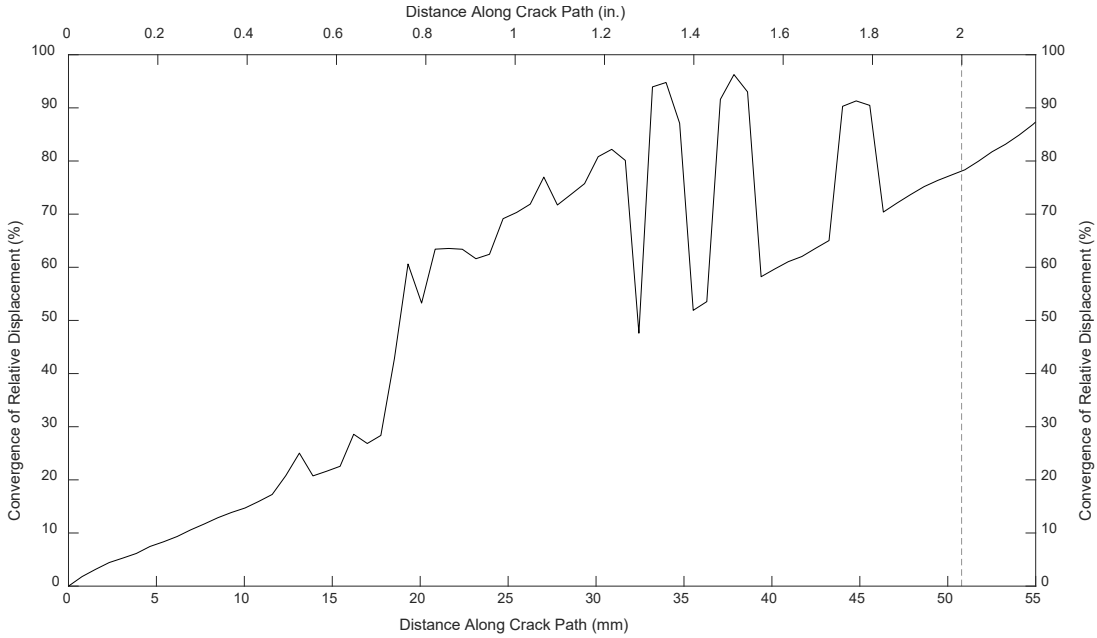

Figure A.19 Convergence of relative displacement of a 50.8 mm (2.0 in.) crack with a camera distance of 304.8 mm (12.0 in.) and an aperture of f/2.8 under LC5

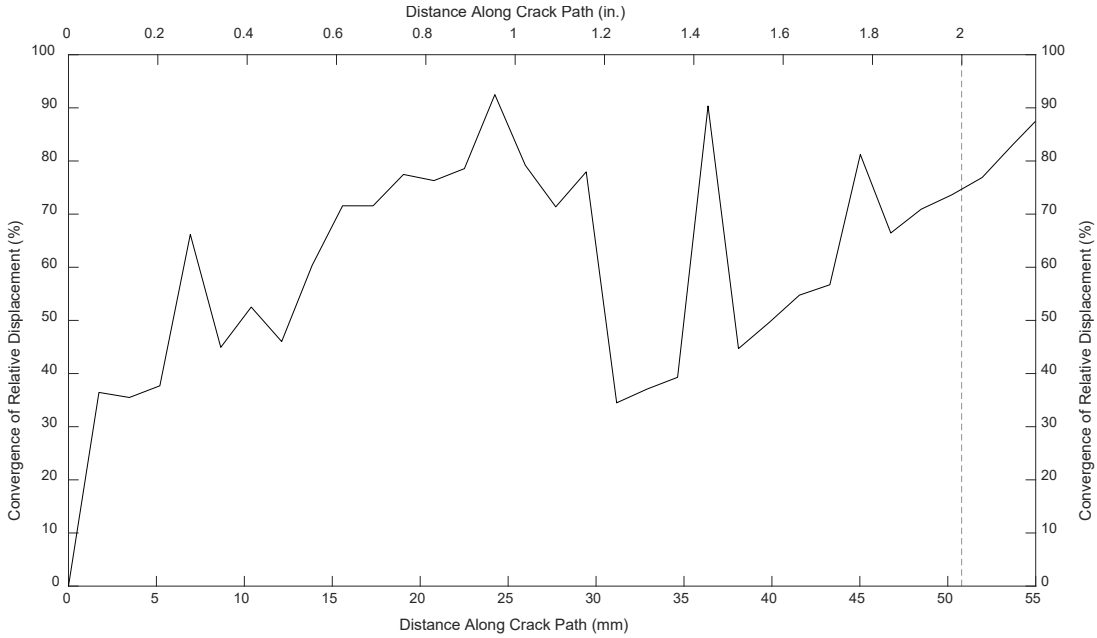

Figure A.20 Convergence of relative displacement of a 50.8 mm (2.0 in.) crack with a camera distance of 457.2 mm (18.0 in.) and an aperture of f/1.4 under LC5

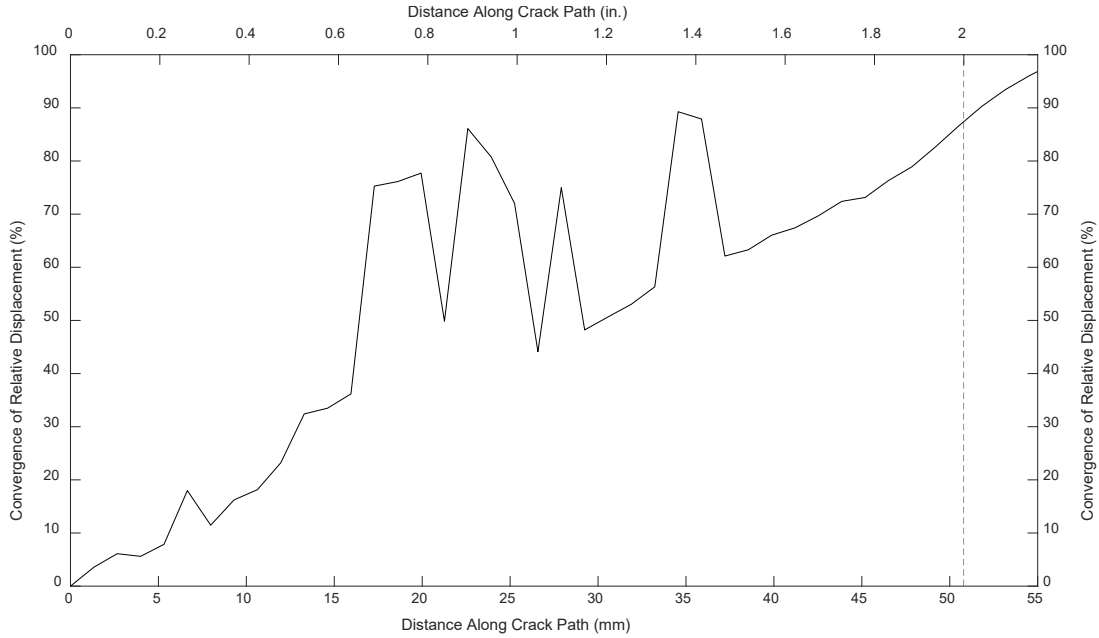

Figure A.21 Convergence of relative displacement of a 50.8 mm (2.0 in.) crack with a camera distance of 457.2 mm (18.0 in.) and an aperture of f/2.8 under LC5

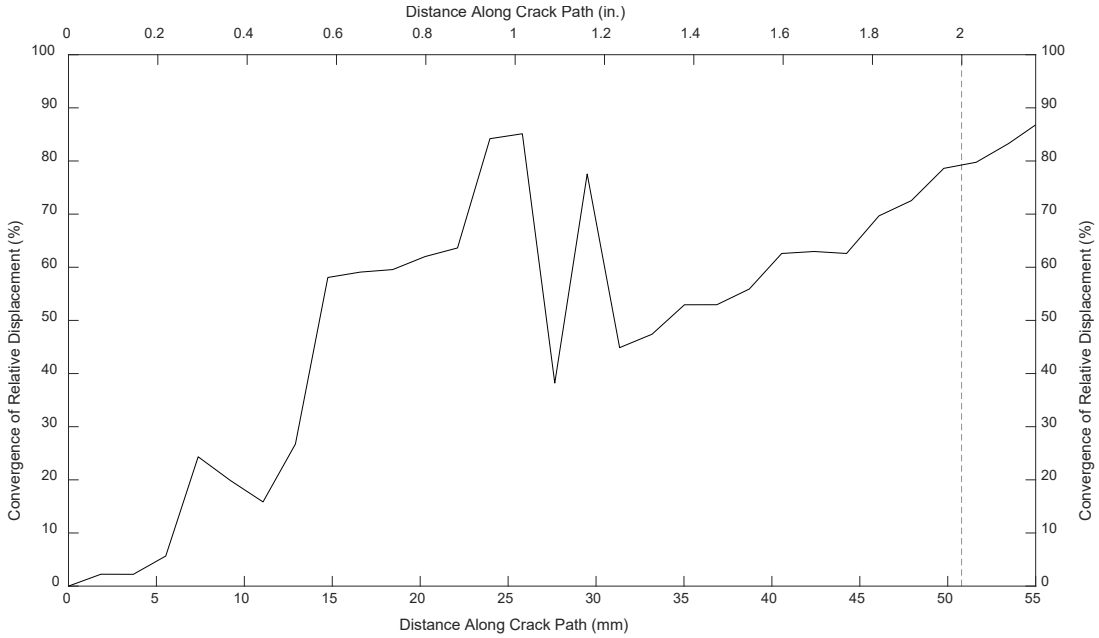

Figure A.22 Convergence of relative displacement of a 50.8 mm (2.0 in.) crack with a camera distance of 609.6 mm (24.0 in.) and an aperture of f/1.4 under LC5

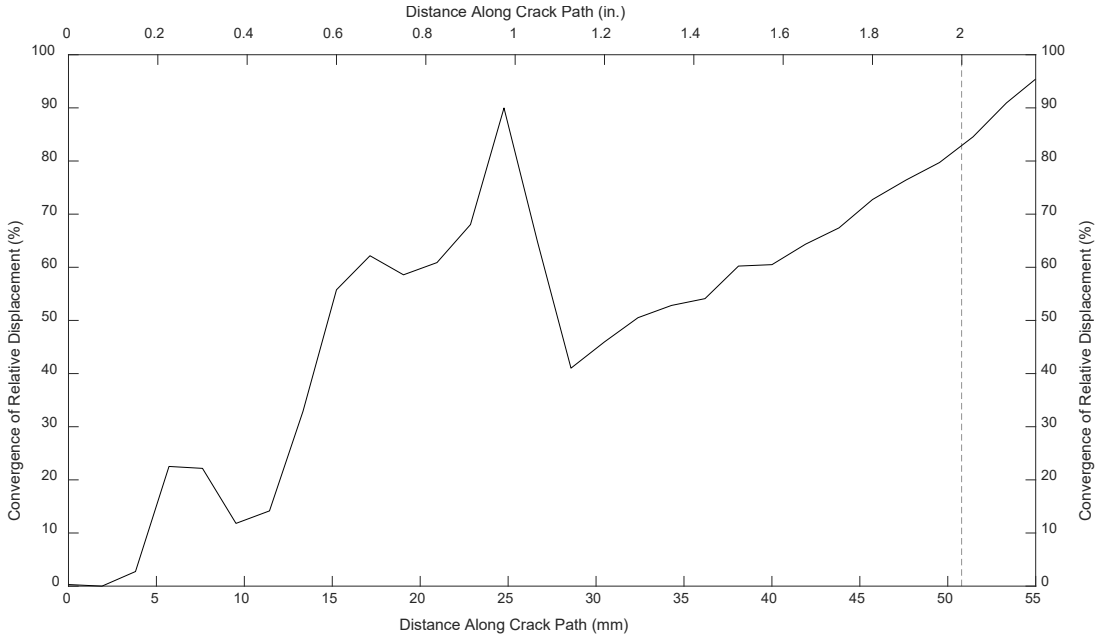

Figure A.23 Convergence of relative displacement of a 50.8 mm (2.0 in.) crack with a camera distance of 609.6 mm (24.0 in.) and an aperture of f/2.8 under LC5

Figures A.24 through A.29 show the in- and out-of-plane crack displacement gradients for the three open-source DIC software packages that were identified as possible alternatives to commercially available DIC. *Ncorr* is shown in figures A.24 and A.25, *ALDIC* is shown in figures A.26 and A.27, and *DICe* is shown in figures A.28 and A.29.

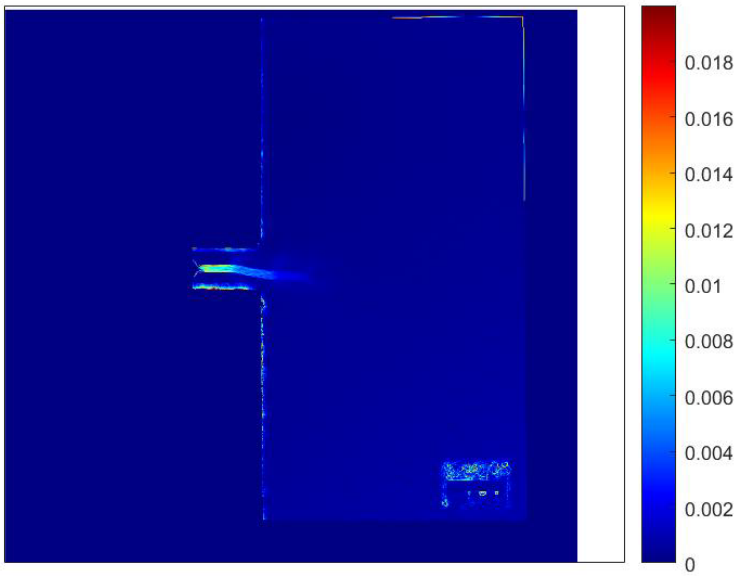

Figure A.24 *Ncorr* in-plane crack displacement gradient

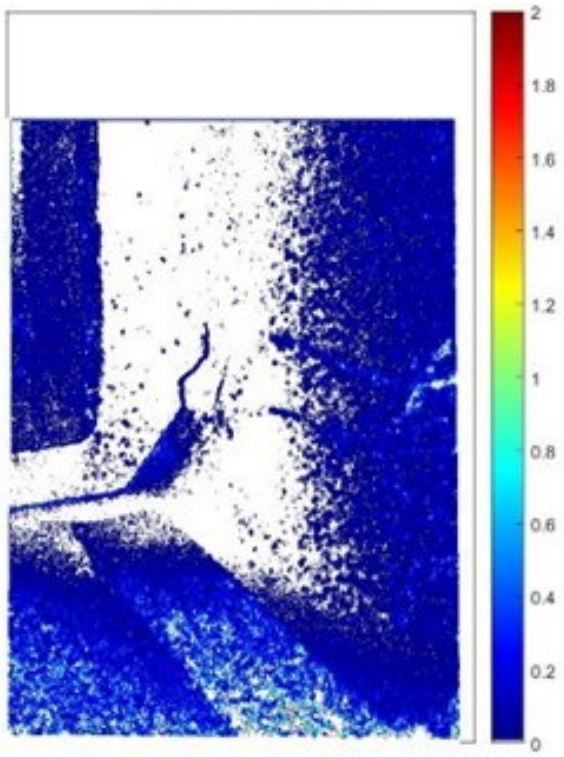

Figure A.25 *Ncorr* out-of-plane crack displacement gradient

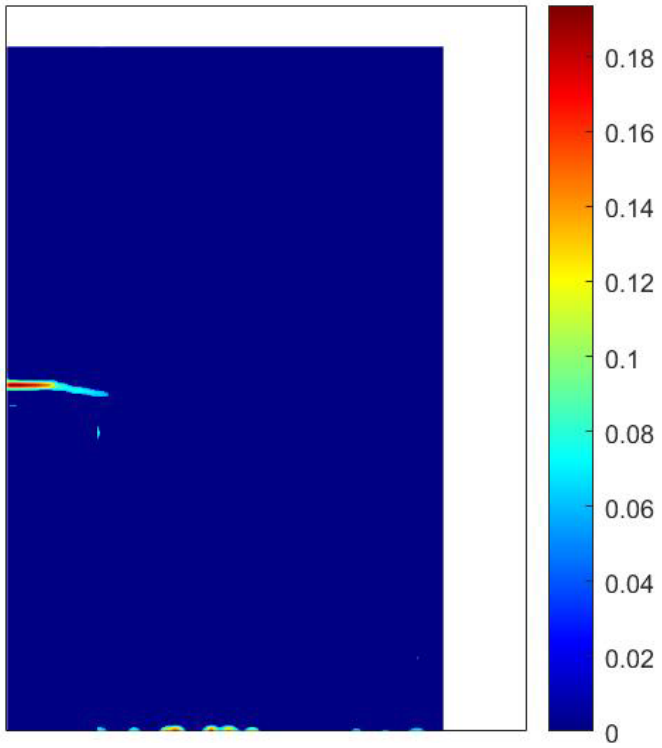

Figure A.26 *ALDIC* in-plane crack displacement gradient

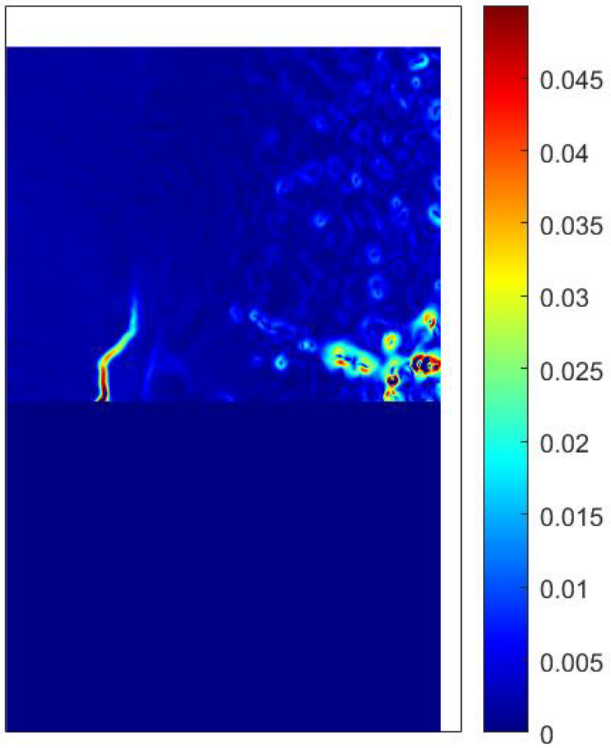

Figure A.27 *ALDIC* out-of-plane crack displacement gradient

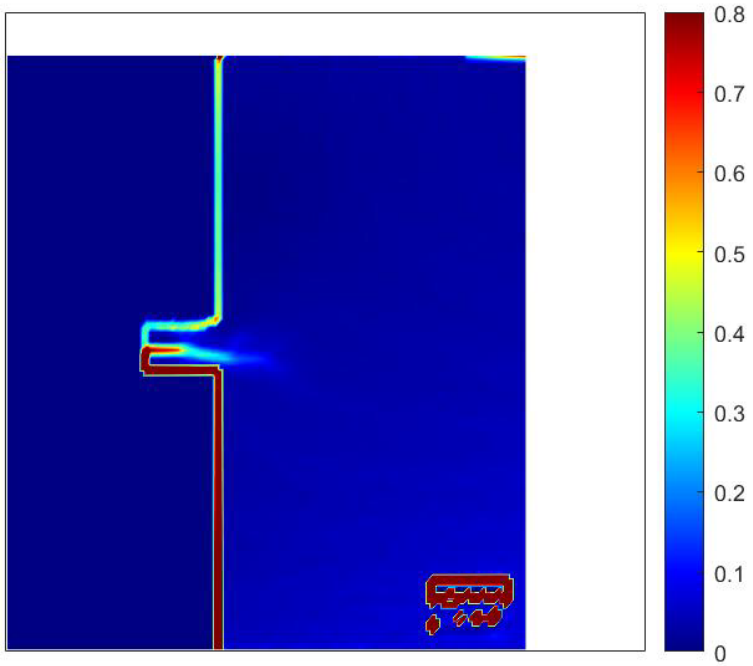

Figure A.28 DICe in-plane crack displacement gradient

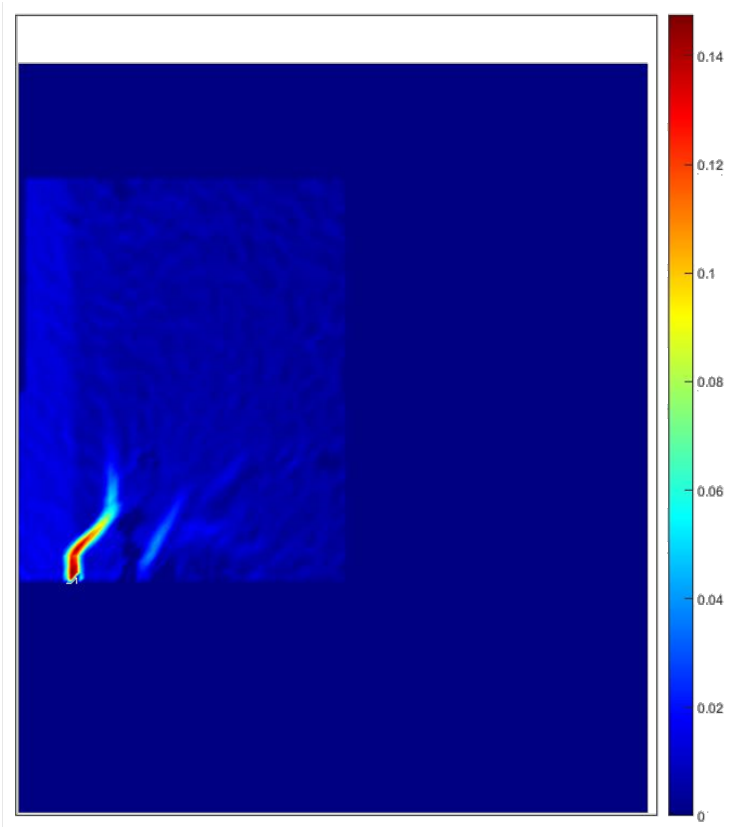

Figure A.29 *DICe* out-of-plane crack displacement gradient

The plots of convergence of relative displacement for out-of-plane cracking analyzed with a single camera are shown in figures A.30 through A.36. The blue vertical lines represent the different segments of the 44.5 mm (1.75 in.) crack. The red line shows the original data when processed using VIC-3D.

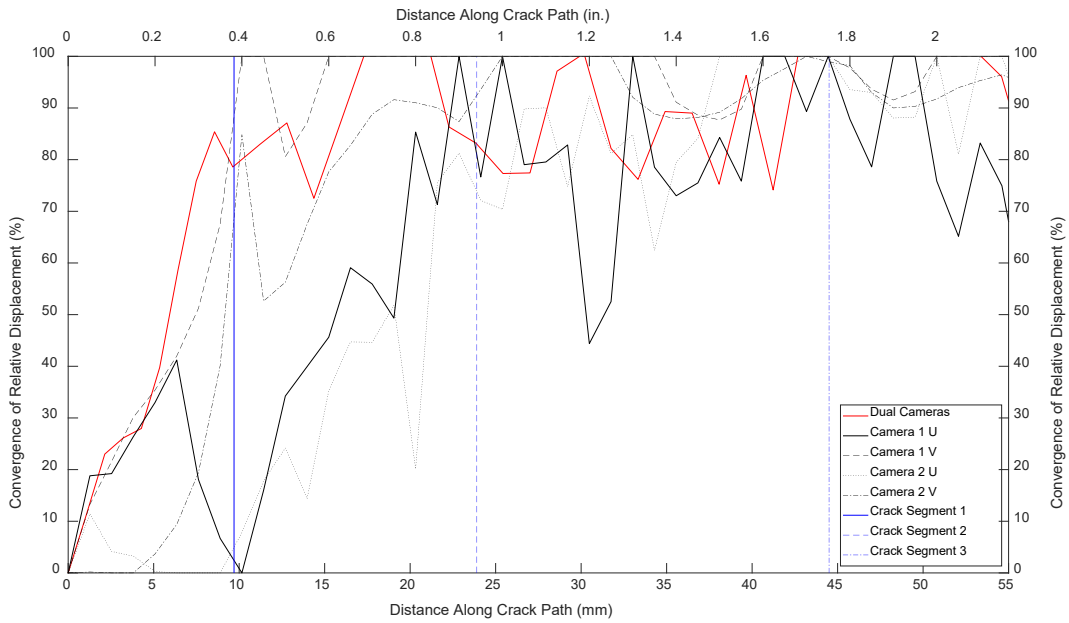

Figure A.30 Convergence of relative displacement of a 44.5 mm (1.75 in.) complex crack under LC1

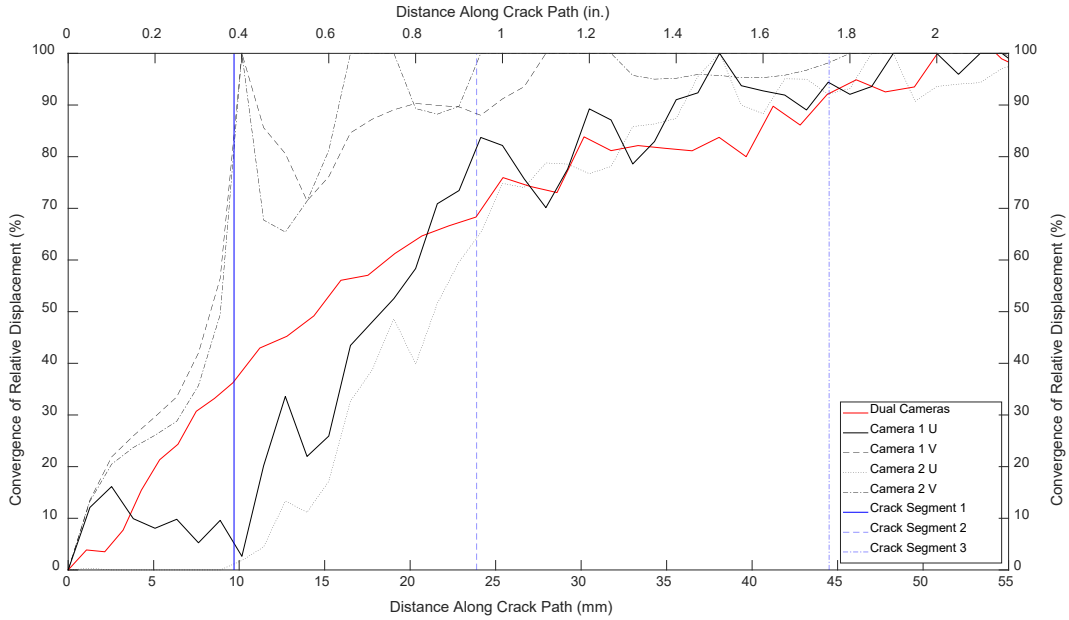

Figure A.31 Convergence of relative displacement of a 44.5 mm (1.75 in.) complex crack under LC2

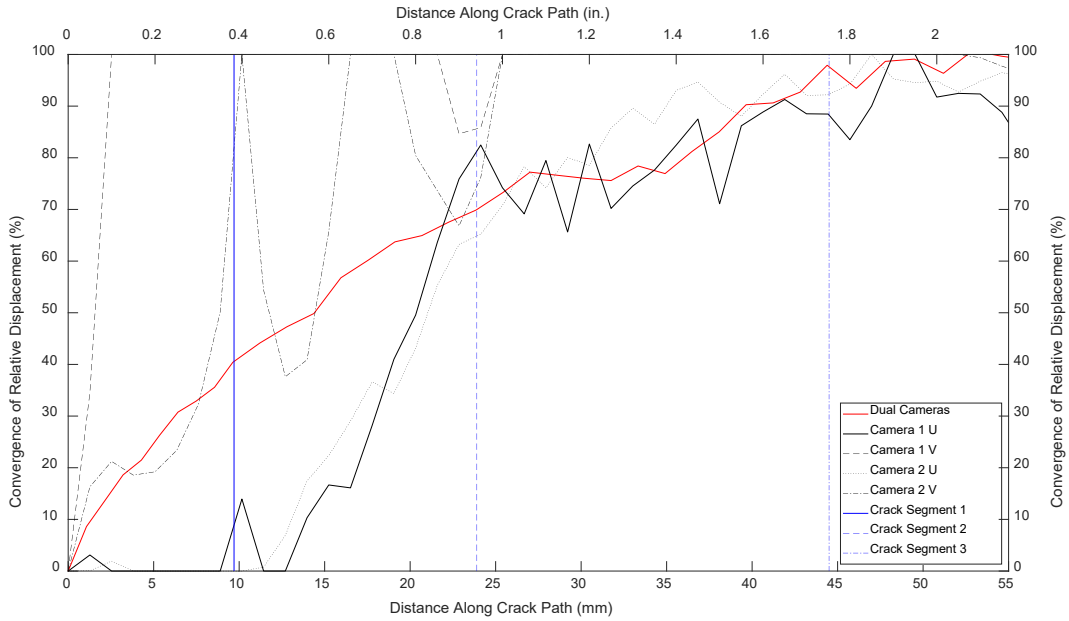

Figure A.32 Convergence of relative displacement of a 44.5 mm (1.75 in.) complex crack under LC3

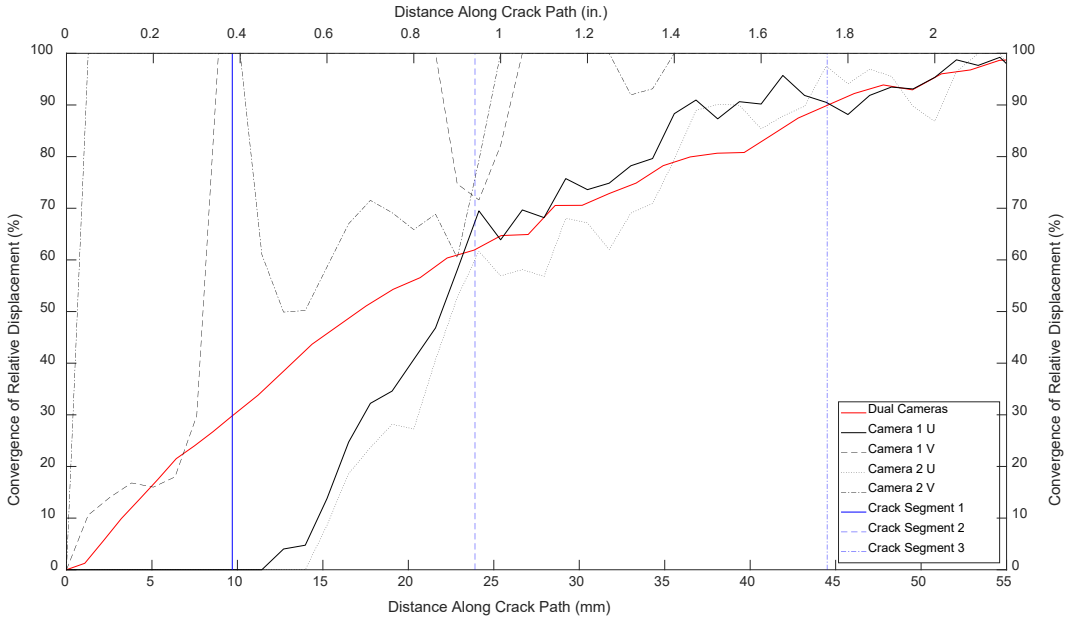

Figure A.33 Convergence of relative displacement of a 44.5 mm (1.75 in.) complex crack under LC4

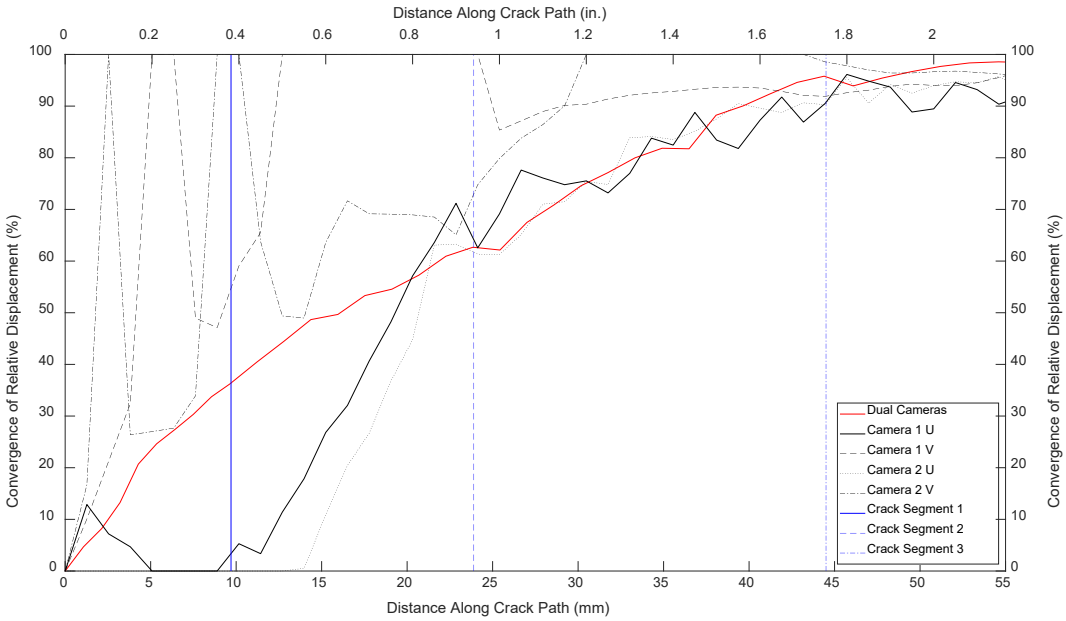

Figure A.34 Convergence of relative displacement of a 44.5 mm (1.75 in.) complex crack under LC5

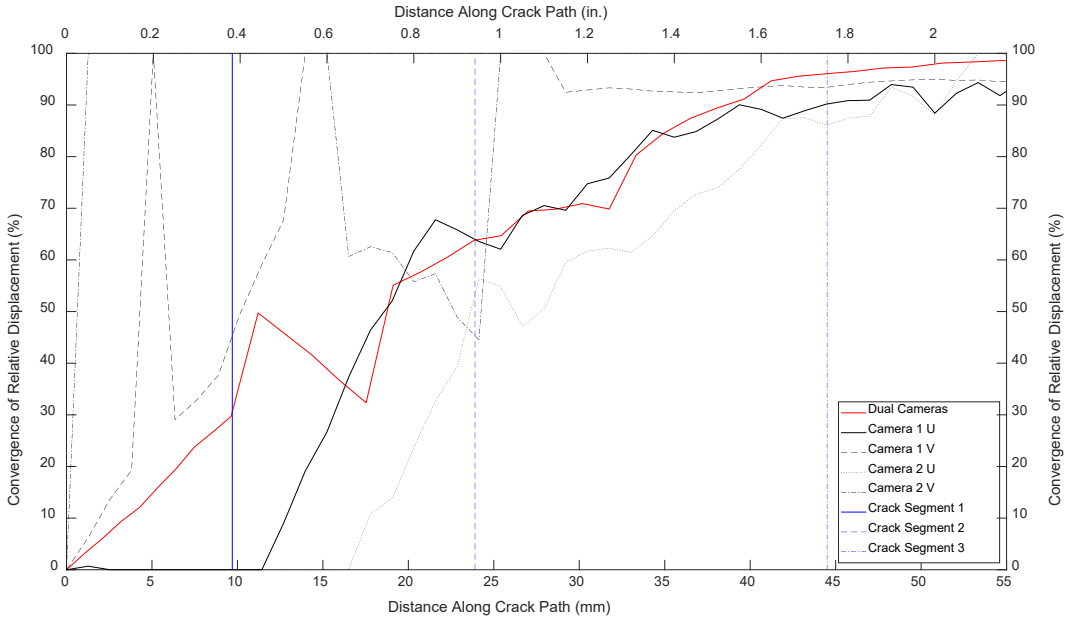

Figure A.35 Convergence of relative displacement of a 44.5 mm (1.75 in.) complex crack under LC6

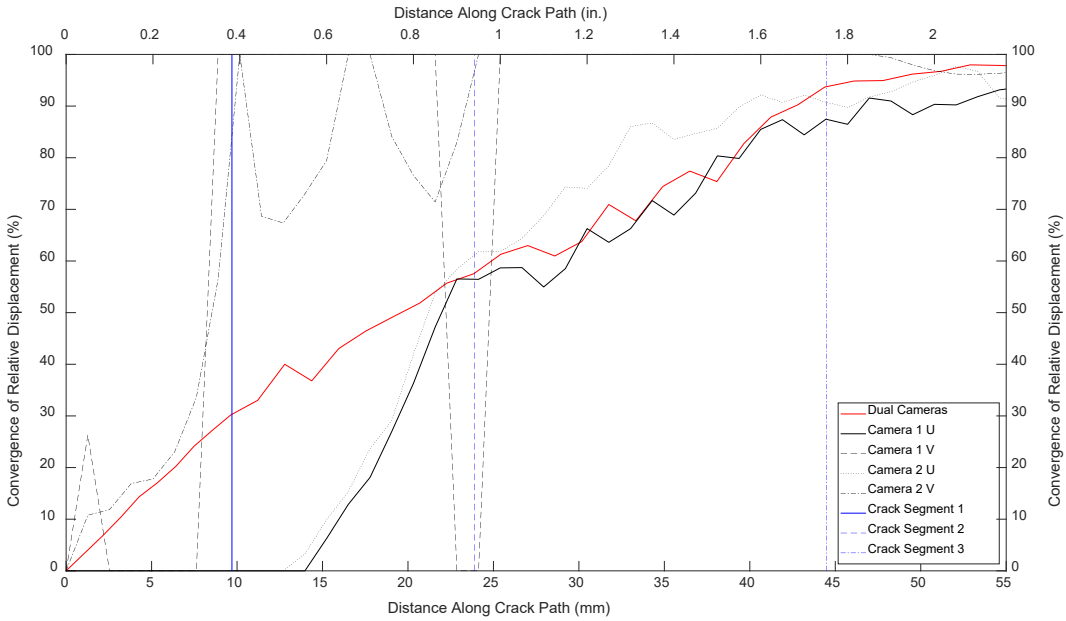

Figure A.36 Convergence of relative displacement of a 44.5 mm (1.75 in.) complex crack under LC7